Physics – Uspekhi **65** (2) 131 – 162 (2022)

REVIEWS OF TOPICAL PROBLEMS PACS numbers: 42.50.Lc, **42.55. – f**, **42.65. – k**, 42.65.Tg

Laser solitons: topological and quantum phenomena

N A Veretenov, N N Rosanov, S V Fedorov

DOI: https://doi.org/10.3367/UFNe.2020.11.038869

Contents

Abstract. A review of the properties of dissipative solitons with different dimensions and various topological characteristics in lasers and laser systems with saturable absorption is presented. Unlike conservative solitons, laser solitons are attractors, the increased stability of which is caused by the balance of energy inflow and outflow. The topology of laser solitons is due to their complex internal structure, which is determined by the field of radiation energy fluxes, and the energy characteristics are an important addition to the topological characteristics. The equation of their dynamics — the generalized Ginzburg – Landau equation — reflects the basic features of open nonlinear systems of various natures. The topological features of solitons expand the range of manifestations of their quantum fluctuations.

Keywords: dissipative, laser, topological, multidimensional solitons; quantum fluctuations

1. Introduction

Spatial, temporal, and spatiotemporal optical solitons, the spreading out of which during propagation is compensated by nonlinear focusing [1, 2], possess interesting particle-like properties and are promising for a number of applications. Of no small importance is the fact that, at present, it is optical solitons that are, in our opinion, studied the most intensely, which is facilitated by the rapid development of laser physics and technology. Depending on the contribution of dissipative factors, solitons are commonly divided into two large classes: conservative [1, 3] and dissipative [4, 5]. Those in the first class are implemented in systems with negligibly small losses, the magnitude of which is what limits the soliton lifetime. In dissipative solitons, the losses are balanced by the energy inflow from outside, so that they exist until this inflow is terminated. A fundamental difference between solitons of these two classes is that conservative solitons possess a continuous spectrum of basic parameters, whereas for dissipative solitons this spectrum is discrete due to the additional requirement of energy inflow/outflow balance (so-called classical quantization [6]). Therefore, the characteristics of a conservative soliton continuously drift under the action of even small fluctuations, substantially deviating from the initial ones over a long time. Under similar conditions, the characteristics of a dissipative soliton exhibit minor fluctuations near their fixed values. Thus, dissipative solitons are much more stable and less sensitive to noise than are conservative ones.

At the time, there are a number of reviews, special issues of journals, and monographs in which the results of research on dissipative optical solitons in various schemes are presented [5, 7–24]. The applied significance of such solitons is most vividly manifested in microresonators with whispering-gallery modes [25, 26] and fiber lasers [27, 28]. The present review mainly focuses on one of their implementations, in

N A Veretenov [(a)], **N N Rosanov** [(b)], **S V Fedorov** [(c)]
Ioffe Institute,
ul. Politekhnicheskaya 26, 194021 St. Petersburg, Russian Federation
E-mail: [(a)] torrek@gmail.com, [(b)] nnrosanov@mail.ru,
[(c)] sfedorov2006@bk.ru

Received 18 August 2020, revised 14 November 2020
Uspekhi Fizicheskikh Nauk **192** (2) 143 – 176 (2022)
Translated by V L Derbov

which solitons were predicted about 30 years ago [29, 30], namely, a wide-aperture laser or laser medium with saturable absorption. An important condition for the existence of laser solitons is the presence of bistability in the system: there should be at least two states with a homogeneous intensity distribution over the aperture, so that the soliton can be interpreted as an island of one state against the background of the other. Another constructive refinement, which makes it relatively easy to find dissipative optical solitons in numerical simulations, is related to the concept of switching waves, or fronts between two indicated states. The presence of diffractive oscillations of radiation intensity at the fronts is characteristic of optics. These oscillations, when the fronts approach at a distance comparable to their width, stop them from getting closer or moving away, which is what the formation of a soliton means [31].

Actually, the laser scheme is applicable to the case of nonequilibrium Bose condensates, e.g., exciton–polariton ones [32]. Minimizing the repetition of conclusions contained in monographs, we pay more attention to modern lines of research, which, in our opinion, are of primary importance, namely, first, topological phenomena for laser solitons with various geometric dimensions and, second, quantum fluctuations of such solitons. Indeed, topological phenomena in physics, in particular, optics, are now studied rather intensely. It is worth noting that so-called topological photonics deals mainly with the topology of an optical medium determined by the features of the medium energy band structure [33–37]. On the contrary, here we focus on the topology of the radiation itself, i.e., the phenomena of topological optics, adjacent to the singular optics [38–40]; in our case, it is possible to speak about dissipative nonlinear topological optics. At the same time, the significance of quantum fluctuations, which are also being intensely studied in the framework of quantum optics [41], in laser systems is due not only to the fact that they determine the ultimate capabilities of dealing with light, but also to the sharp increase in fluctuation intensity near topological singularities of radiation.

Generally, a detailed description of realistic laser systems requires considering many factors, including the propagation of optical radiation, the state of the optical medium and its response to the radiation, as well as the presence of a number of additional elements in these systems. To emphasize the generality of the physics of laser solitons, we use as our base the simplest case of a noninertial medium response, when the dynamics is described by a unified generalized Ginzburg–Landau equation for the field envelope.

In Section 2, we present basic models of the systems considered and the master equation for them. In Section 3, the simplest spatially homogeneous field distributions described by these equations are analyzed. Sections 4–7 sequentially present one-dimensional, two-dimensional, and three-dimensional bright solitons (i.e., finite-energy solitons against the background of a zero-intensity field), including an analysis of solitons with polarization singularities. Dark solitons are briefly considered in Section 8. In Section 9, the quantum Heisenberg–Langevin equation is presented, which describes quantum fluctuations in bright two-dimensional laser solitons, as well as illustrations of the calculation of these fluctuations. Various additional factors, including those beyond the framework of the generalized Ginzburg–Landau equation, are listed in Section 10. In Section 11, we summarize the results and discuss possible avenues of development in this field.

It should be noted that one-dimensional localized structures of radiation in a nonequilibrium (amplifying) medium have also been referred to as dissipative solitons in a number of papers (see, e.g., [42–45]). We will not follow this terminology, since such structures are definitely unstable.

2. Basic models and equations

The main systems considered in the present review are shown in Fig. 1. In them, a unidirectional propagation of radiation packets is implemented in a medium where both the refractive index and the absorption (gain) are optically nonlinear. The number of directions in which the radiation is localized due to nonlinear effects determines the system's dimensionality: 1 for those shown Fig. 1a, b; 2 for the one in Fig. 1c; and 3 for that in Fig. 1d. Single-pass schemes (Fig. 1a, c, d) turn into multipass ones when placed in a ring resonator (Fig. 1e); in the one-dimensional case, the multipass property is also implemented in the scheme shown in Fig. 1b.

The radiation is considered quasimonochromatic and close to a plane wave, which allows describing its propagation within the quasioptical approximation, or slow envelope approximation dating back to the studies by Leontovich and Fock [46, 47]. For this purpose, we present the electric field strength of radiation $\tilde{\mathbf{E}}(\mathbf{r}, t)$ as

$$\tilde{\mathbf{E}}(\mathbf{r}, t) = \mathrm{Re}\left\{\mathbf{e}E(\mathbf{r}, t)\exp\left(\mathrm{i}k_0 z - \mathrm{i}\omega_0 t\right)\right\},$$

where $\mathbf{r}$ is the radius vector, t is the time, $\mathbf{e}$ is the unit polarization vector, E is the envelope that changes slowly compared to the exponential function in this expression, ω_0 is the carrier frequency, k_0 is the real part of the wavenumber at this frequency, and z is the coordinate along the direction of predominant propagation of radiation. The medium is assumed to be a matrix having nonresonant refractive and absorption indices with centers embedded in it, which possess resonant gain and absorption. Then, e.g., for a three-dimensional scheme (Fig. 1d) and fixed linear polarization, from the Maxwell equations of continuous media electrodynamics, the master equation follows, namely, the generalized complex Ginzburg–Landau equation in the dimensionless form (see, e.g., [5]):

$$\frac{\partial E}{\partial z} = \left[(\mathrm{i} + d_\perp)\nabla_\perp^2 + (\mathrm{i} + d_\parallel)\frac{\partial^2}{\partial \tau^2}\right]E + fE. \qquad (2.1)$$

Here, $\Delta_\perp = \partial^2/\partial x^2 + \partial^2/\partial y^2$ is the transverse Laplacian, x and y are the transverse coordinates, $\tau = t - z/v_\mathrm{g}$ is the time

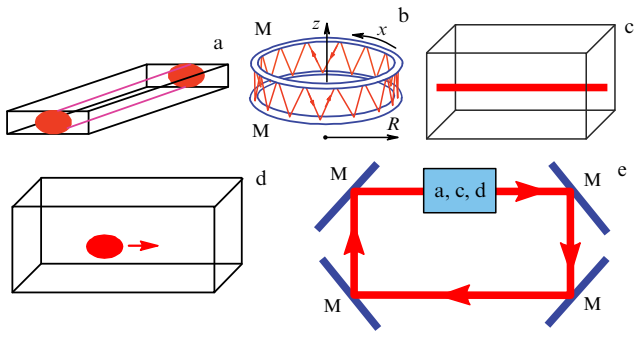

Figure 1. (Color online.) Systems under consideration. The radiation is quasicontinuous (a–c) or pulsed (d, e). The spatial domain occupied by the radiation is simply connected (a, c, d) and nonsimply connected (b, e). M are mirrors.

in the accompanying coordinate frame that moves along the z-axis (the evolution variable) with group velocity v_g, and the 'diffusion coefficients' $d_\parallel$ and $d_\perp$ lie in the interval $0 < d_{\perp,\parallel} \ll 1$. In this case, linear operator $i\nabla_\perp^2$ describes the diffraction of radiation, $d_\perp\nabla_\perp^2$, the angular selectivity of losses in the medium [48, 49], $i\partial^2/\partial\tau^2$, the frequency dispersion of the matrix refractive index, and $d_\parallel\partial^2/\partial\tau^2$, the frequency dispersion of losses in the matrix. Finally, the last term on the right-hand side of Eqn (2.1) represents the reaction of the centers to the radiation; it is convenient to include nonresonant absorption by the matrix in this term as well. In the basic model, this reaction is considered inertialess and to depend only on the radiation intensity $I = |E|^2$, i.e., $f = f(I)$.

In the simplest case, the diffusion coefficients are equal, $d_\parallel = d_\perp = d$. The form of Eqn (2.1) is then simplified:

$$\frac{\partial E}{\partial z} = (i + d)\,\nabla_3^2 E + fE\,, \qquad \nabla_3^2 = \nabla_\perp^2 + \frac{\partial^2}{\partial\tau^2}\,. \tag{2.2}$$

In the real form, Eqn (2.2) is represented by equations for intensity I and phase $\Phi = \arg E$:

$$\frac{1}{2}\frac{\partial I}{\partial z} + \nabla_3(I\nabla_3\Phi) = I\,\mathrm{Re}\,f + d\left[I^{1/2}\Delta_3 I^{1/2} - I^{-1}(I\nabla_3\Phi)^2\right], \tag{2.3}$$

$$\frac{\partial\Phi}{\partial z} + (\nabla_3\Phi)^2 - I^{-3/2}\Delta_3 I^{1/2} - \mathrm{Im}\,f = dI^{-1}\nabla_3(I\nabla_3\Phi)\,. \tag{2.4}$$

The dissipative terms are grouped on the right-hand sides of these equations. Correspondingly, the conservative limit is realized under the conditions that $\mathrm{Re}\,f = 0$ and $d = 0$. According to Eqn (2.3), the quantity $\mathbf{S}_3 = I\nabla_3\Phi$ has the meaning of the energy flux density, i.e., the Poynting vector in the paraxial approximation.

The initial conditions specify the envelope distribution at $z = 0$. The above equations allow determining the distribution of the complex envelope E or the real intensity I and phase Φ in the three-dimensional space $\mathbf{r}_3 = \{x, y, \tau\}$ for each fixed z. The phase of radiation is indefinite at zero intensity, which is equivalent to two conditions: $\mathrm{Re}\,E = 0$, $\mathrm{Im}\,E = 0$. Correspondingly, these are surfaces in the space $\{x, y, z, \tau\}$ and lines in the $\mathbf{r}_3$-space (with z fixed). When traveling around such a line in the $\mathbf{r}_3$-space along a closed loop in a small neighborhood of a plane, locally orthogonal to it, the radiation phase changes by $2\pi m$, where the integer m is the topological charge of the line. We will call such lines vortex lines, because the energy flux in their neighborhood forms a vortex. The energy flux lines in the $\mathbf{r}_3$-space, whose tangent at every point of the line is parallel to $\mathbf{S}_3$, are determined by the equations

$$\frac{\mathrm{d}x}{\mathrm{d}l} = S_x\,, \qquad \frac{\mathrm{d}y}{\mathrm{d}l} = S_y\,, \qquad \frac{\mathrm{d}\tau}{\mathrm{d}l} = S_\tau\,, \tag{2.5}$$

where l is the line length measured from its arbitrary point. Singular elements of dynamic system (2.5) correspond to the condition $\mathbf{S}_3 = 0$. The singularities arise, first, at the zero phase gradient, $\nabla_3\Phi = 0$. This vector equality is generally satisfied only at isolated points in the $\mathbf{r}_3$-space. Second, singular elements correspond to the condition of zero intensity, $I = 0$, or $\mathrm{Re}\,E = \mathrm{Im}\,E = 0$, which coincides with the equation for vortex lines.

To compare with the hydrodynamics, we interpret Eqn (2.3) as a continuity equation, in which the intensity I is likened to the density of a fluid, the phase gradient $\nabla_3\Phi$, to its velocity, and the Poynting vector $\mathbf{S}$, to the flux density. Then, the right-hand part of Eqn (2.3) acts as 'external' sources of sinks of the 'fluid.' The optical fluid motion turns out to be vortex-free everywhere except on the vortex lines.

The initially considered three-dimensional scheme (or, to be precise, the system with dimension $(3 + 1)$ taking into consideration the evolution variable, too) allows a reduction of dimensionality to $(2 + 1)$ (Fig. 1c) and $(1 + 1)$ (Fig. 1a). For this purpose, the field in the scheme is confined by a sharp inhomogeneity of the medium characteristics, e.g., mirrors that fix the dependence of the envelope on the eliminated spatial variables. The factorization of the envelope with such fixation somewhat changes the form of the nonlinear response $f = f(I)$ in comparison to that in the initial three-dimensional analysis, but, in the cases considered below, with sufficient accuracy, the change in the function is described by renormalizing its parameters. Note that two conditions of singularity, $\mathrm{Re}\,E = 0$ and $\mathrm{Im}\,E = 0$, in the scheme with dimension $(2 + 1)$ determine lines in the three-dimensional space or points in the two-dimensional space — the centers of vortices, or wavefront dislocations. For the system dimension $(1 + 1)$, these conditions are satisfied at discrete moments of time and discrete coordinate values.

In the schemes considered, the radiation can occupy a simply connected (Fig. 1a, c, d) as well as a nonsimply connected (Fig. 1b, e) domain; the topological features arising in the latter case are considered in Section 4.2. If the scheme in Fig. 1a corresponds to the propagation of CW radiation (with time-independent intensity) in a planar waveguide with a single mode in one of the transverse directions, then the space-time analogy allows applying the results of the analysis to the propagation of radiation pulses through a single-mode optical fiber, where the nonlinear field limitation occurs in the longitudinal direction, so that the dimension of the problem is still $(1 + 1)$.

3. Regimes with homogeneous intensity distribution

Equation (2.1) has a trivial solution $E = 0$ (nonlasing regime). The regime is stable with respect to small perturbations (serves as an attractor) under the condition $\mathrm{Re}\,f_0 < 0$, which is assumed to be satisfied below. Here, $f_0 = f(I = 0)$ is the medium polarizability in the limit of small intensities ($I \to 0$).

From Eqn (2.3), an analog of the energy conservation law follows, the energy being understood as $W(z) = \int I(\mathbf{r}_3, z)\,\mathrm{d}\mathbf{r}_3$. For the derivation, we integrate Eqn (2.3) over $\mathbf{r}_3$ and arrive at the relation for the rate of energy variation in bright localized structures (with finite energy)

$$\frac{1}{2}\frac{\partial W}{\partial z} = \int I\,\mathrm{Re}\,f\,\mathrm{d}\mathbf{r}_3 - d\int |\nabla_3 E|^2\,\mathrm{d}\mathbf{r}_3\,. \tag{3.1}$$

Hence, in particular, we find that the nonlasing regime is globally stable (not only against small perturbations), if $\mathrm{Re}\,f < 0$ for all values of intensity achievable in the dynamics.

With the condition $\mathrm{Re}\,f_0 < 0$ of nonlasing regime stability taken into account, it follows from Eqn (3.1) that, for the existence of nontrivial bright localized (finite-energy) radiation structures, it is necessary that the function $\mathrm{Re}\,f(I)$, negative at small intensities, change sign upon an intensity increase. However, at high intensities, the function $\mathrm{Re}\,f(I)$ must become negative again. Indeed, otherwise, a regime uniform in the space $\mathbf{r}_3$ with infinitely increasing intensity of

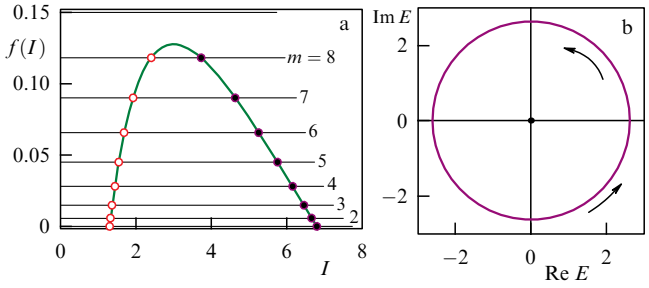

Figure 2. (Color online.) Gain/loss balance function $f(I)$ and illustration of the definition of mode intensity I_h (a). Stable regimes correspond to the right branch of $f(I)$, on which black dots are located. The quantization of topological charge m, shown in Fig. a, and the corresponding phase curve in the complex plane of envelope E, whose origin of coordinates represents the nonlasing regime (b), refer to the scheme presented in Fig. 1b; $g_0 = 2.114$, $L = 36$.

radiation could be established in the course of propagation. Therefore, for the occurrence of nontrivial bright localized structures, the function $\mathrm{Re}\, f(I)$ should turn into zero at least twice, i.e., other uniform regimes must exist in addition to the nonlasing one, which is the case of classical optical bistability. Then, the bright localized structure, the laser soliton, can be interpreted as an island of laser oscillation against the background of the nonlasing regime.

Proceeding further requires completing Eqn (2.1) using a 'material equation,' specifying the response of active and passive centers $f(I)$ in the accepted inertialess approximation. We will mainly assume that the response of the centers is described by effectively two-level schemes with a homogeneous type of spectral broadening. If the transition frequencies of these two-level systems and the carrier frequency of radiation are close to each other, then the function $f(I)$ appears to be real-valued and has the form [24]

$$f(I) = -1 - \frac{a_0}{1+I} + \frac{g_0}{1+I/b}\,. \tag{3.2}$$

On the right-hand side of Eqn (3.2), the first term (-1) corresponds to the nonresonant absorption of light by the matrix (with the chosen normalization of the evolution variable), g_0 and a_0 are the coefficients of nonsaturated gain and absorption, and b is the ratio of saturation intensities for gain and absorption. The light intensity is normalized to the saturation intensity of absorption.

In addition to the nonlasing regime, $I = 0$, Eqn (2.1) allows the existence of regimes with $\mathbf{r}_3$-independent nonzero intensity: $I = I_h = |A_h|^2 > 0$. These are plane-wave structures propagating obliquely with respect to the z-axis:

$$E = A_h \exp\left(\mathrm{i}\mathbf{K}_3\mathbf{r}_3 - \mathrm{i}K_3^2 z\right), \quad f(I_h) = dK_3^2\,. \tag{3.3}$$

We consider the conditions when $f_0 < 0$ and the function $f(I)$ has a maximum (Fig. 2a). Since nonresonant losses increase quadratically in the slope of K_3, its value is limited: $K_3^2 < K_{\max}^2 = \max f(I)/d$. The second equation (3.3) allows finding the intensity I_h from the crossing of the plot of the function $f(I)$ by the horizontal line, corresponding to the losses dK_3^2 (Fig. 2a). A linear analysis of stability shows that the inequality $(\mathrm{d}f/\mathrm{d}I)_{I=I_h} < 0$ serves as a stability criterion. Therefore, the left branch of solutions (with smaller I_h) is unstable with respect to small perturbations, while the right one is stable. Naturally, the mode with zero slope, $K_3 = 0$, has the greatest intensity. Note that, during propagation, the sloping structures experience a geometric shift in the x direction; therefore, in a system with a realistic (finite) aperture, they are conserved only for a limited time, proportional to the aperture size. Thus, only those structures with small wavefront slopes have physical meaning.

The quantization of topological charge shown in Fig. 2a, as well as Fig. 2b illustrating it, correspond to the scheme shown in Fig. 1b and explained below in Section 4.2. Therefore, in a certain interval of parameter values, the nonlasing regime and those of uniform lasing (continuous spectrum) are simultaneously stable.

4. One-dimensional structures

For the scheme shown in Fig. 1a with a slit resonator, the field distribution along one of the transverse directions is fixed by the unique mode of the corresponding planar waveguide. If additionally the resonator length in the direction of predominant propagation z is small (the case typical for semiconductor microresonators), then the lasing is represented by a unique longitudinal mode. The total envelope is then represented by the product $F(y,z)E(x,t)$, where the first factor describes the fixed mode structure of the field in the appropriate directions, and the second factor, depending only on one transverse coordinate x and time t, serves as an envelope for the one-dimensional problem. As noted in Section 2, the dimensionality reduction also leads to a modification of the response function (3.2), which with sufficient accuracy is reduced to a renormalization of the parameters of this function. Another way to reduce the dimensionality is averaging the envelope over the eliminated coordinates [5]. In this case, it is unreasonable to move to the accompanying coordinate frame, and the time t becomes an evolution variable:

$$\frac{\partial E}{\partial t} = (\mathrm{i}+d)\,\frac{\partial^2 E}{\partial x^2} + f\left(|E|^2\right)E\,. \tag{4.1}$$

Such a mean field approximation reducing the dimensionality was first used for lasers in Ref. [50]. Here, we ignore the matrix frequency dispersion, considering which in the approximation used would lead only to an inessential change in the form of function $f(|E|^2)$ in the present problem. Equation (4.1) can be derived from Eqn (2.1) by renotation of variables and ignoring the dependence on the 'excess' coordinates. The nonlasing regime $E = 0$ is still stable under the condition $f_0 < 0$, which we also assume to be fulfilled.

4.1 Infinite simply connected aperture

Assuming that the scheme parameters are uniform in quite a wide domain along x, we set the boundary conditions for bright localized structures of radiation as a requirement for the field to decrease at the periphery:

$$E(x = \pm\infty, t) = 0\,. \tag{4.2}$$

The plane-wave regimes have the previous form (3.3) with $\mathbf{K}_3 = K_x\mathbf{e}_x$ and $\mathbf{r}_3 = x\mathbf{e}_x$, where $\mathbf{e}_x$ is the x-axis unit vector. Stable regimes in Fig. 2a are presented by the right-hand branch of the function $f(I)$. Their spectrum is continuous with the limitation $K_x^2 < K_{\max}^2 = \max f(I)/d$.

The field distribution for stabilized structures has the form

$$E(x,t) = F(\xi)\exp\left(-\mathrm{i}\nu t\right), \qquad \xi = x - Vt\,. \tag{4.3}$$

The function F is determined by an ordinary differential equation, in which the transverse velocity of the structure V and the shift of its central frequency v play the role of eigenvalues:

$$(\mathrm{i}+d)\,\frac{\mathrm{d}^2F}{\mathrm{d}\xi^2}+V\,\frac{\mathrm{d}F}{\mathrm{d}\xi}+\left[\mathrm{i}v+f\left(|F|^2\right)\right]F=0\,. \tag{4.4}$$

The plane-wave regimes with a continuous spectrum of slopes K_x (relative to the z-axis) also obey this equation. However, it also describes a variety of other regimes with inhomogeneous intensity distribution, which are implemented upon imposing appropriate boundary conditions.

One of the classes of such structures corresponds to switching waves, when, in two parts of the (infinite) aperture, the regimes are asymptotically achieved with homogeneous intensity distribution, but different intensity levels; alternatively, such regimes are referred to as domain walls and fronts. Within nonlinear optics, switching waves, first discovered in systems with external incoherent or coherent radiation [51, 52], serve as one of the main mechanisms of forming localized structures — dissipative solitons [5, 53]. For example, the regime approaches the nonlasing one at one of the aperture edges (intensity $I \to 0$ at $\xi \to -\infty$) and a plane-wave regime at another edge ($I \to I_\mathrm{h} > 0$ at $\xi \to +\infty$).

A specific feature of laser systems without external coherent radiation is a continuous spectrum of switching waves that follows from the continuous character of plane-wave regimes. This means that, with the parameters of the system being fixed, depending on the initial conditions, switching waves are possible with the continuous velocity parameter V — the spectral parameter of Eqn (4.4). However, here again, it is necessary to add a caveat about the limited reality of such structures because of the radiation outcome through the edges of a finite-size aperture. At the same time, for localized 'bright' (with the finite 'energy' $W = \int |E|^2\,\mathrm{d}x$) structures, whose field decreases fairly fast at the periphery, such losses are absent until the structure itself is far from the aperture edge. However, they become more significant as the switching wave front or the bright soliton approaches the aperture edge. The boundary condition for structures remote from the edge, according to Eqn (4.2), has the form

$$F(\xi = \pm\infty) = 0\,. \tag{4.5}$$

The properties of one-dimensional dissipative optical solitons and their interpretation as coupled switching waves are described in Ref. [5] and original publications cited therein. The spectrum of bright solitons is discrete, which reflects the balance of energy inflow and outflow in the region of their localization. The branch of immobile structures, $V = 0$, corresponds to a symmetric intensity distribution $I(x) = I(-x)$, whereas structures having an asymmetric profile move in the x direction. Single stationary solitons are stable within a certain range of parameters, and various types of oscillations arise beyond this range. Alongside single solitons, there are complexes with various numbers of coupled solitons, which can also be immobile (with a symmetric intensity profile) and moving (asymmetric profile), including those with variable shape and motion velocity. Referring to [5] for examples, we proceed to a more detailed consideration of a related one-dimensional scheme with a ring-shaped aperture of the resonator. One of the advantages of this scheme is its limited aperture.

4.2 Ring-shaped aperture

The scheme with a ring-shaped aperture is shown in Fig. 1b; the presentation here follows Ref. [54]. Note that in this case the radiation propagates mainly in the direction of the ring axis z rather than along its perimeter, as, for example, in Ref. [55], where phase dissipative solitons were studied. With the same master equation (4.1), the boundary condition now consists of the requirement of periodicity

$$E(L, t) = E(0, t)\,. \tag{4.6}$$

The case of an infinite aperture corresponds to the limit $L \to \infty$. Due to the periodicity (4.6), plane-wave regimes with a homogeneous intensity distribution are quantized, provided that the length L is finite: $K_x = 2\pi m/L$, $m = 0, \pm1, \pm2, \ldots, \pm m_\mathrm{max}$, where m_max is the integer part of $(L/2\pi)K_\mathrm{max}$. Stable plane-wave regimes ($f'(I_{\mathrm{h},m}) < 0$) are marked with black dots in Fig. 2a; under its conditions, $m_\mathrm{max} = 8$, so that there are 17 such regimes (in the numerical calculations herein, we use the parameter values $b = 10$, $a_0 = 2$, $d = 0.06$, unless stated otherwise). The meaning of m is clarified in Fig. 2b, where the dependence $E(x)$ at constant time t is depicted in the complex plane $\{\mathrm{Re}\,E(x), \mathrm{Im}\,E(x)\}$ with x varying from 0 to L; the origin of coordinates corresponds to the nonlasing regime $E = 0$. In a round trip along the corresponding closed contour (here, it is a circle), the phase incursion is $2\pi m$, and therefore, with the common definition of topological charge as the phase incursion along a closed path divided by 2π, m can be considered a topological charge. However, there is a specific feature caused by the fact that the domain occupied by the radiation is nonsimply connected: while the closed contour can usually be compressed into a point, it is now fixed.

The phase curve is oriented in correspondence with the direction of the x-coordinate increase (shown by an arrow in Fig. 2b); the contour is passed m times counterclockwise at $m > 0$. The energy flux (Poynting vector) component has the same value along the contour, namely, $S = I\,\mathrm{d}\Phi/\mathrm{d}x = KI_\mathrm{h} = 2\pi m I_\mathrm{h}/L$; for $m > 0$, the flux is directed along the phase curve. The case $m = 0$ is degenerate, the field phase Φ in this case is arbitrary, and there is a stochastic drift along the phase curve under the action of fluctuations.

For a relatively small size of the scheme, $L < L_\mathrm{cr}$, where L_cr is of the order of the immobile soliton width at $L \to \infty$, only plane-wave regimes (with a homogeneous intensity distribution) are realized. If $L > L_\mathrm{cr}$, the formation of structures with a nonuniform intensity profile becomes possible too; it is natural to speak about solitons if the field localization region is much smaller than the length L. For such stationary structures, expression (4.3) and master equation (4.4) are valid as before. For such structures, Fig. 3 shows the envelope amplitude profiles and phase curves at various topological charges m. Only one of the structures shown ($m = 0$, Fig. 3a) is immobile (with the velocity $V = 0$) because of symmetry, whereas other structures move. The phase curves now differ from circles; they are closed and have self-crossings. For $m = 0$, the phase curve is degenerate: it consists of a line which is passed back and forth between two end points as x changes. The ends are return points (cusps).

For the other structures in Fig. 3 that are asymmetric, the phase curves are smooth; they go round the origin of coordinates m times (counterclockwise at $m > 0$). As was pointed out above, for a scheme with dimension $(1 + 1)$, phase singularities are possible only at discrete moments of

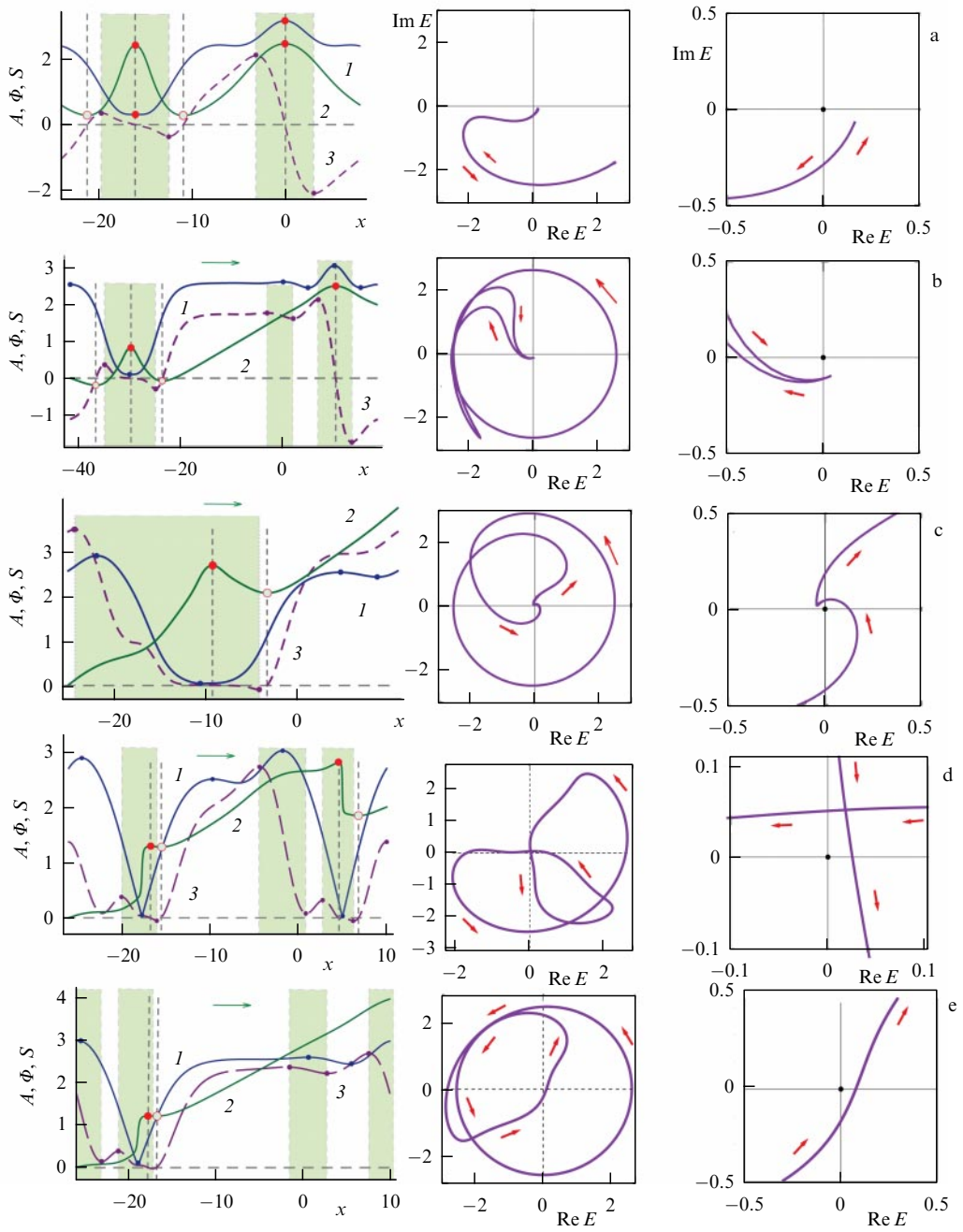

Figure 3. (Color online.) Left column: profiles of real-valued amplitude $A = |E|$ (blue curves *1*), phase Φ (green curves *2*), and energy flux $S = I(\mathrm{d}\Phi/\mathrm{d}x)$ (dashed curves *3*) of stabilized field structures. Extrema of the amplitude and phase, marked by dots, coincide only in the case of Fig. a. Vertical dashed lines indicate phase extrema and, respectively, zeros of energy flux. Shaded and unshaded strips correspond to the local decrease and increase in radiation energy. Symmetric structure in Fig. a ($m = 0$) is immobile; remaining ones are asymmetric and move in the direction indicated by the green arrow ($m > 0$). Middle column: phase curves, degenerate in the case of Fig. a, possess one (a–c, e) and two (d) returns to the origin of coordinates, corresponding to the nonlasing regime $E = 0$. Right column: magnified image of phase curves in the neighborhood of the origin of coordinates. Red arrows on phase curves show the direction of increasing x. Topological charge is $m = 0$ (a), $m = 1$ (b, d), and $m = 2$ (c, e); in Figs a, c–e, $g_0 = 2.114$, $L = 36$; in Fig. b, $g_0 = 2.116$, $L = 60$.

time and at discrete values of the coordinate. Such an event corresponds to an exact crossing of the origin of coordinates by the phase curve (see Fig. 6b below). At such moments, when the origin of coordinates is passed in the process of moving along the phase curve, the phase abruptly changes by π. In Fig. 3d, e, one can also see sharp phase jumps conserved during finite time intervals and having a magnitude different from π, but close to it. They take place as the phase curve approaches the origin of coordinates quite closely.

In the case of a significant length L, complexes of similar soliton structures and single solitons with large total phase incursion are also possible (Fig. 4). The structure shown in Fig. 4c is logically interpreted as a dark soliton with narrow intensity dips against the background of plane-wave regime intensity with oblique propagation. For all structures in Fig. 3, the phase profiles have extrema ($\mathrm{d}\Phi/\mathrm{d}x = 0$), at which the energy flux is, respectively, $S = 0$. At these points, the direction of the energy flux changes to the opposite one, so

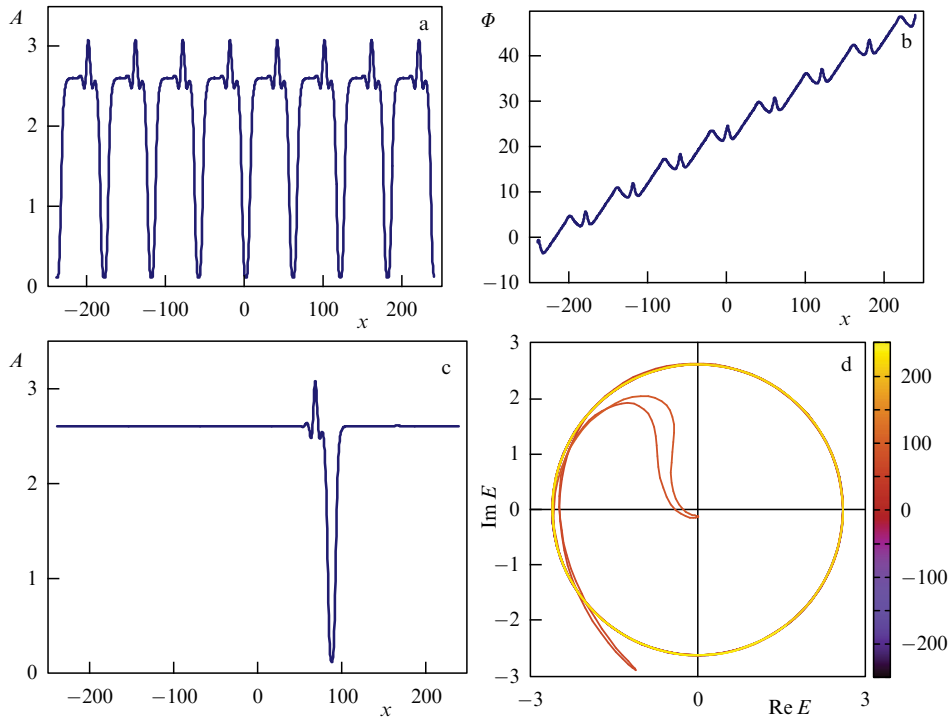

Figure 4. (Color online.) Profiles of the amplitude (a, c) and phase (b) for a complex of eight solitons (a, b) and a dark soliton (c) with a phase curve (d). Topological charge is $m = 8$, $g_0 = 2.116$, $L = 480$.

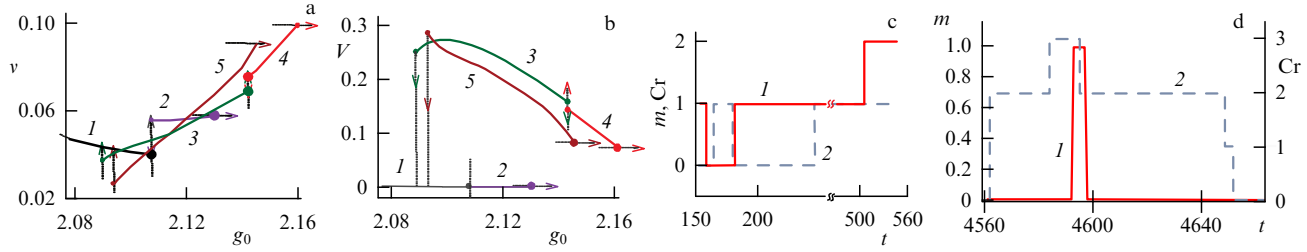

Figure 5. (Color online.) Dependence of nonlinear frequency shift v (a) and velocity V (b) on linear gain coefficient g_0 for: (*1*) symmetric fundamental structure with topological charge $m = 0$ and the only maximum of intensity (lower boundary of the stability is realized at $g_0 = 2.035$); (*2*) symmetric structure with charge $m = 0$ and three maxima of intensity (Fig. 3a); (*3*) asymmetric structure with $m = 1$ and two phase jumps by the value of $\sim \pi$ of different signs (Fig. 3d); (*4*) asymmetric structure with $m = 2$ and two positive phase jumps of $\sim \pi$; (*5*) asymmetric structure with $m = 2$ and one positive phase jump of $\sim \pi$ (Fig. 3e). Vertical arrows show transitions between structures, and horizontal arrows correspond to a transition to the regime with homogeneous intensity distribution. (c, d) Dynamics of variation in the topological charge m (solid red lines *1*) and the number of self-crossings of phase curve Cr (dashed blue lines *2*) in the case with phase incursion 2π introduced (Fig. c, $L = 36$, $g_0 = 2.114$) and with the variation in gain coefficient g_0 from 2.114 to 2.122 (Fig. d).

that the phase curves are sign changing, according to the terminology of Ref. [56]. Upon a change in the system parameters, structures also arise that oscillate or move with changing velocity and envelope profile. The interpretation of these structures as regimes of synchronization of transverse modes [57] (here, modes with homogeneous intensity distributions and different charges m) is inefficient if the number of such modes is large.

The structures presented are attractors; their stability domains are illustrated in Fig. 5a, b. Upon a smooth variation in the parameters (here, the linear gain coefficient g_0), they transform into each other without the appearance of intermediate oscillating structures, as pointed out by arrows in Fig. 5a, b. As g_0 decreases, the structure with the charge $m \neq 0$ transforms into a symmetric structure with the charge $m = 0$, which, upon a further decrease in g_0, turns into the nonlasing regime. Due to the overlap of stability domains of different structures, the phenomena of irreversible hysteresis, characteristic of dissipative systems, take place (see Section 7.3).

Thanks to the linear stability of the structures presented, the topological charge is conserved during evolution, but only when the deviations from these structures are sufficiently small. As we just have seen, the situation can change when the system parameters go beyond the stability range of the corresponding regime. Such a conclusion is also valid for the transient process of establishing stationary structures after strong initial perturbations. Paper [54] considers two kinds of such perturbations. In the first option, the initially symmetric structure ($m = 0$, Fig. 3a) is given a wavefront gradient, for which the envelope structure is multiplied by $\exp(2i\pi x/L)$. Thus, the initial structure acquires the charge $m = 1$. In the second option, after establishing a symmetric structure with the charge $m = 1$ (Fig. 3b), the gain coefficient is sharply

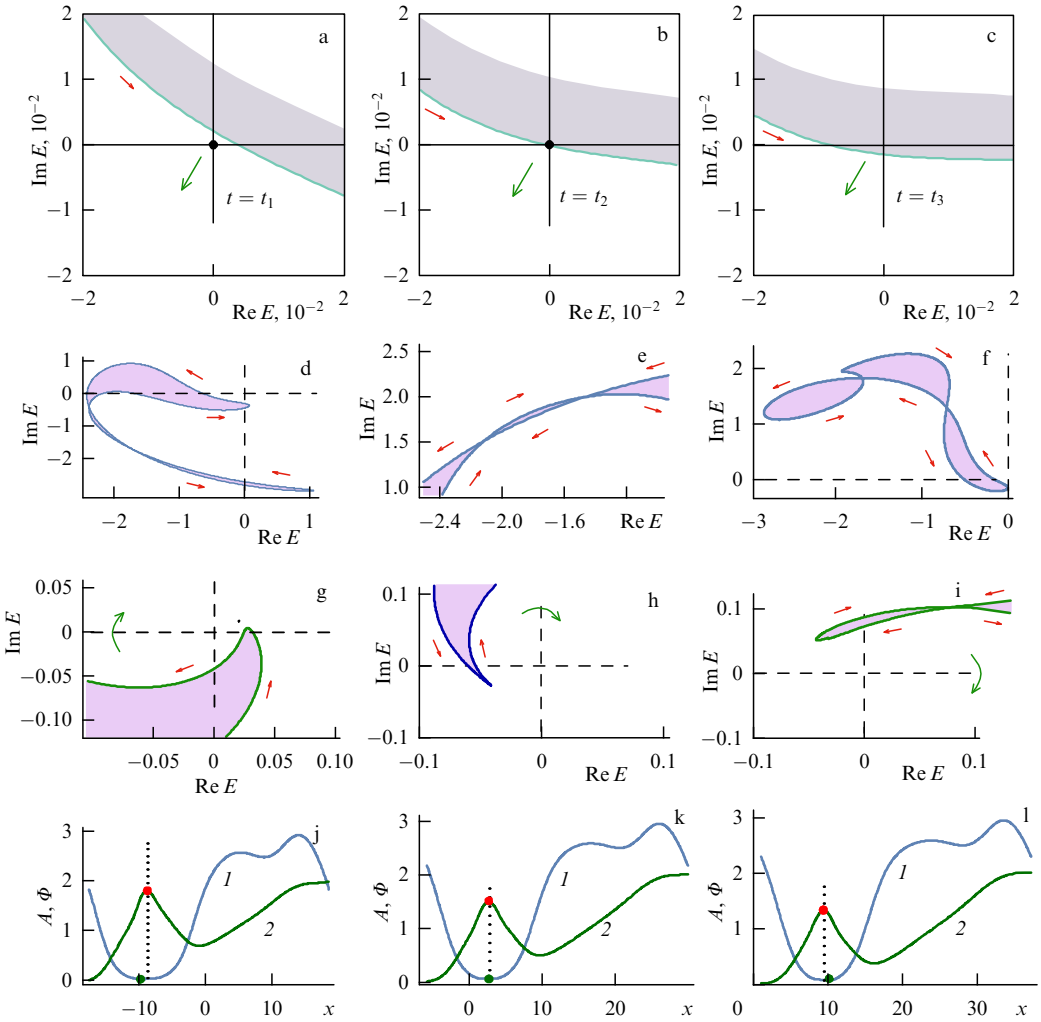

Figure 6. (Color online.) Dynamics of phase curve fragments, illustrating elementary reactions of changing topological charge m (a–c) and the number of Cr self-crossings (d–i). Moments of time: before the reaction (left column, $t = t_1$), moment of the reaction (middle column, $t = t_2$), and after the reaction (right column, $t = t_3$). Reactions may proceed in the opposite direction from t_3 to t_1 as well. Short red arrows show direction of growing x, and longer green arrows, direction of motion of phase curve fragments. Number of Cr self-crossings changes by 2 without the occurrence of cusps (d–f) and by 1 with a simultaneous formation of a cusp and its transformation (g–i) into a loop. (j–l) Profiles of the amplitude (curves *1*) and phase (curves *2*) corresponding to panels g–i; vertical dotted lines mark the position of extrema of these profiles. Figures a–c, g–i are obtained for the first variant of initial conditions, and d–f, for the second one. In Fig. a–c, $t_2 = t_1 + \delta t$, $t_3 = t_2 + \delta t$, $\delta t = 1$; in Fig. d–f, $t_1 = 161$, $t_2 = 184$, $t_3 = 200$; in Fig. g–l $t_1 = 191$, $t_2 = 248$, $t_3 = 281$.

changed (from $g_0 = 2.114$ to $g_0 = 2.122$). Then, in both cases, the establishment of stationary structures is observed. In the first case it is a structure with charge $m = 2$, shown in Fig. 3c; in the second case, the initially zero charge is temporarily increased to $m = 1$. The topological charge dynamics in the first and second case is presented in Fig. 5c and 5d, respectively.

The transformations of the structures occur in the form of a series of elementary topological reactions, shown in Fig. 6. For example, a change in the topological charge by one occurs when a fragment of the phase curve crosses the origin of coordinates (Fig. 6a–c). If, for instance, the origin of coordinates was initially located outside the phase curve topologically equivalent to a circle, then, after the above-mentioned crossing, a unit charge arises. However, this is not enough, for example, for the transition to the charge $m = 2$ shown in Fig. 5c, since in the latter case the phase curve must incorporate no fewer than two loops. The mechanism of generating additional loops requires involving self-crossings of the phase curve. Two types of changing the number of self-crossings that occur in the dynamics are presented in Fig. 6d–f and 6g–i. For the first type, one fragment of the phase curve approaches the other (Fig. 6d), touches it (Fig. 6e), and then crosses at two points (Fig. 6f). However, upon touching, the fragments have different values of the coordinate x; therefore, such an event is not critical for the envelope profile. For the change of the second type, the fragment of the phase curve strongly bends (Fig. 6g), so that a return point (cusp) is formed (Fig. 6h), from which a closed loop is then generated (Fig. 6i). Later, in the case of crossing the origin of coordinates by the branches of loops generated by cusps, the topological charge can change by a significant (integer) value relative to the initial charge, whereas in the absence of cusps it can change only by one.

Let us dwell in more detail on the cusp issue, one of the basic subjects of the catastrophe theory [58]. The necessary condition for the appearance of a singularity (cusp) on a parametric curve $\{X(x), Y(x)\}$ at point $x = x_0$ is $\mathrm{d}E/\mathrm{d}x = 0$, i.e., $\mathrm{d}X/\mathrm{d}x = 0$, $\mathrm{d}Y/\mathrm{d}x = 0$, where $X(x) = \mathrm{Re}\,E(x)$, $Y(x) = \mathrm{Im}\,E(x)$. This condition can be formulated as $\mathrm{d}A/\mathrm{d}x = 0$ and $\mathrm{d}\Phi/\mathrm{d}x = 0$, i.e., the extrema of the amplitude A (or intensity I) and the phase Φ must coincide. Therefore, the power

expansion of functions $X(x)$ and $Y(x)$ in the neighborhood of the point $x = x_0$ begins from quadratic terms (the dashes mean derivatives):

$$X(x) - X_0 = \frac{1}{2} X_0''(x - x_0)^2 + \frac{1}{6} X_0'''(x - x_0)^3 + \dots,$$
$$Y(x) - Y_0 = \frac{1}{2} Y_0''(x - x_0)^2 + \frac{1}{6} Y_0'''(x - x_0)^3 + \dots. \quad (4.7)$$

Near the cusp,

$$(x - x_0)^2 = -\frac{2(X - X_0)}{X''} = -\frac{2(Y - Y_0)}{Y_0''}.$$

Hence, it follows that at the cusp itself the phase curve slope is $\mathrm{d}Y/\mathrm{d}X = Y_0''/X_0''$ and its fragment is located in the area where $\mathrm{d}Y/\mathrm{d}X = Y_0''/X_0''$ and $\operatorname{sgn}(Y - Y_0) = -\operatorname{sgn} Y_0''$. Finally, the curvature of the phase curve is

$$K = \frac{X_0'' Y_0''' - Y_0'' X_0'''}{2(X_0''^2 + Y_0''^2)^{3/2}} \frac{1}{x - x_0}. \quad (4.8)$$

Correspondingly, the curvature, inversely proportional to the distance between a phase point and the cusp, turns into infinity at the cusp and changes its sign when passing the cusp by the point. Numerical simulations confirm these conclusions.

Note that in the reaction considered, the cusp appears and disappears instantaneously and locally at a single point of the phase curve. The number of self-crossings changes by one rather than by two, as in the first type of change. These reactions can occur on both sides, i.e., alongside an increase in topological charge or the number of phase curve self-crossings, their decrease is also possible.

In the cases considered, the events of changing the charge and the number of self-crossings alternate; the appearance of cusps is necessary but not sufficient for the above case of charge change (it is necessary that the branch of the generated loop cross the origin of coordinates). As shown in Fig. 6j–l, the appearance of cusps presented in Fig. 6g–i indeed manifests itself in the instantaneous and local coincidence of the amplitude and phase extrema of the envelope.

Note that the demonstrated violation of the topological charge conservation principle is due to the fact that the domain of field localization is nonsimply connected and does not contradict its validity in schemes with three-dimensional geometry, since the vortices — the singularities of the wave front — can leave the quasi-one-dimensional resonator or enter it from outside. Note also that the presented results of the analysis of the one-dimensional laser scheme are naturally generalized to the case of practically important optical microcavities [25, 26] and a wide class of effectively one-dimensional nonequilibrium condensates, including exciton-polariton lasers [59]. The exciton–polariton laser with saturable absorption [32] is closest to the system considered. The closeness of the process in lasers considered here to the phase slip effect known in superconductivity [60], hydrodynamics [61, 62], and electric conductivity of solids [63] should also be noted.

5. Two-dimensional structures

Let us now consider a wide-aperture laser with saturable absorption and effectively a two-level scheme, also using the mean-field approximation (with averaging of the envelope in the longitudinal direction z). The master equation differs from Eqn (4.1) only by the inclusion of the term $\partial^2/\partial y^2$ in the Laplacian, with the rest of the notation unchanged:

$$\frac{\partial E}{\partial t} = (\mathrm{i} + d)\nabla_\perp^2 E + f(|E|^2)E. \quad (5.1)$$

Here, we restrict ourselves to the case of resonators with simply connected and infinite aperture. Naturally, the conditions for both the nonlasing regime $f_0 < 0$ and the regimes with homogeneous intensity distribution $(\mathrm{d}f/\mathrm{d}I)_{I=I_\mathrm{h}} < 0$ are preserved.

The energy flux lines in a wide-aperture laser at a fixed moment of time are determined by the equations (compare with Eqn (2.5))

$$\frac{\mathrm{d}x}{\mathrm{d}l} = S_x(x, y), \qquad \frac{\mathrm{d}y}{\mathrm{d}l} = S_y(x, y). \quad (5.2)$$

The singular points (x_0, y_0) of Eqn (5.2) are found as solutions to the system of equations $S_x(x_0, y_0) = 0$, $S_y(x_0, y_0) = 0$. Since the energy flux is equal to the product of the intensity I and the phase gradient $\nabla\Phi$, there are two types of singular points. In the first case, the expansion of the envelope in the neighborhood of a singular point in small deviations from it, x and y, begins from linear terms:

$$E(x_0 + x, y_0 + y) = E_{(x)}x + E_{(y)}y + \dots, \quad (5.3)$$

where the derivatives $E_{(x)} = \mathrm{d}E/\mathrm{d}x|_{x=y=0}$, etc. are calculated at the singular point. If we restrict the expansion to the terms written down, then

$$\frac{\mathrm{d}x}{\mathrm{d}l} = qy, \qquad \frac{\mathrm{d}y}{\mathrm{d}l} = -qx, \quad (5.4)$$

where $q = \operatorname{Im}(E_{(x)}E_{(y)}^*)$. Then, the trajectories are concentric circles with the center at the singular point, and the point itself appears to be a center, i.e., is noncoarse and changes its type upon considering the next terms of expansion (5.4). Below, we will demonstrate that, for a soliton with an axially symmetric intensity distribution, this point is a focus.

For a singular point of the second type, a constant term is present in a similar expansion:

$$E(x_0 + x, y_0 + y) = E_0 + E_{(x)}x + E_{(y)}y + \frac{1}{2}E_{(xx)}x^2 + E_{(xy)}xy + \frac{1}{2}E_{(yy)}y^2 \dots. \quad (5.5)$$

Now, the energy flux becomes zero under the condition $\operatorname{Im}(E_0^* E_{(x)}) = \operatorname{Im}(E_0^* E_{(y)}) = 0$ and the flux lines are determined by the equations

$$\frac{\mathrm{d}x}{\mathrm{d}l} = \operatorname{Im}(E_0^* E_{(xx)})x + (q + p)y,$$
$$\frac{\mathrm{d}y}{\mathrm{d}l} = (p - q)x + \operatorname{Im}(E_0^* E_{(yy)})y, \quad (5.6)$$

where $p = \operatorname{Im}(E_0^* E_{(xy)})$. The character of the singular point is determined by the quantities

$$\sigma = -\operatorname{Im}(E_0^* E_{(xx)}) - \operatorname{Im}(E_0^* E_{(yy)}),$$
$$\Delta = \operatorname{Im}(E_0^* E_{(xx)}) \operatorname{Im}(E_0^* E_{(yy)}) - p^2 + q^2. \quad (5.7)$$

When $\sigma \neq 0$ and $\Delta \neq 0$, the singular point appears to be coarse, like a node, focus, or saddle. Generally, to divide the

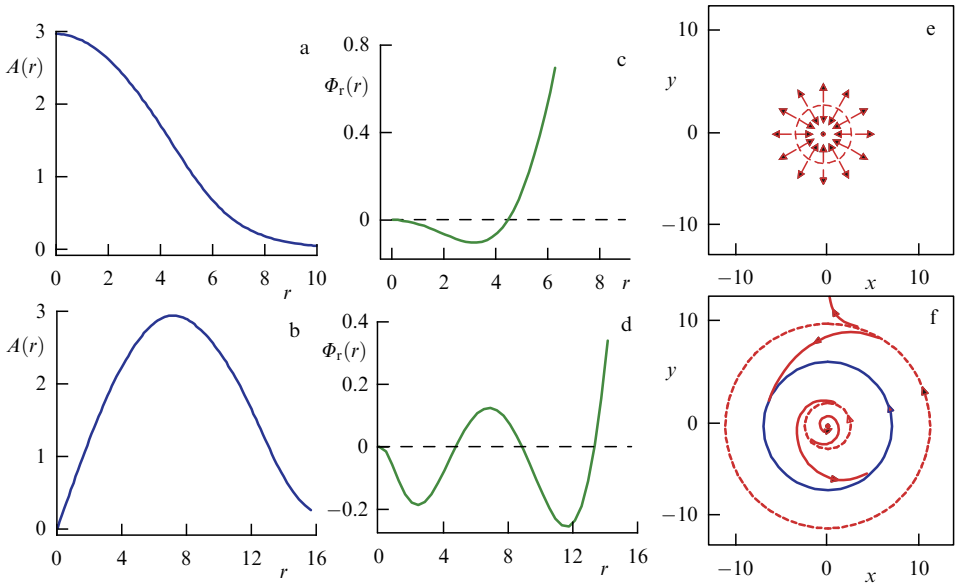

Figure 7. (Color online.) Radial profiles of the envelope amplitude (a, b), radial phase (c, d), and transverse fluxes of radiation energy (e, f); arrows show the direction of the transverse Poynting vector for fundamental ($m = 0$) (a, c, e) and vortex ($m = 1$) (b, d, f) solitons.

phase plane of energy fluxes into cells with topologically different forms of trajectories, the nonlocal elements — the limit cycles (closed trajectories with periodic variations in x and y upon changing l) — and the positions of saddle separatrices [64] should be known in addition to singular points.

5.1 Solitons with axially symmetric intensity distribution

In polar coordinates (r, φ), the envelope of solitons with axially symmetric intensity distribution has the form

$$E = A_{|m|}(r) \exp\left(\mathrm{i}m\varphi - \mathrm{i}\nu_{|m|}t\right). \tag{5.8}$$

Here, ν_m is the nonlinear frequency shift, $m = 0, \pm 1, \pm 2, \ldots$ is the topological charge, showing the phase incursion $2\pi m$ upon a round trip along a small closed loop around the soliton center $r = 0$, and $A_m(r)$ is the radial function that satisfies the equation

$$\frac{\mathrm{d}^2 A_m}{\mathrm{d}r^2} + \frac{1}{r}\frac{\mathrm{d}A_m}{\mathrm{d}r} - \frac{m^2}{r^2}A_m + \frac{\mathrm{i}\nu_m + f\left(|A_m|^2\right)}{\mathrm{i} + d}A_m = 0 \tag{5.9}$$

following from Eqn (5.1). The radial amplitude $A_m(r)$ and the frequency shift ν_m are degenerate with respect to the topological charge sign m. For bright (finite-power) solitons, the boundary conditions require finiteness at $r = 0$ and decrease at $r \to \infty$. In addition to the 'instantaneous' phase $\Phi = \arg E$, it is reasonable to introduce the 'radial' phase $\Phi_\mathrm{r} = \arg A_m$. Then, abstracting from the linear time dependence, we can present the instantaneous phase in the form $\Phi(r, \varphi) = \Phi_\mathrm{r}(r) + m\varphi$.

Solitons with $m = 0$ will be referred to as fundamental and those with nonzero m as vortex solitons because of the rotation of the energy flux around the center:

$$\mathbf{S}_\perp = \left|A_m(r)\right|^2\left(\frac{\mathrm{d}\Phi_\mathrm{r}}{\mathrm{d}r}\,\mathbf{e}_\mathrm{r} + \frac{m}{r}\,\mathbf{e}_\varphi\right). \tag{5.10}$$

The radial profiles of the envelope modulus and phase of such solitons are shown in Fig. 7. Near the center the amplitude is maximum for the fundamental solution and approaches zero for vortex ones. At the periphery, the amplitude of all solitons exponentially decreases.

Let us turn attention to the radial dependence of Φ_r. For a fundamental soliton, the function $\Phi_\mathrm{r}(r)$ has only one maximum (at $r = 0$) and one minimum. However, for a vortex soliton, there are two maxima and two minima of function $\Phi_\mathrm{r}(r)$. This fact affects the internal structure of the solitons determined by the structure of the energy fluxes (Fig. 7e, f). For fundamental solitons, the energy fluxes are radial; the energy flows towards the center at small r and from the center to the periphery, changing direction at a unique circle that divides the phase plane into two cells. However, for vortex solitons, there are three dividing circles — three limit cycles. Therefore, the phase plane for them consists of four cells. The dividing closed lines (in the present case circles) are an important feature of laser solitons.

Note also that the definition of the topological charge here is similar to that in conservative systems, including those described by the Gross–Pitaevskii equation for the Bose–Einstein condensate at zero temperature [65]. At the same time, the dissipativity of the laser system introduces principal changes into the dynamics — the vortex laser solitons are attractors, which is impossible in conservative systems.

5.2 Axially asymmetric solitons and soliton complexes

A large number of such structures is presented in Ref. [5] and papers cited therein. A general feature of bright laser solitons is the discrete spectrum of their eigenvalues. For a wide class of laser solitons, three eigenvalues are important, related to the symmetry of Eqn (5.1) with respect to a radiation phase shift, a shift in transverse coordinates, and rotation. Correspondingly, such solitons are characterized by the nonlinear frequency shift ν, the absolute value of the transverse velocity V, and the angular velocity Ω. These three eigenvalues correspond to three integral characteristics with discrete values, namely, the power $P_z(z) = \int I(\mathbf{r}_\perp, z)\,\mathrm{d}\mathbf{r}_\perp$, the transverse energy flux $\mathbf{P}_\perp(z) = \int \mathbf{S}_\perp(\mathbf{r}_\perp, z)\,\mathrm{d}\mathbf{r}_\perp$, and the axial component of the angular momentum $M_z(z) = \int (xS_y - yS_x)\,\mathrm{d}\mathbf{r}_\perp$.

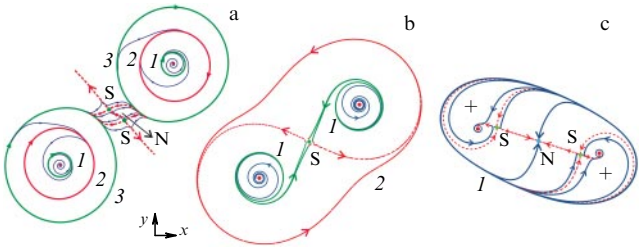

Figure 8. (Color online.) Energy fluxes for two vortex solitons in the cases of weak (a), strong (b), and superstrong (c) coupling, distinguished by the presence and number of limit cycles, individual for the vortices. Singular points are stable foci, around which flux lines are wound (centers of vortices are marked by red dots), saddles S, and nodes N. Limit cycles and separatrices of the saddles divide the phase plane into cells with topologically different characters of flux lines, whose direction is indicated by arrows. Peripheral region of the fluxes is not shown.

Let us consider examples of coupled pairs of vortex solitons illustrating three types of their coupling. Figure 8a shows the phase plane of energy fluxes in the case of *weak coupling* — each of the solitons preserves three individual closed lines (slightly deformed circles). For *strong coupling* (Fig. 8b), the outer individual closed lines are collectivized, but each dislocation, understood as a vortex center or a singular point of the wave front, still has one individual limit cycle. Finally, in Fig. 8c we see an example of *superstrong coupling*, when the dislocations have no individual limit cycles at all [66]. These solitons are rigid ones, in which the distributions of intensity and energy flux do not change in time up to a shift of transverse coordinates and rotation as a whole. Depending on the symmetry of these two distributions, four types of 'Euler mechanics' motion presented in [5] are implemented: fixed structure, uniform rectilinear motion of the structure along the axis of symmetry, rotation around the fixed center of symmetry, and so-called lunar motion. In the last, the center of the structure moves along a circle and the structure itself rotates around this center with the same period. The complexes shown in Fig. 8 possess an inversion symmetry and, therefore, rotate around the center of symmetry with a constant angular velocity. Paper [5] also presents a scheme of a 'soliton collider,' in which the formation of strongly coupled soliton complexes is implemented upon collision of individual vortex solitons.

5.3 Polarization singularities

5.3.1 Paraxial scalar solitons. Above, we considered scalar structures of radiation, in which one polarization component dominates, disregarding the second one. More general is the case of vector (polarization) structures with elliptic polarization. Such structures possess a much richer but less studied topology [67–71]. We have already met two-dimensional structures with isolated phase singularities, characterized by an integer topological charge. For two-dimensional vector structures, nonisolated (edge) phase dislocations, located on lines, are also realized. In this section, the attention will be mainly focused on polarization singularities (see also [5, 72] and Section 7.4). For these singularities, the choice is indefinite between the major and minor axis of the polarization ellipse (purely circular polarization, C-points) or between the clockwise and counterclockwise rotation of the electric field strength vector along the polarization ellipse (purely linear polarization, L-points). An analog of the integer topological charge m for isolated phase singularities is the half-integer or integer Poincaré index η — the number of turns of the major axis of the polarization ellipse during a round trip along a small-radius circle around a polarization singularity [70, 71]. In degenerate cases, singularity points may form lines or even fill aperture areas.

Following Ref. [73], we describe the dynamics of two-dimensional polarization structures in a wide-aperture laser using the quasioptical approximation and the mean field approximation, replacing the scalar equation (5.1) with a system of equations of the same type for the amplitudes of the envelope Cartesian components $\mathbf{E} = \{E_x, E_y\}$ or the amplitudes of circular polarizations $E_\pm = (E_x \pm \mathrm{i}E_y)/\sqrt{2}$. Note that both types of components can be separately detected, so that it is reasonable to consider phase singularities in any polarization components. For semiconductor vertical-cavity surface-emitting lasers, we accept the spin-flip model [74, 75]. Neglecting rapid oscillations of populations that are of minor importance for the analysis of the transverse radiation structure, we write the corresponding system of two dimensionless equations:

$$\frac{\partial E_\pm}{\partial t} = (\mathrm{i} + d)\nabla_\perp^2 E_\pm + f_\pm(I, \delta I)E_\pm \,. \tag{5.11}$$

Here,

$$\begin{aligned} f_\pm(I, \delta I) &= -1 - \frac{a_0}{1+I} + (1 - \mathrm{i}\alpha)g_\pm(I, \delta I)\,, \\ g_\pm(I, \delta I) &= N\left(1 \pm \frac{\varepsilon_J b \delta I}{1 + \varepsilon_J b I}\right), \\ N &= \frac{g_0}{1+bI}\left[1 - \frac{\varepsilon_J b^2 \delta I^2}{(1+bI)(1+\varepsilon_J bI)}\right]^{-1}, \end{aligned} \tag{5.12}$$

$I = |E_+|^2 + |E_-|^2 = |E_x|^2 + |E_y|^2$ is the total intensity, $\delta I = (|E_-|^2 - |E_+|^2)$ is the difference between intensities of circular components, α is the alpha factor characterizing semiconductor lasers, and the dimensionless parameter ε_J is determined by the ratio of relaxation rates and appears to be small, $1/201 \leqslant \varepsilon_J \leqslant 1/3$ [74].

At $\varepsilon_J = 0$, the functions f_+ and f_- coincide and depend only on the total intensity I ($f_+ = f_- = f(I)$). In this case, there is a family of solitons with a continuously varying parameter, generated by a scalar soliton — one of the above stable solutions of the scalar equation (5.1). For example, in an axially symmetric distribution of intensity, the coordinate dependence of scalar vortex solitons can be presented in the form $E_s(r, \varphi) = A_{|m|}(r)\exp(\mathrm{i}m\varphi)$ (taking into account the degeneracy of solutions of Eqn (5.9) with respect to the topological charge sign). Then, the solution of Eqn (5.11) will be a family of solitons:

$$\begin{aligned} E_+(r, \varphi) &= \exp(\mathrm{i}m_+\varphi)A_{|m_+|}(r)\cos\theta\,, \\ E_-(r, \varphi) &= \exp(\mathrm{i}m_-\varphi)A_{|m_-|}(r)\sin\theta\,, \end{aligned} \tag{5.13}$$

with $m_+ = -m_-$ and arbitrary parameter θ (the mutual time-dependent factor is omitted). The continuous spectrum of such dissipative solitons is explained by the invariance of the master equations with respect to rotations in the plane of intensities (I_+, I_-).

However, for $\varepsilon_J > 0$, when the functions f_+ and f_- differ and also depend on the difference among intensities of polarization components, the degeneracy is removed and the

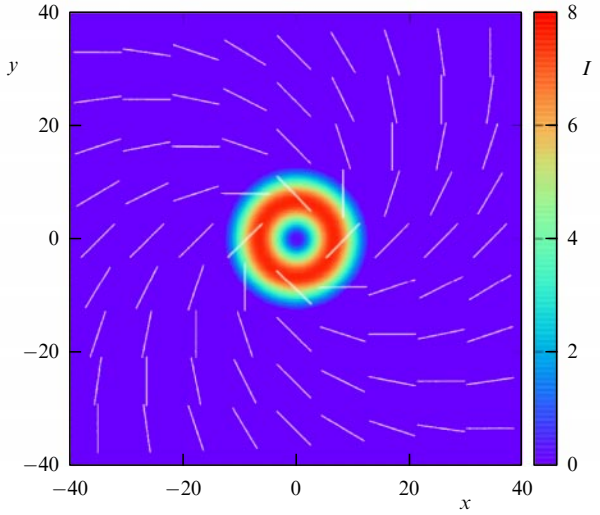

Figure 9. (Color online.) Direction of linear polarization (light segments) and distribution of total intensity (color scale on the right) for the vector soliton of the form (5.13) with $m_+ = -m_- = 1$; $\varepsilon_J = 0.04$.

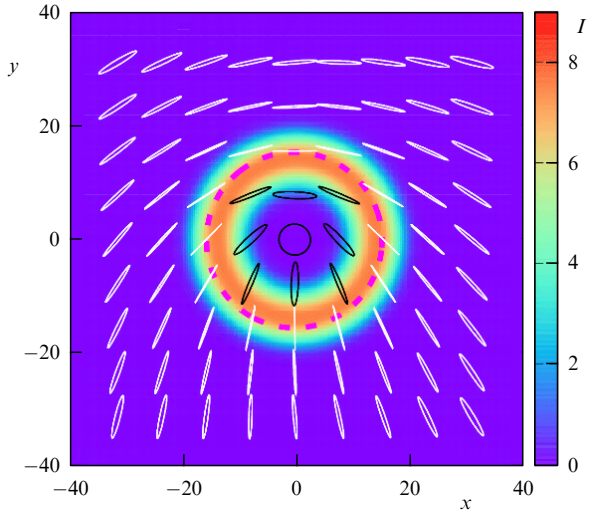

Figure 10. (Color online.) Polarization ellipses and distribution of total intensity (color scale on the right) for topological charges $m_+ = 2, m_- = 3$; $\varepsilon_J = 0.04$. White ellipses correspond to left-hand polarization, black ellipses, to the right-hand one. Dashed circle is the L-line, on which the polarization of radiation is linear.

continuous spectrum of soliton structures turns into a discrete one. At the initial moment of time, E_+ and E_- can be specified in the form (5.13) with $m_+ = -m_-$. It appears that, with time (the longer the time, the smaller ε_J), the intensities of components with opposite signs of the topological charge equalize. The resulting vector structure illustrated in Fig. 9 possesses linear polarization and the Poincaré index $\eta = 1$ all over the laser aperture.

More generally, the topological charges of circular polarization components can differ in moduli, too. If the difference between moduli is not large, then a vector soliton with a more complex polarization structure is established. Figure 10 shows such a structure for a soliton with the topological charge of two circular polarizations $m_+ = 2$ and $m_- = 3$. It is seen that, in the center, the polarization is circular, on the circle with the radius corresponding to the outer radius of the total intensity ring, the polarization is purely linear (L-line), and in the peripheral region, it is elliptic with the direction of rotation opposite to that in the central region. The Poincaré index $\eta = 1/2$, i.e., when passing around the singular point, the polarization ellipse rotates half a turn. For the Cartesian polarization component E_x, Fig. 11 shows the presence of an edge dislocation at $m_+ = -m_- = 1$ ($E_x = 0$ on the line $x = 0$) and isolated phase dislocations at different topological indices of the circular components but that are close in modulus. A more complete set and analysis of laser solitons with polarization singularities is presented in Ref. [73].

5.3.2 Manifestations of nonparaxiality. Our consideration in Section 5.3.1 was based on the quasioptical (paraxial) approximation valid for beams whose width considerably exceeds the wavelength. As the beam width decreases, the role of nonparaxiality effects increases. Such effects manifest themselves, first of all, in the complication of the polarization structure of radiation. In the case of fairly wide beams, the effects of weak nonparaxiality have been analyzed in Ref. [76] (see also [5]) for fundamental laser solitons and in Ref. [77] for vortex solitons.

In the paraxial approximation, the polarization of radiation was considered the same all over the laser aperture. However, from the Maxwell equation for the electric induction $\tilde{\mathbf{D}}$,

$$\operatorname{div} \tilde{\mathbf{D}} = 0\,, \tag{5.14}$$

in the weakly-nonparaxial approximation, it follows that

$$E_z \approx \frac{\mathrm{i}}{k_0} \operatorname{div}_\perp \mathbf{E}_\perp \to \frac{\mathrm{i}}{k_0} \frac{\partial E_x}{\partial x}\,. \tag{5.15}$$

The approximation makes use of the fact that the parameter $(k_0 w)^{-1}$ is small, where w is the characteristic soliton width. The other polarization component E_y and the corrections to the main component E_x arise only in higher orders of the parameter $(k_0 w)^{-1}$. Hence, the polarization is generally elliptic and changes over the transverse section. It is remarkable that the polarization ellipses are located in the plane including the z-axis (the main direction of the radiation propagation) rather than orthogonal to it. Allowing for the component E_y reveals a small slope of the ellipses, which will be disregarded below.

For a vortex soliton with axially symmetric intensity distribution in the paraxial approximation,

$$E_x(r, \varphi) = A_m(r) \exp(\mathrm{i}m\varphi) = (x + \mathrm{i}y)^m B_m(x^2 + y^2)\,, \tag{5.16}$$

where $A_m(r) = r^m B_m(r^2)$. Expression (5.16) can be presented in the form

$$E_x = |E_x| \exp(\mathrm{i}\Phi_x)\,, \qquad \Phi_x = m\varphi + \arg B_m(r^2)\,. \tag{5.17}$$

Then, according to (5.15),

$$E_z(r, \varphi, z) = |E_z| \exp(\mathrm{i}\Phi_z)\,, \tag{5.18}$$

where the phase is given by

$$\Phi_z = \frac{\pi}{2} + (m-1)\varphi + \arg\left[mB_m + 2r^2 \exp(\mathrm{i}\varphi) \cos\varphi \frac{\mathrm{d}B_m}{\mathrm{d}r^2}\right]. \tag{5.19}$$

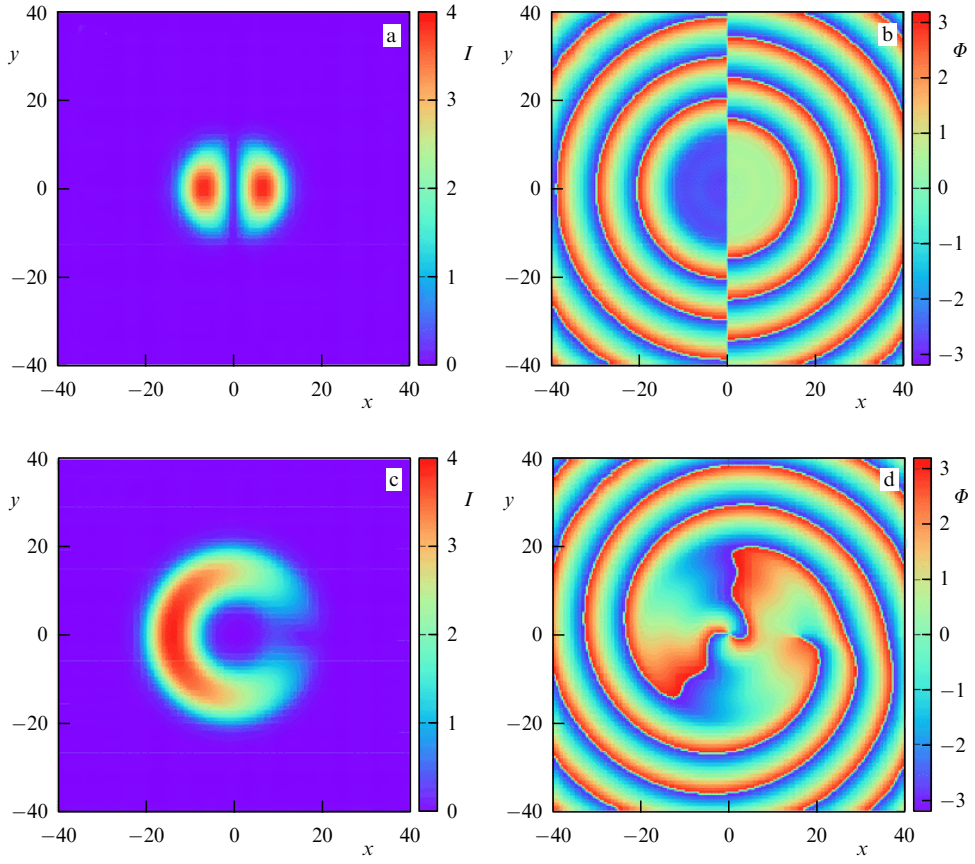

Figure 11. (Color online.) Transverse distributions of intensity I and phase Φ of Cartesian polarization component E_x: (a, b) $m_+ = -m_- = 1$, (c, d) $m_+ = 2$, $m_- = 3$. Intensity distribution for component E_y is rotated by $\pi/2$.

The elliptic polarization turns linear if

$$\delta\Phi = 0 \quad \text{or} \quad \delta\Phi = \pi\,, \tag{5.20}$$

where $\delta\Phi = \Phi_z - \Phi_x$. The direction of rotation of the electric field strength vector $\tilde{\mathbf{E}}$ along the polarization ellipse is determined by the sign of $\sin\delta\Phi$ and changes to the opposite one upon a change of this sign. From Eqns (5.17) and (5.19), it follows that

$$\operatorname{sgn}\sin\delta\Phi = \operatorname{sgn}\left(x\,\frac{\mathrm{d}}{\mathrm{d}r}\left|A_m(r)\right|\right). \tag{5.21}$$

According to Eqn (5.21), condition (5.20) is satisfied on two L-lines within the laser aperture (x, y), which are shown in Fig. 12. The first of them is a straight line coincident with the axis $x = 0$ (it is orthogonal to the direction of the main polarization of radiation). The second L-line is a circle on which the intensity of the paraxial soliton is maximum (see Fig. 7). The entire aperture is divided by these lines into four cells with opposite directions of rotation of vector $\tilde{\mathbf{E}}$ along the polarization ellipse with time.

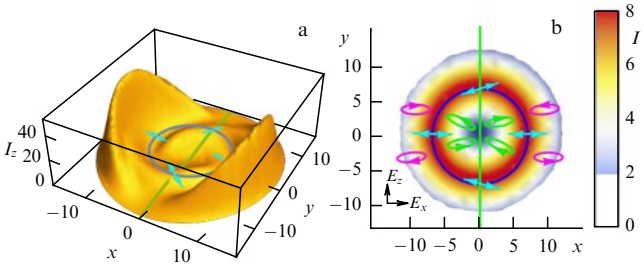

Figure 12. (Color online.) Distributions of amplitude (a) and intensity (b) of a two-dimensional weakly nonparaxial soliton with topological charge $m = 1$ in the (x, y)-plane (color scale on the right) and a schematic representation of polarization ellipses in the (E_x, E_z)-plane; arrows show the direction of vector $\tilde{\mathbf{E}}$ rotation. Polarization in Fig. b becomes linear on the circle, where the intensity of a paraxial soliton is maximum, and on the axis $x = 0$ (L-lines).

6. Scheme with external coherent signal

The topology of radiation in effectively two-dimensional laser schemes is much richer than in one-dimensional ones, which makes urgent the problem of controlling this topology. As is known, by means of weak and smooth transverse inhomogeneities, it is possible to control the motion and localization of solitons of various types, and the change in the structure topology can be achieved upon the collision of solitons ('soliton collider' scheme) [5]. In this section, we will demonstrate a relatively simple and efficient method of controlling the topology of structures using a weak external coherent holding radiation [66].

The dimensionless master equation for the laser field envelope with rapidly saturated absorption and a weak holding signal — a plane monochromatic wave with amplitude E_{in} — in the mean field approximation is conveniently written considering the frequency of the signal as the carrier

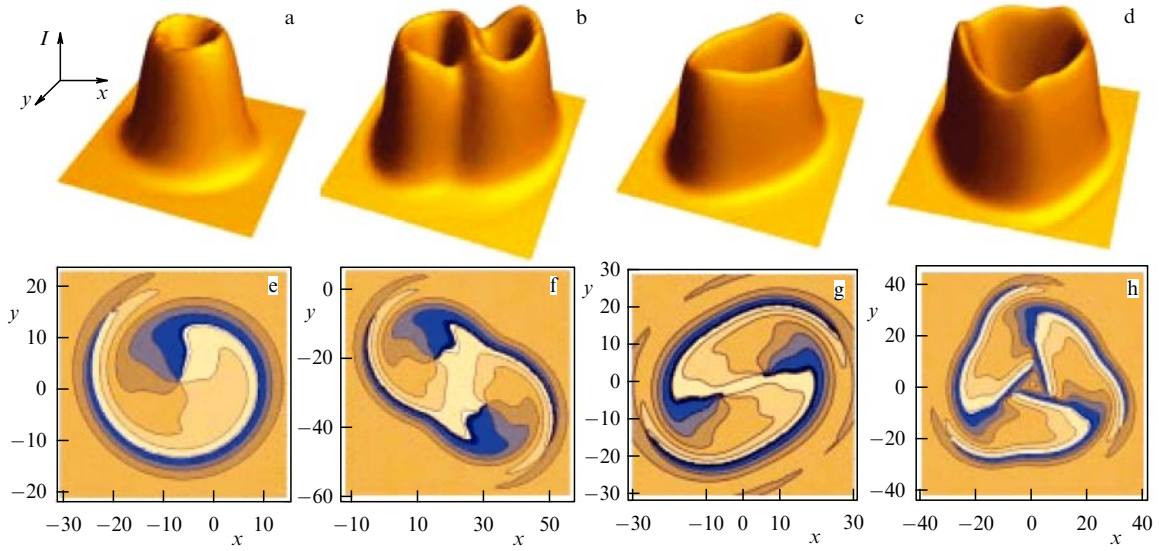

Figure 13. (Color online.) Transverse profiles of intensity (a–d) and phase isolines (e–h) for solitons arising from free axially symmetric solitons with topological charge $m = 1$ (a, e), $m = 2$ (b, c, f, g), and $m = 3$ (d, h) upon introducing the holding radiation with amplitude $E_{\text{in}} = 0.01$. Parameters: $g_0 = 2.10$ (a, e), 2.11 (b, f), 2.09 (c, d, g, h); $\theta = 0.08$ (a, e), 0.06 (b, f), 0.01 (c, g), 0.015 (d, h).

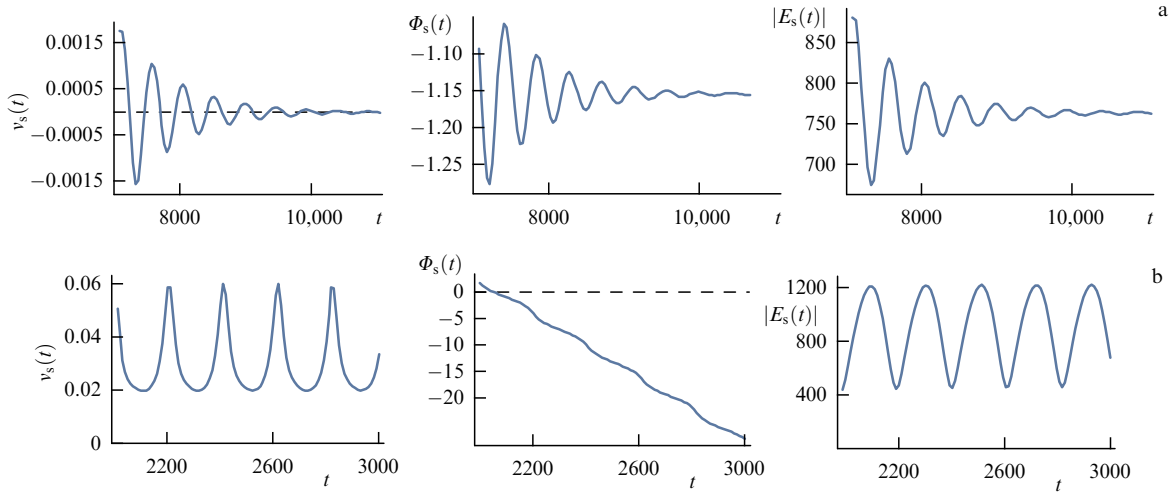

Figure 14. (Color online.) Time dependence of instantaneous integral frequency ν_s, integral phase Φ_s, and modulus of integral field E_s upon the establishment of the synchronization regime (a) and periodical beats (b) of a triangular soliton ($m_0 = 3$, Fig. 9d); $g_0 = 2.09$, $E_{\text{in}} = 0.01$, $\theta = 0.015$ (a), 0 (b).

frequency [21]:

$$\frac{\partial E}{\partial t} = (\mathrm{i} + d)\left(\frac{\partial^2}{\partial x^2} + \frac{\partial^2}{\partial y^2}\right)E + \mathrm{i}\theta E + f\left(|E|^2\right)E + E_{\text{in}}\,. \quad (6.1)$$

Here, θ is the detuning of the frequency of the resonator longitudinal mode from the frequency of the holding radiation, considered to be small. We preserve the domain of parameters in which at $E_{\text{in}} = 0$ there are laser solitons, presented in Figs 7 and 8, and assume that the amplitude of the holding radiation is much smaller than their maximal amplitude, $|E_{\text{in}}| \ll |E|_{\max}$.

Consider the influence of the weak holding radiation on a singular vortex soliton with the axially symmetric intensity profile and topological charge m. In the soliton periphery, instead of the zero field, a background with the small amplitude $E_{\text{b}} \approx -E_{\text{in}}/(f_0 + \mathrm{i}\theta)$ is established. The soliton remains stable if the parameters are not close to the boundaries of the soliton stability domain in the absence of the holding radiation. Correspondingly, the 'driven' soliton can be considered to be a result of interference between a 'free' laser soliton and the low-amplitude background.

The presence of holding radiation leads, first of all, to the violation of central symmetry of a vortex soliton ($m \neq 0$), so that such structures begin to move, remaining rigid, and/or oscillate at any values of E_{in} and θ. Then, the multiple central dislocation with the charge m ($|m| > 1$) splits into $|m|$ dislocations with unit charge. Simultaneously, $|m|$ dislocations with opposite-sign unit charges move from the periphery and approach the center. As E_{in} increases, the central and peripheral dislocations draw together, ultimately merge, and annihilate, as $|E_{\text{in}}|$ exceeds the critical value. The intensity distribution becomes slightly asymmetric, as shown in Fig. 13 for 'driven' solitons with initial topological charges from $m = 1$ (Fig. 13a, e) to $m = 3$ (Fig. 13d, h).

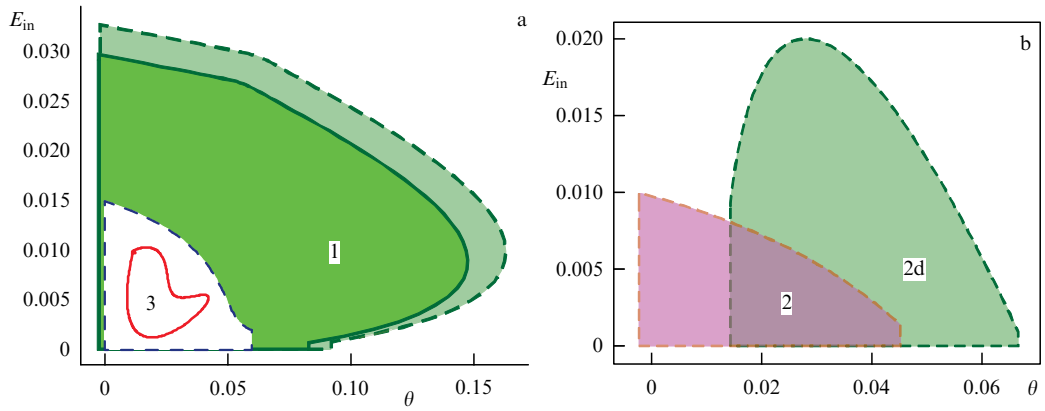

Figure 15. (Color online.) Boundaries of domains of synchronization (solid lines) and periodical beats (dashed lines) of solitons with initial topological charge $m_0 = 1, 3$ (a) and $m_0 = 2$ (b) (values of m_0 are indicated inside the domains). Domain 2d corresponds to the soliton with strong coupling (Fig. 9c); $\min I_{in,\,thr} \approx 10^{-5}$, $g_0 = 2.09$ (domains 1–3), $g_0 = 2.11$ (2d).

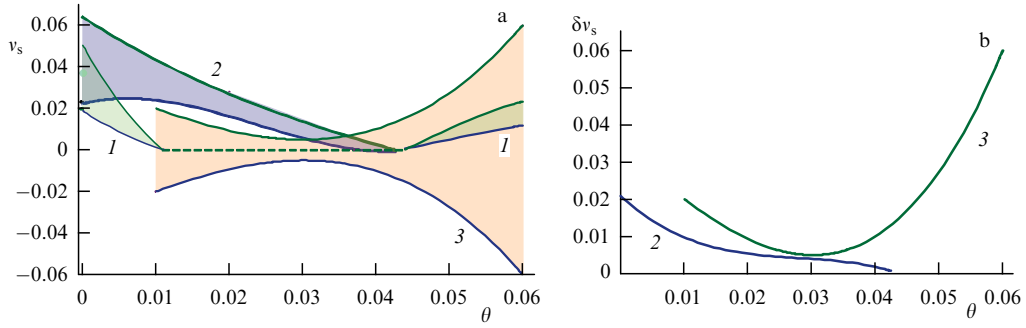

Figure 16. (Color online.) Boundaries of time variations of instantaneous frequency v_s (a) and the amplitude of its changes (b), depending on detuning θ for a driven triangular soliton with strong coupling (region *1*, $m_0 = 3$ (Fig. 9d)), a soliton with superstrong coupling (region *2*, $m_0 = 2$ (Fig. 9c)), and a soliton with strong coupling (region *3*, $m_0 = 2$ (Fig. 9c)). Horizontal dashed line corresponds to complete synchronization. In regions *1* and *2*, $E_{in} = 0.005$, $g_0 = 2.09$; in region *3*, $E_{in} = 0.010$, $g_0 = 2.11$.

At $|m| = 1$ and very small amplitudes E_{in}, the central and peripheral dislocations rotate around the soliton center with an angular velocity close to the difference in frequencies between the free soliton (with the nonlinear frequency shift taken into account) and the holding radiation. Due to the arising weak asymmetry of the intensity distribution, this structure is not rigid. When E_{in} exceeds a certain threshold $E_{in,\,thr}$, synchronization occurs, and the structure becomes rigid. Hence, the distributions of intensity and energy fluxes are stationary in the coordinate frame associated with the structure. The transient process is shown in Fig. 14a for integral characteristics

$$E_s(t) = \int E(x, y, t)\,dx\,dy\,, \quad \Phi_s(t) = \arg E_s\,, \quad v_s(t) = \frac{d\Phi_s}{dt}\,. \tag{6.2}$$

However, such synchronization is realized only in a certain domain of the system parameters. Beyond this domain, either the regime of periodic beats is established (Fig. 14b) or a transformation or destruction of the localized structure occurs. The domains of parameters corresponding to different structures are shown in Fig. 15. Upon exiting beyond the boundary of the stability domain of periodic beats (shaded areas), the following scenarios of the merging of central and peripheral dislocations (vortex centers) are observed. If the exit from the domain occurs at the expense of an increase in the detuning θ, then the central dislocations move off the center and annihilate with the peripheral dislocations. On the contrary, upon the loss of stability at constant θ and growing E_{in}, the peripheral dislocations approach the center, where their annihilation with the central ones occurs already in the region of high intensities. If $|m| > 1$, then, upon an increase in θ with E_{in} kept unchanged, the split central dislocations reach the periphery and annihilate with peripheral ones in sequential pairs. When E_{in} decreases to zero at constant detuning θ, a transition to a soliton, free but asymmetric at $|m| > 1$, occurs, only if such a soliton is stable at the given values of gain g_0. Otherwise, the structure disperses with the establishment of nonlasing regime $E = 0$ all over the laser aperture.

In Fig. 16, we show the range of variation for the instantaneous frequency $v_s(t)$ for steady-state solitons. Under the assumed conditions, the complete synchronization with $v_s(t) \equiv 0$ is achieved only for a soliton with a unit topological charge (dashed line). Other solitons experience periodic beats all over the stability domain.

Finally, Fig. 17 demonstrates the phase plane of the radiation energy fluxes for the driven solitons shown in Fig. 13. Cases of strong coupling are presented, when there is one individual limit cycle for each of the two main dislocations (Fig. 17b) and superstrong coupling without individual limit cycles (Fig. 17c, d). Solitons generated by the axially symmetric vortex soliton with $m_0 = 1$ (Fig. 17a) and the triangle soliton with $m_0 = 3$ (Fig. 17d) are rigid; they are synchronized by the holding radiation. At $m_0 = 2$,

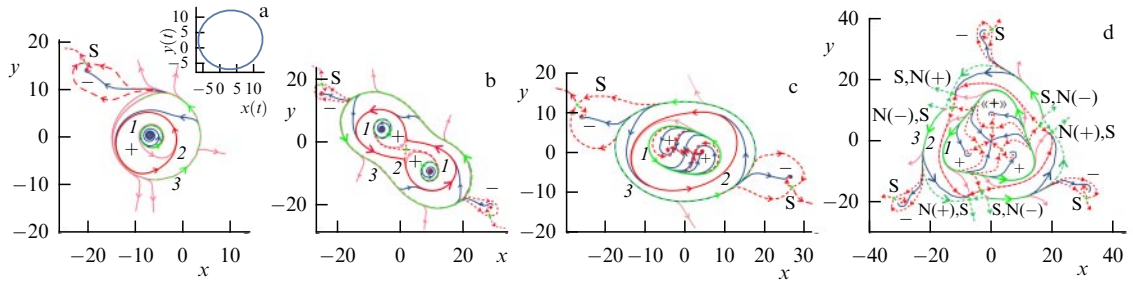

Figure 17. (Color online.) Energy fluxes for guided solitons, arising from initial axially symmetric solitons with topological charge $m_0 = 1$ (a), 2 (b, c), and 3 (d). Plus and minus signs indicate the sign of central and peripheral dislocations (focus-type singular points). Closed curves *1* are unstable limit cycles; in panels a–c, closed curves *2* and *3* are stable and unstable limit cycles; in d, closed curve *2* is a stable limit cycle, and *3* is a line composed of separatrix lines, including saddle (S)–node (N) pairs. Stable and unstable nodes are denoted, respectively, as N(+) and N(−). Closed curves separate cells with different topologies of radiation energy fluxes. Inset in panel a demonstrates the circular trajectory of soliton center $\mathbf{R}_c(t)$. Parameters are $g_0 = 2.10$ (a), 2.11 (b), 2.09 (c, d); $E_{in} = 0.010$ (a, b), 0.005 (c, d); $\theta = 0.08$ (a), 0.06 (b), 0.03 (c), and 0.037 (d).

the solitons are not completely synchronized; periodic beats with small amplitude (about 2%) manifest themselves in their structure. The motion of solitons obeys the 'Euler mechanics' of rigid dissipative structures [5]. So, at $m_0 = 2$ (Fig. 17b, c) and $m_0 = 3$ (Fig. 17d), there are axes of rotation of the second and third order. Therefore, the solitons considered rotate around the fixed center of symmetry with a constant angular velocity. At $m_0 = 1$ (Fig. 17a), there are no elements of symmetry. Then lunar motion is realized: the energy center of solitons, $\mathbf{R}_c(t) = \int \mathbf{r}_\perp I(\mathbf{r}_\perp, t)\, d\mathbf{r}_\perp / \int I(\mathbf{r}_\perp, t)\, d\mathbf{r}_\perp$, $\mathbf{r}_\perp = (x, y)$, moves along a circle, and the entire structure simultaneously rotates with the same period.

A slow change in the parameters allows implementing hysteresis phenomena. For example, from an axially symmetric soliton with charge $m_0 = 3$, by increasing the amplitude of the supporting radiation E_{in}, we get a rotating triangle soliton with three separated dislocations. If, then, E_{in} smoothly decreases to zero, the structure of the soliton will stay unchanged, i.e., three central dislocations will not merge and will stay separated from each other. A similar hysteresis takes place upon a change in the detuning θ for other values of m_0 as well. Such hysteresis demonstrates the bistability of axially symmetric- and triangle-type solitons, even in the absence of holding radiation.

The results presented in this section show the nontriviality of synchronization of spatially distributed systems. Even weak holding radiation can change the topology of two-dimensional vortex laser solitons and their complexes in a controllable way. This can be used to control the number and position of dislocations, as well as the character of their interaction with each other. The support of high contrast (the ratio of maximum intensity to the background one) together with the suppression of the phase drift in free solitons (see Section 9) and a rich set of guided structures of various types make their application promising for topologically protected information operations. The effects described, apparently, seem easily observable in wide-aperture semiconductor lasers combining saturable absorption [78–80] and holding radiation [81–86] schemes.

7. Three-dimensional structures

Systems with a three-dimensional geometry are the richest with various structures. The singularities of field distribution at a fixed value of the evolution variable z arise upon simultaneous turning to zero the right-hand sides of Eqns (2.5), i.e., for zero flux of the radiation energy, $\mathbf{S}_3 = 0$. Since $\mathbf{S}_3 = I\nabla_3\Phi$, two ways of satisfying this condition arise. First, there is a singularity at zero radiation intensity, $I = 0$, which is achieved under the conditions

$$\operatorname{Re} E(x, y, \tau) = 0\,, \qquad \operatorname{Im} E(x, y, \tau) = 0\,. \tag{7.1}$$

In the three-dimensional space, the last two conditions generally determine the lines having the parametric form $\{x(l), y(l), \tau(l)\}$, l being the line length. These are vortex lines, since near them the radiation energy flux has a vortex structure. The second way of implementing a singularity corresponds to the vector equality $\nabla_3\Phi = 0$, which is equivalent to three scalar conditions,

$$\frac{d\Phi}{dx} = 0\,, \qquad \frac{d\Phi}{dy} = 0\,, \qquad \frac{d\Phi}{d\tau} = 0\,. \tag{7.2}$$

Generally, Eqns (7.2) determine isolated points in the three-dimensional space $\mathbf{r}_3 = \{x, y, \tau\}$.

7.1 Vortex lines

Vortex lines exist in the linear regime as well, e.g., higher-order monochromatic Gaussian beams possess open and closed vortex lines [87]. Vortex lines with a more complex topology, including knot ones, are theoretically and experimentally demonstrated in [88] in relation to the propagation of radiation in a vacuum. However, in linear media, such structures disperse in the course of evolution and become undetectable. Below, we dwell only on nonlinear structures, paying particular attention to the specific features of their topology. First of all, let us consider the properties of vortex lines in application to laser solitons.

Topological three-dimensional laser solitons have at least one vortex line (we do not classify fundamental solitons as topological). When passing around a line in its small neighborhood in a plane, orthogonal to the line tangent, the phase incursion is $\delta\Phi = 2\pi m$ due to the field unambiguity, with integer m being the topological charge. In the systems considered, only the vortex lines with unit charge $m = \pm 1$ are stable. The orientation of the lines can be chosen such that $m = 1$. The vortex lines of the laser (dissipative) scheme interesting to us will be characterized, first, geometrically by the topological characteristics, and, second, by the features of energy fluxes.

As in linear media, these lines may be closed or open, with the ends extended to the periphery of solitons (to infinity) in the $\mathbf{r}_3$-space. An open line can be formally closed, completing

it with an arc of an infinitely large radius with the center in the neighborhood of a soliton. Asymptotically (at the periphery of bright soliton structures), the open vortex lines approach straight lines. This can be shown analytically for weakly coupled fundamental laser solitons [21]. Such individual solitons described by the localized solutions of Eqn (2.2) possess a spherically symmetric field distribution, exponentially decreasing at large distances from the soliton center with the coordinate $\mathbf{r}_n$:

$$E_n(\mathbf{r}) = A\,\frac{1}{|\mathbf{r}-\mathbf{r}_n|}\exp\left(-q|\mathbf{r}-\mathbf{r}_n| + \mathrm{i}\Phi_n\right), \qquad q = q' + \mathrm{i}q'', \quad q' > 0\,. \tag{7.3}$$

At large distances from the soliton center, it is possible to use an analog of the multipole expansion [89]: $|\mathbf{r}-\mathbf{r}_n| \to r - (\mathbf{n},\mathbf{r}_n)$, $\mathbf{n} = \mathbf{r}/r$. Then, saving the dependence upon $\mathbf{r}_n$ only in the exponent, we get for a complex of such weakly bound solitons

$$E(\mathbf{r}) \approx \frac{A}{r}\exp(-qr)\sum_n \exp\left[q(\mathbf{n},\mathbf{r}_n) + \mathrm{i}\Phi_n\right]. \tag{7.4}$$

Now, the conditions (7.1) determining the vortex lines take the form

$$\sum_n \exp\left[q'(\mathbf{n},\mathbf{r}_n)\right]\cos\left[q''(\mathbf{n},\mathbf{r}_n) + \Phi_n\right] = 0\,,$$
$$\sum_n \exp\left[q'(\mathbf{n},\mathbf{r}_n)\right]\sin\left[q''(\mathbf{n},\mathbf{r}_n) + \Phi_n\right] = 0\,, \tag{7.5}$$
$$n_x^2 + n_y^2 + n_\tau^2 = 1\,.$$

This is a system of three equations for three unknowns, n_x, n_y, n_τ, specifying the direction of the straight lines. The discrete set of solutions determines the asymptotic form of the hyperbolic-shaped vortex lines. In Fig. 18, this is illustrated by an example of a pyramidal complex of four fundamental solitons, three of which have a similar phase, $\Phi_1 = \Phi_2 = \Phi_3 = 0$, and the fourth one being in antiphase, $\Phi_4 = \pi$. Due to the presence of planes of symmetry, passing through the vertex and the altitude of a pyramid, the complex moves straight without rotation (in the accompanying reference frame). A number of other rigid complexes of fundamental three-dimensional solitons are considered in Ref. [5] (see also references therein). The asymptotic behavior of the vortex lines found numerically is close to that obtained analytically. This conclusion is also confirmed numerically for more complex localized structures.

On the very vortex line, the energy flux approaches zero, $\mathbf{S}_3 = 0$, due to which all points of the vortex line are singular for the dynamic system (2.5) (nonisolated singular points). In a local neighborhood of the vortex line, system (2.5) possesses a symmetry with respect to the axis parallel to the vortex line tangent; for definiteness, assume this axis to be the τ-axis. In the cylindrical (locally cylindrical) coordinates ρ, φ, τ the field envelope can be written in the form $E = A(\rho,\tau)\exp(\mathrm{i}\varphi)$. At small ρ, the function $A(\rho,\tau)$ is expanded into a series in odd powers of ρ: $A(\rho,\tau) = \rho f(\tau) - \rho^3 g(\tau) + \ldots$. Then, in the lowest-order approximation in ρ,

$$S_\rho = -\rho^3 F_\rho(\tau)\,, \quad S_\varphi = \rho F_\varphi(\tau)\,, \quad S_\tau = \rho^2 F_\tau(\tau)\,, \tag{7.6}$$

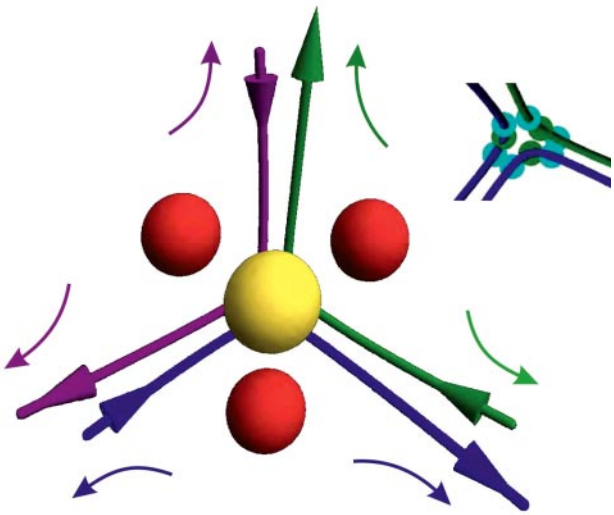

Figure 18. (Color online.) Intensity isosurfaces (spheres) and three hyperbola-like vortex lines for a pyramidal complex of four weakly bound fundamental solitons (a view from the side of the symmetry axis). Three solitons (off-axis) possess that same phase and the fourth (central) one is antiphase to them. Straight arrows on the lines show the direction of their orientation and curved arrows show the direction of the longitudinal component of the energy flux, which changes to the opposite one at supersingular points. Inset shows the central part of the vortex lines with supersingular points on them (dots).

where

$$F_\rho(\tau) = 2\,\mathrm{Im}\,(f^* g)\,, \quad F_\varphi(\tau) = |f|^2\,, \quad F_\tau(\tau) = \mathrm{Im}\left(f^*\frac{\mathrm{d}f}{\mathrm{d}\tau}\right). \tag{7.7}$$

According to (7.6), near the vortex line of the main component of the energy flux is the azimuthal component. The radial component possesses the smallest magnitude; as shown by calculations, $F_\rho(\tau) > 0$, according to which the vortex line in system (2.5) is an attractor. The longitudinal component of the energy flux is of primary interest to us. Calculations show that the function $F_\tau(\tau)$ can change its sign at some points of the vortex line. In the presence of such supersingular points of the vortex line, where $F_\tau(\tau) = 0$, the line will be referred to as sign changing, and in the absence of them as constant sign. Open vortex lines by necessity have an odd number of supersingular points (e.g., three in Fig. 18), whereas closed lines can be both constant sign and sign changing.

7.2 Bright topological solitons

Three-dimensional laser solitons are characterized, first, by the topology of their skeletons, i.e., the collection of all vortex lines. This is a general issue for both the conservative and dissipative varieties. Second, for laser (dissipative) solitons, the classification of the structure of energy fluxes is essential — a factor which is not manifested in conservative systems. Of the quantitative integral characteristics, besides the bright soliton energy $W(z) = \int I(\mathbf{r}_3, z)\,\mathrm{d}\mathbf{r}_3$, we will also use the tensor of inertia, calculated with respect to the center $\mathbf{R}_c(z)$ of the structure:

$$J_{ij}(z) = \int (r_i^2\delta_{ij} - r_i r_j)\, I(\mathbf{r}_3, z)\,\mathrm{d}\mathbf{r}_3\,. \tag{7.8}$$

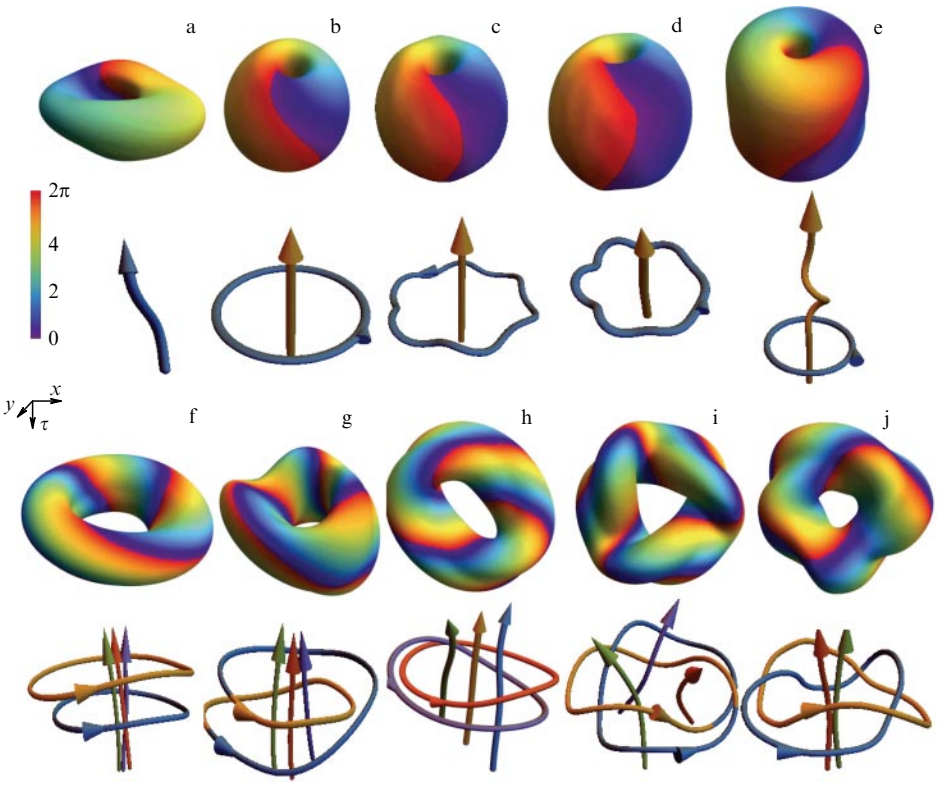

Figure 19. (Color online.) Laser solitons with various topologies. First and third rows are intensity isosurfaces at a level of $I/I_{\max} = 0.15$; second and fourth rows show skeletons for these solitons. (a) Precesson, $s = 0$, Cr = 0, Lk = 0. (b–e) Apple solitons, $s = 0$, Cr = 2, Lk = 1. (f) Double-ring soliton, $s = 0$, Cr = 8, Lk = 4. (g) 'Soliton with trivial knot+', $s = -1$, Cr = 9, Lk = 4. (h) Hopf+, $s = -2$, Cr = 10, Lk = 5. (i) Trefoil+, $s = -3$, Cr = 11, Lk = 4. (j) Solomon+, $s = -4$, Cr = 12, Lk = 6. The sign + emphasizes the difference from traditional structures with a similar name due to the presence of open vortex lines. Color scale indicates the value of the phase on the surfaces.

In Refs [56, 90–94], a wide class of bright (finite-energy) three-dimensional topological laser solitons is found and investigated, which is illustrated in Fig. 19. The presence of open (infinite) vortex lines in all of them in many cases complicates the direct application of known topological characteristics, e.g., the number of crossings in the projection of the skeleton on a plane, Cr, or the number of crossings with a sign for oriented lines, Lk (see [56]). Here, we accept the following approach: we specify a way of constructing the initial field distribution for obtaining a localized structure by stabilization after the transient process described by the master equation (2.2) and provide the established structures with the characteristics of this distribution, having made sure that the topology does not change in the transient process.

The algorithm for constructing an initial distribution for 'hula hoop' solitons, described in [91], is as follows. Initially, there is a two-dimensional soliton or a strongly coupled complex of such solitons, studied in sufficient detail [5]. The two-dimensional structure has a symmetry axis of the order N_{2D} and total topological charge m_{2D} (here, we consider only structures with the same sign of the charge). We place such a two-dimensional distribution of the envelope in a plane including the τ-axis, e.g., in the plane $y = 0$; in this case, the center of symmetry is located at distance ρ_2 from this axis, exceeding the dimensions of the two-dimensional structure. Let us rotate the two-dimensional distribution around the τ-axis, changing angle $\varphi = \arctan(y/x)$ from 0 to 2π, so that the two-dimensional center of symmetry describes a circle with radius ρ_2 centered on the τ-axis, simultaneously developing this distribution around the two-dimensional center of symmetry by angle $\theta(\varphi) = -s\varphi/N_{2D}$ with the integer twist index s in the initial plane rotated through an angle φ (with the current tangent to the circle serving as an instantaneous developing axis). As a result of such a procedure, the trajectories of dislocations of the two-dimensional structure in the $\mathbf{r}_3$-space are closed helical lines (circles on $s = 0$).

The thus formed three-dimensional field of the envelope is continuous. However, the structure will not be stable because of 'centrifugal forces' caused by the substantial angular momentum of the field with closed vortex lines having unit topological charges. To compensate for the angular momentum, let us introduce open vortex lines, arranged along the τ-axis. This is implemented by multiplying the above field distribution by $\exp(\mathrm{i}M_0\varphi)$ with an integer index M_0. Note that the formation of closed vortex lines gives rise to open lines, too, also oriented along the τ-axis. Therefore, the total number N_U of open vortex lines in a structure with the topological charge of each line $m = 1$ generally differs from $|M_0|$ and their total topological charge M also depends on N_C, the number of open vortex lines, with M coinciding with N_U:

$$M = N_U = M_0 + s\,\frac{N_C}{N_{2D}}\,. \tag{7.9}$$

The open lines are not linked to each other and by construction are oriented along the τ-axis.

Index M determines the total phase incursion per round-trip about open vortex lines in the (x, y)-plane: $\delta\Phi = 2\pi M$. Note that, due to the symmetry of the master equation (2.2) with respect to mirror reflection $x \to -x$ or $y \to -y$, topological solitons have mirror counterparts (without the

additional symmetry, the distributions of their field envelopes do not coincide). Hence, specifying the orientation of the closed lines relative to the open ones (the latter are unidirectional in the case considered) also essentially determines the soliton topology. If the directions of motion coincide, then the directions of rotation of a soliton and 'antisoliton' are opposite, and the character of stability is preserved. Specifying the initial parent two-dimensional soliton together with the number of open vortex lines N_U and the twist index s allows complete characterization of the skeleton topology of the three-dimensional field distribution. Calculations show that, to conserve the topological structure in the transient process, it is necessary to satisfy the condition $|M_0| \geqslant |M| > 0$.

In Refs [90, 91], tangle solitons with unit topological charge of all vortex lines were found. In this case, the above condition of soliton stability requires choosing a negative twist index, $s < 0$. For a stable laser soliton, the change of the sign of s without a change of signs of the topological charges of its vortex lines gives rise to another localized structure that cannot be reduced to the initial soliton by rotations. The change of the sign of s is equivalent to the reflection $\tau \to -\tau$ with a consequent change of the sign of the topological charges of the closed lines m_C, i.e., reversing their orientation to the opposite one. The new structure substantially differs from the initial one, and its stability requires additional investigation.

The parent two-dimensional structures for the solitons depicted in Fig. 19 are: a fundamental soliton, $m_{2D} = 0$, the only open vortex line with an absence of closed ones (Fig. 19a); a vortex soliton, $m_{2D} = 1$, $N_{2D} = \infty$, one open vortex line, surrounded by one closed line (Fig. 19b–e); a strongly coupled pair of vortex solitons with similar charges, $m_{2D} = 2$, $N_{2D} = 2$ (Fig. 19f–j). In this case, the twist index is $s = 0$ (Fig. 19a–f), $s = 1$ (Fig. 19g), $s = 2$ (Fig. 19h), $s = 3$ (Fig. 19i), and $s = 4$ (Fig. 19j).

We will determine the topological characteristics of the soliton skeletons — the collection of vortex lines — following the terminology of Ref. [95]. We introduce plane projections of these three-dimensional lines, depicting the intersections by a cross of two lines, a solid line located higher in the three-dimensional space, and a line with a gap located lower (see Fig. 23 in Section 7.3). The crossing index of oriented lines, located for definiteness in the (x, y)-plane, can be defined as $\varepsilon = \operatorname{sgn}\{\mathbf{t}_1 \times \mathbf{t}_2\}_\tau$. Here, $\mathbf{t}_{1,2}$ are tangents to the projections of the curves, the solid line chosen first in the vector product. The sum of crossing indices is the number of linkings of vortex lines Lk, which is a topological invariant, i.e., is preserved under smooth deformations of these lines. Another topological invariant, denoted by Cr, is the minimal number of crossings of the vortex lines of the skeleton projected on a plane upon changing this plane. The values of the invariants Lk and Cr are indicated in the Fig. 19 caption.

In Fig. 19, the bright laser solitons are arranged in order of growing topological complexity of their skeletons (we recall that a fundamental soliton without vortex lines is not a topological soliton). The simplest topological soliton possesses a single open vortex line, bent and precessing at some values of parameters, due to which we call it a precesson (Fig. 19a). In the apple solitons shown in Fig. 19b–e, a closed line is added embracing one open line. The open line is straight if the closed one possesses a rotational symmetry (Fig. 19b, c), and curved otherwise (Fig. 19d, e); the open line rotates in a helical fashion in the case of Fig. 19e.

A skeleton of the 'double-ring' soliton (Fig. 19f) consists of a bundle of three open vortex lines formed by splitting the topologically triply charged 'parent' straight vortex line and two closed nonlinking lines around them. The four remaining solitons shown in the bottom two rows (Fig. 19g–j) adopt the names common in topology for structures, consisting of only closed vortex lines; we add + to the traditional name to indicate the presence of open lines in the skeletons. In the case of Fig. 19g, it is a trivial knot with three open lines (upon extracting them, the only closed line can be transformed into a circle by smooth deformations). In Fig. 19h, there are two singly linked closed vortex lines (a Hopf link) belting three open lines. The closed line in Fig. 19i is a knot (trefoil), inside which there are three open lines. Finally, Fig. 19j illustrates a knot, or more exactly a Solomon link, in which two closed vortex lines are doubly linked; two open vortex lines are additionally present.

Another factor, important for classification and specific to dissipative solitons, is related to the structure of energy fluxes — the field of the Poynting vector $\mathbf{S}_3$. Note that the wavefront of many conservative solitons, e.g., in a medium with saturable Kerr nonlinearity [96], is a plane, so that we can assume $\nabla\Phi_3 = 0$ and $\mathbf{S}_3 = 0$; therefore, for such solitons, energy fluxes are absent. For dissipative solitons, the divergence of the energy flux serves as a local characteristic of the vector field $\mathbf{S}_3$: depending on whether the energy predominantly inflows or outflows from an elementary volume through its boundaries, $\nabla_3\mathbf{S}_3 < 0$ (the first case: energy sink) or $\nabla_3\mathbf{S}_3 > 0$ (the second case: energy source). Generally, the energy sinks and sources should be defined with explicit consideration of the dissipative factors in Eqn (2.3), but calculations show only a weak influence of these factors due to the smallness of the diffusion coefficients and approximate dynamic balance between the gain and absorption.

In addition, also of importance is the number of supersingular points on the vortex lines, at which the sign of S_τ — the longitudinal (along the vortex line) component of the energy flux — changes. The number of such points on open vortex lines must be odd, since at the periphery the energy flux is directed off the soliton center, and on closed lines in must be even.

In Fig. 20, we show the supersingular points for a number of solitons, presented in Fig. 19. As is seen from Fig. 20b–e, although for all four types of apple solitons the topology is similar, they differ from each other by the number of supersingular points on the closed and open vortex lines. Note also that, among stable laser solitons, there are 'rigid' (with intensity and energy flux distributions unchanged in the course of propagation up to a translation or rotation as a whole) and 'deformable' solitons with distributions of intensity and energy flows quasiperiodically oscillating in the course of propagation.

Apple solitons of various types exist in different domains of the parameter space, partially overlapping. We choose the linear gain coefficient g_0 as the main variable parameter. From Fig. 21a, one can see the ranges of existence and stability of various apple solitons. The overlapping of these domains for the asymmetric stationary 'rigid' and oscillating deformable solitons, in principle, allows speaking about the possibility of recording information, protected from perturbations not only by topological characteristics, but also by an energy characteristic — the number of supersingular points on the vortex lines.

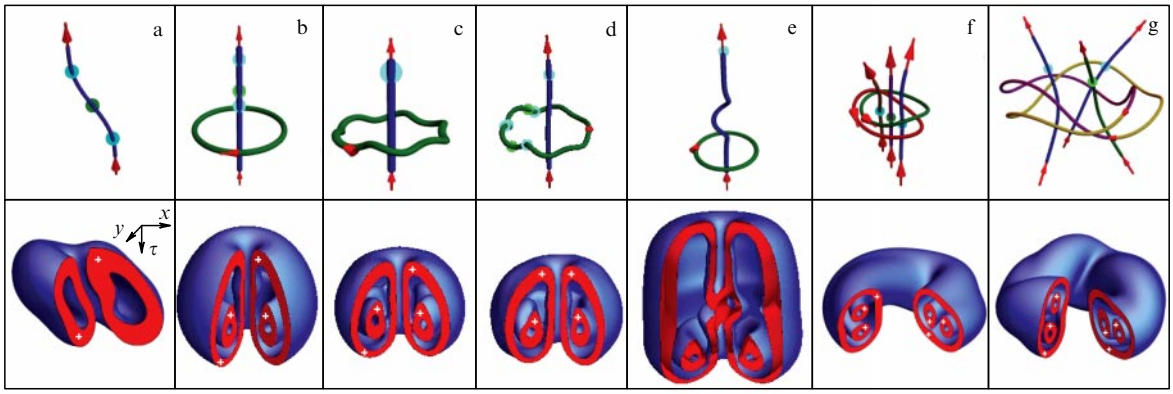

Figure 20. (Color online.) Laser solitons with various structures of energy fluxes and topologies. (a) Precesson. (b–e) Apple solitons. (f) Hopf+ soliton. (g) Trefoil+. Upper row: vortex lines with supersingular points (circles). Lower row: divergence of radiation energy flux $\mathbf{S}_3$: regions with a + sign ($\operatorname{div}\mathbf{S}_3 > 0$, red color) correspond to sources of radiation; those with a minus (−) sign ($\operatorname{div}\mathbf{S}_3 < 0$, blue color) correspond to energy sinks.

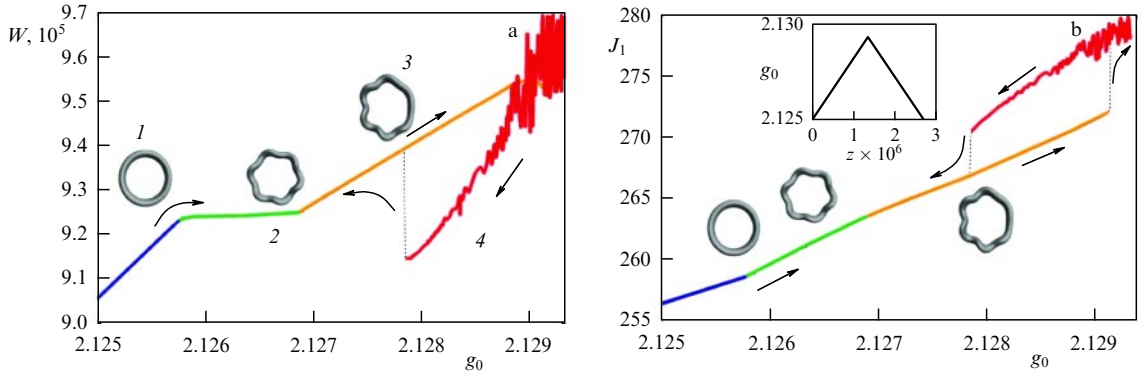

Figure 21. (Color online.) Stability ranges of apple solitons of various types and the hysteresis change in soliton energy (a) and the minimal eigenvalue of the inertia tensor (b) upon a slow longitudinal increase and decrease (arrows) in the linear gain coefficient (shown in the inset). In Fig. a, segment *1* corresponds to the regime of a symmetric apple, *2* to an apple with azimuthal modulation of the closed vortex line, *3* to an asymmetric apple, *4* to an asymmetric oscillating apple.

7.3 Hysteresis phenomena

The above conservation of topological and energy characteristics (information) is possible only under certain limitations of the variation of parameters. Let the linear gain coefficient g_0 at first smoothly grow with an increase in propagation length z, crossing the boundary of stability of the initial type of soliton, and then smoothly return to the initial value (see the inset in Fig. 21b). As is seen from Fig. 21, a reversible hysteresis takes place for asymmetric 'rigid' and oscillating solitons: after the recovery of the parameters, the number of supersingular points is also restored (provided that the topological characteristics do not change). Such a hysteresis may be related to a first-order phase transition, i.e., a hard excitation, or subcritical bifurcation. At the same time, transitions between an ideal symmetric apple and asymmetric apples of two types, upon which not only the topology but also the number of supersingular points are preserved, can be associated with phase transitions of the second order, or supercritical bifurcations.

As is seen from Fig. 22, the stability domains of the solitons discussed are overlapping. Therefore, upon changing the linear gain coefficient with the crossing of stability domain boundaries, a change in the soliton topology is inevitable. Simulations show that the laser soliton topology changes via topological reactions of two types (Fig. 23). The first (Fig. 23a–d) is the approaching and touching of two vortex lines, followed by the switching of their branches. At the touching point, the tangents to the lines corresponding to their orientation are oppositely directed. Such a reaction can proceed in both directions. The second type includes reactions (Fig. 23e–g) comprising a strong bending of a vortex line followed by the separation of a closed vortex line from it and, possibly, a sequential separation of several such loops.

Upon a slow change in the gain coefficient, similar to that shown in the inset to Fig. 21b, the cascade of the above topological reactions occurs comparatively quickly (see Ref. [56] for details), the result being illustrated in Fig. 24a. Here, the initial structure was a trefoil+ soliton, which, upon a slow increase in the gain coefficient, transformed first into a Hopf+ soliton, and then after short-term intermediate topological reactions, into an apple soliton, stable in the widest domain of parameters. Upon a slow increase in the gain coefficient, the soliton conserves its apple form. Thus, an irreversible hysteresis of the soliton takes place here. In this case, for one value of the gain coefficient, the energy of the final apple soliton is considerably smaller than that of the initial topologically more complex trefoil+.

Figure 24b shows the change in the topological invariant Cr (minimal number of crossings) with an increase and decrease in the gain coefficient. If the initial structure is a

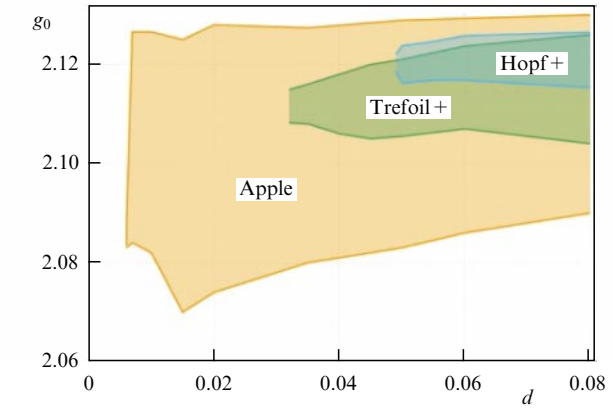

Figure 22. (Color online.) Domains of stability for solitons: apple (symmetric), trefoil+, and Hopf+ in the plane of parameters 'diffusion coefficient d–linear gain coefficient g_0.'

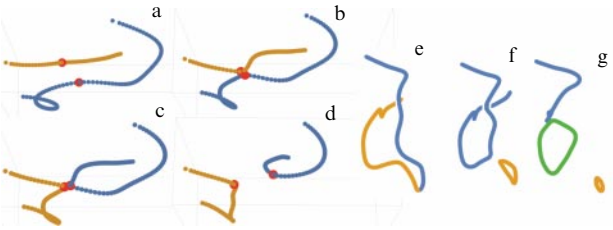

Figure 23. (Color online.) Two types of elementary topological reactions with vortex lines of dissipative structures: opposite direction reconnection (a–d) and separation of a closed vortex line from the parent one (e–g).

stable trefoil+, then, upon a decrease in the gain coefficient, it vanishes with the establishment of a nonlasing regime in the entire system. In the case of an increasing gain coefficient, the trefoil+ turns into a Hopf+ soliton. Furthermore, if the gain coefficient decreases, then, as in the previous case, the nonlasing regime is established, whereas, upon an increase in the gain coefficient, a transition to the apple soliton occurs. The latter vanishes with the establishment of the nonlasing regime upon both increasing and decreasing the gain coefficient. Note that, with all topological transformations, the topological structure is simplified — the topological invariant Cr decreases. Moreover, Fig. 24b shows within what limits the topological invariants are preserved — these limits coincide with those of the corresponding soliton stability.

7.4 Tubular solitons

In this section, we consider bright solitons (with a finite power of radiation), which are intermediate between two-dimensional and three-dimensional ones. In the case adjacent to the two-dimensional geometry, this problem can be considered to be beyond the mean field approximation due to the longitudinal variation in the field envelope taken into account. In the opposite limit, the transition to the model of an unlimited nonlinear medium is implemented, e.g., in ring resonators of sufficiently large length.

For scalar solitons, following [77], we proceed from the master equation (2.2). Consider first a symmetric distribution with a straight vortex line (compare with Eqn (5.8)):

$$E(\mathbf{r}_3, z) = A_{|m|}(r)\exp\left(-\mathrm{i}q_{|m|}z + \mathrm{i}m\varphi\right). \tag{7.10}$$

Here, the envelope is independent of the variable τ, and for the rest of the variables we use a cylindrical system of coordinates (r, φ, z) with $r = \sqrt{x^2 + y^2}$; as before, m is the integer topological charge. Substituting (7.10) into (2.2), we arrive at the equation coinciding with that for symmetric two-dimensional solitons (5.9) with q replaced with ν. However, the stability of a two-dimensional structure does not imply the stability of the corresponding three-dimensional one, since, in the latter case, the stability with respect to perturbations modulated in the additional coordinate τ is also of importance. Moreover, such structures appear to be unstable with respect to small perturbations [77].

Indeed, although solutions of the form (7.10) with $m = 1$ exist, they appear to be unstable because of bending and fragmentation of the straight vortex line. Nevertheless, stabilization of the vortex line becomes possible upon proceeding from an unlimited medium to a ring resonator of finite length L, which is implemented, for example, in a fiber laser. The stabilizing role of the finite length is due to the fact that it restricts manifold of possible 'dangerous' perturbations, serving as a filter.

The dynamics of a system with finite resonator length L is described by the master equation in the fixed (laboratory) coordinate frame (in which the frequency dispersion is taken into account by the term with $\partial^2 E/\partial z^2$, since, in the lowest-

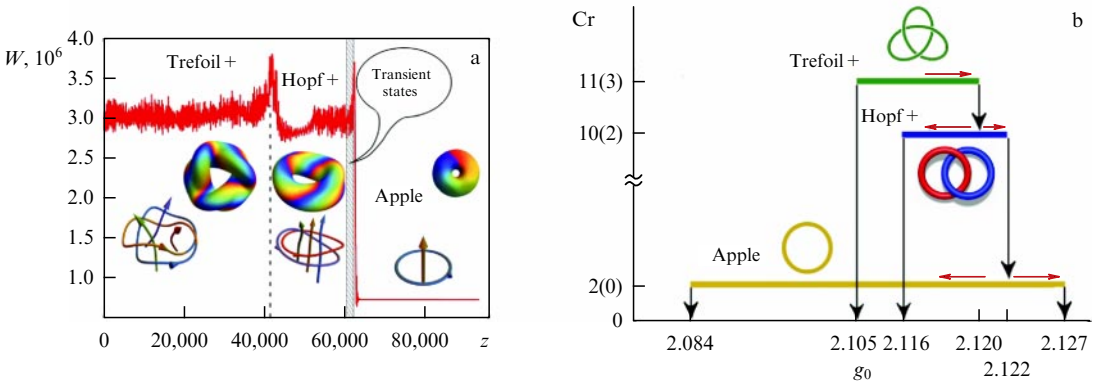

Figure 24. (Color online.) (a) Soliton energy variation with the growth of the linear gain coefficient with sequential jump-like transformation of the trefoil+ soliton into a Hopf+ one and then into an apple soliton, which is conserved upon a decrease in the gain coefficient. Insets show intensity isosurfaces and complete skeletons of the solitons. (b) Dependence of the minimal number of self-crossings on the gain coefficient. On the Cr scale, numbers on the left indicate the number of crossings of all vortex lines, and the number on the right (in parentheses), only of the closed ones. Horizontal arrows directed to the right correspond to an increase in the gain coefficient and, to the left, to its decrease. Insets show closed vortex lines.

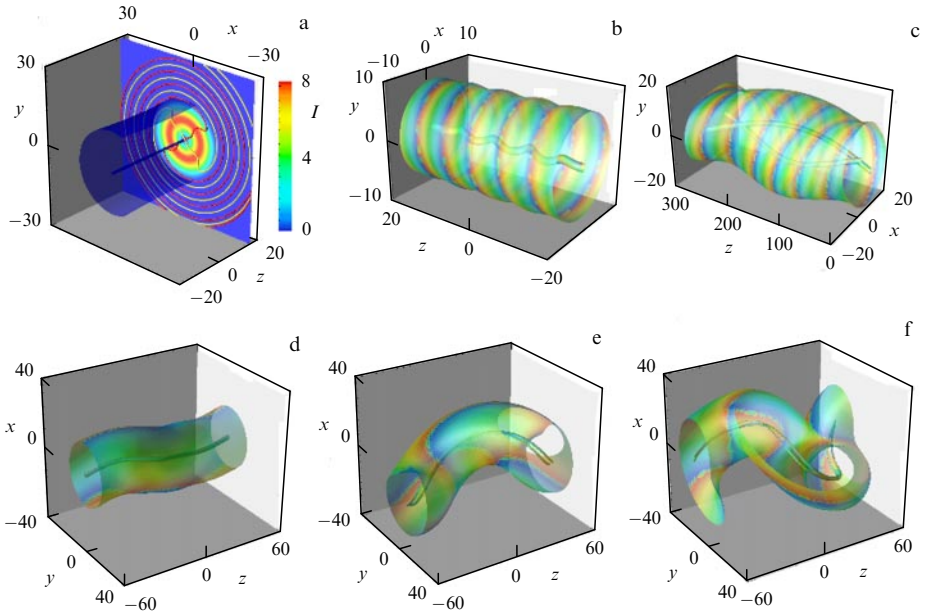

Figure 25. (Color online.) Intensity isosurfaces for tubular solitons with topological charge $m = 1$ (a) and $m = 2$ (b–f) in a resonator with length $L = 36$ (a), 42 (b), 300 (c), and 110 (d–f).

order approximation, it follows from the transfer equation that $\partial^2 E/\partial t^2 = v_g^2(\partial^2 E/\partial z^2)$ and the condition of periodicity in z:

$$\frac{\partial E}{\partial t} + \frac{\partial E}{\partial z} - (\mathrm{i} + d_\perp)\Delta_\perp E - (\mathrm{i} + d_\parallel) D_2 \frac{\partial^2 E}{\partial t^2} = f\left(|E|^2\right) E\,, \tag{7.11}$$

$$E(x, y, z + L, t) = E(x, y, z, t)\,. \tag{7.12}$$

Calculations [77] have shown the presence of a critical length of resonator L_{cr}, depending on the topological charge m. Tubular structures with a straight vortex line are stable in resonators with subcritical length $L < L_{\mathrm{cr}}$ (Fig. 25a). Upon exceeding the critical length, the vortex line bends (Fig. 25b, d). Lines with the charge $|m| > 1$ at somewhat greater resonator lengths split into $|m|$ lines with a unit charge (Fig. 25c, e, f). At even greater lengths L, fragmentation of the vortex lines and the formation of three-dimensional solitons (for the parameters lying within the stability domain) or field damping occur.

The analysis of polarization features of tubular solitons with the effects of weak nonparaxiality taken into account reduces to that carried out in Section 5.3 for symmetric structures with a straight vortex line [77]. As we have seen, such paraxial solitons are stable in resonators with a subcritical length. In this case, the polarization structure in arbitrary transverse sections of a tubular soliton is constant and coincides with that for a two-dimensional laser soliton (see Fig. 12).

8. Dark topological solitons

In Section 7, we considered bright optical solitons in scenarios with various geometrical dimensions, whose field rapidly decreases at the periphery, ensuring the finiteness of the soliton energy. At the same time, it is reasonable to consider dark solitons with a nonzero and uniform level of intensity at the periphery and a localized intensity dip in the central part of the soliton. Although the energy of 'ideal' dark solitons is infinitely large, which cannot be implemented experimentally, such models adequately describe the central region of solitons, weakly sensitive to the behavior of the field in the remote peripheral region. Hence, dark solitons, as well as in the case of conservative schemes [1], are experimentally available. Moreover, they can have advantages over bright ones, including a wider domain of stability in the parameter space.

Dark laser solitons exist in schemes with various dimensions, but here we will restrict ourselves to analyzing three-dimensional schemes that allow structures with the most diverse topology. For tubular dark solitons, the analysis is close to that presented in Section 7.4. A specific feature of dark solitons that distinguishes them from bright ones is the peripheral boundary conditions. Note the high sensitivity of the results to these conditions. To reduce this sensitivity, in the numerical calculations in [97] presented below, the authors used 'transparent boundary conditions' with minimization of fictitious reflection from the edge of the computation domain by choosing the transverse profile of radiation losses in the peripheral region.

The master equation (2.2) serves as the starting point again. For a symmetric distribution with a straight vortex line, the field has the form (7.10), but with different asymptotic behavior at the periphery:

$$\frac{\mathrm{d}\left|A_m(r)\right|^2}{\mathrm{d}r} \to 0 \quad \text{at} \quad r \to \infty\,. \tag{8.1}$$

For the radial function $A_m(r)$, we get an equation that coincides with the equation of symmetric two-dimensional solitons (5.9), with q replaced by v. However, as in the case of bright tubular solitons (see Section 7.4), the stability of a two-dimensional structure does not imply the stability of the corresponding three-dimensional structure, because, in the latter case, stability against perturbations, modulated in the additional coordinate τ, is also of importance.

Solutions of the form (8.1) with $m = 1$ are also unstable because of bends and the fragmentation of the straight vortex line. The vortex line stabilization again becomes possible with a transition from an unlimited medium to a ring resonator

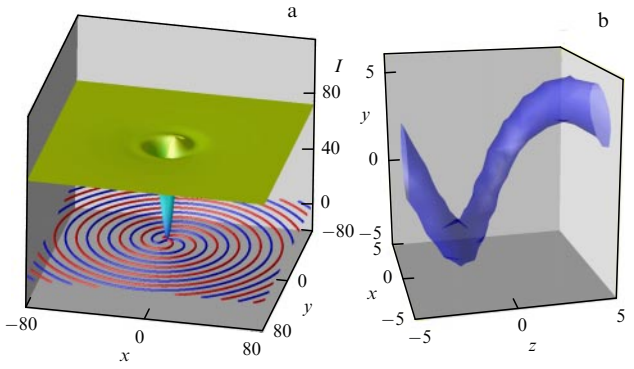

Figure 26. (Color online.) (a) Intensity distribution for a dark soliton with topological charge $m = 1$ at $z = L/2$ and lines $\mathrm{Re}\, E = 0$ and $\mathrm{Im}\, E = 0$ (below). (b) Vortex line, shown by the intensity isosurface at a level of $I/I_{\max} = 0.06$ at $z = L/2$; $g_0 = 2.15$, $d = 0.05$, $L = 10$.

with finite length L, which is implemented, for instance, in a fiber laser. We describe the dynamics of such a scheme with the master equation (7.11) and z-periodicity condition (7.12). A symmetric dark soliton with the charge $m = 1$ serves as an initial condition.

In contrast to bright solitons, a dark soliton breaks down with time at small resonator lengths, $L < L_{\min}$ (with the parameters chosen, $L_{\min} \approx 5$): its center in the transverse plane begins to move along a spiral and ultimately goes to the periphery. As a result, a regime of homogeneous lasing is established inside the entire resonator. Furthermore, for lengths L exceeding the critical value $L_{\max}$ ($L_{\max} \sim 20$), the initially single vortex line is fragmented, as in an unlimited medium, in the way pointed out above. Therefore, we will consider only those schemes with medium resonator lengths $L_{\min} < L < L_{\max}$. Here, it is necessary to distinguish between two ways of stabilizing the vortex line.

First, a vortex line can simply bend, which leads to stable asymmetric distribution of the field (Fig. 26). Even more stable and at the same time existing in a wider range of resonator lengths are structures in which the vortex lines are segments of a 'double helix' with similar topological charges, determined by the modified initial condition (Fig. 27). Depending on the length L, the helices make one ($L \approx 12$) or two ($L \approx 25$) turns. At small deviations from these lengths, the helices retain stability, but lose the helical symmetry. Structures with two helical vortex lines are also rigid.

Second, an interesting scenario for stabilizing a straight vortex line of a dark soliton is realized at smaller values of the linear gain coefficient g_0. In this case, the structure preserves the symmetry, but an additional closed (circular) vortex line arises (Fig. 28). The circular line moves with considerable velocity along the straight vortex line without loss of symmetry. Such a structure preserves the stability even at relatively large lengths of the resonator. Note that a kindred structure is presented in Ref. [13] for a different scheme — an optical parametric oscillator in an unlimited medium with quadratic nonlinearity.

As we have seen, the longitudinal limitations of a real scheme allow the formation of stable topological (vortex) dark solitons. The domain of their stability is rather large; it practically coincides with the domain of classical bistability of plane wave regimes. The natural question of the effect of the scheme's transverse limitations on topological localized structures is discussed in Section 10.

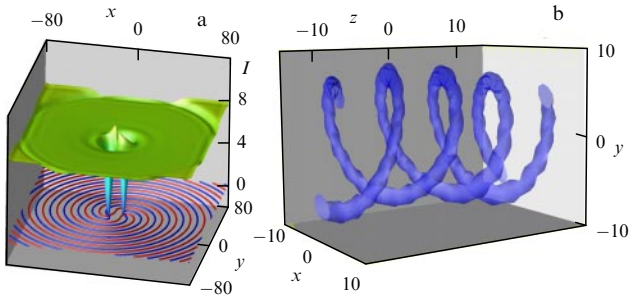

Figure 27. (Color online.) (a) Intensity distribution for a dark soliton with total topological charge $m = 2$ at $z = L/2$ and lines $\mathrm{Re}\, E = 0$ and $\mathrm{Im}\, E = 0$ (below). (b) Double vortex line (intensity isosurface at the level of $I/I_{\max} = 0.06$); $g_0 = 2.15$, $d = 0.05$, $L = 25.6$.

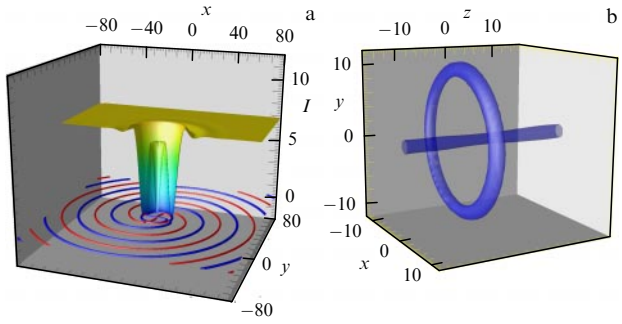

Figure 28. (Color online.) (a) Intensity distribution in the transverse section in the plane of a circular vortex line and lines $\mathrm{Re}\, E = 0$, $\mathrm{Im}\, E = 0$ (below) for a dark soliton. (b) Intensity isosurfaces at the level $I/I_{\max} = 0.06$, demonstrating vortex lines; $g_0 = 2.117$, $d = 0.045$, $L = 30$.

9. Quantum fluctuations

Quantum fluctuations of the field of laser solitons and the medium in which they propagate are of interest not only from a general scientific point of view but also from a practical one, since these fluctuations restrict the ultimate capabilities of soliton applications to informatics. For conservative temporal solitons, squeezed states are theoretically predicted and experimentally implemented, which correspond to solitons with a noise level below that of a common coherent state [98–100]. Similar studies of quantum fluctuations in spatial conservative solitons were carried out in Refs [101–103].

For dissipative optical solitons, the quantum effects are studied in less detail. Results on generating squeezed radiation from such solitons in the parametric oscillator scheme are summarized in monograph [104]. In Refs [105–107] (see also [5]), for spatial solitons in a wide-aperture passive nonlinear interferometer with coherent holding radiation, a quantum Langevin equation is derived. The solution of this equation in the approximation of weak fluctuations (linearized approach) allowed finding a statistical variance of fluctuations of the mean position and momentum of solitons and the conditions for implementing squeezed states.

However, at present, studies of quantum fluctuations of the laser solitons, especially topological laser solitons, are just beginning. Although in this case the approach is largely similar to the theory of solitons in a nonlinear interferometer, the laser case has its own essential specificity. First, for lasers with saturable absorption, it is important to take into account fluctuations of the active and passive media provid-

ing the resonance nonlinearity (in the case of an interferometer, the nonlinearity is Kerr-type and nonresonant). Further, for topological laser solitons, the angular selectivity of losses in the scheme is important, in the absence of which the domain of stability for these solitons in the parameter space collapses into a point [5].

In this section, we will first present a master equation to describe fluctuations in two-dimensional laser solitons [108]. In the case of a fast medium response, this equation generalizes the classical equation (5.1) by introducing a stochastic Langevin force in it. A scheme of a wide-aperture laser with saturable absorption and external holding radiation is considered (see Section 6 for the classical analog). At zero intensity of the holding radiation, this scheme reduces in essence to a laser one, and — upon replacing the medium material equations — to the scheme of a nonlinear interferometer with holding radiation. By analogy with the case of a nonlinear interferometer, the linearization approach is then developed [109]. Then, following Ref. [110], we will present some results of solving the complete quantum Langevin equation numerically. We restrict ourselves here to the scheme of a wide-aperture ring laser with saturable absorption using the above mean-field approximation (envelope averaging in the longitudinal direction).

9.1 Laser Heisenberg–Langevin equations

The master equations are derived as follows [108]. The total Hamiltonian of the system consists of the Hamiltonian $\hat{H}_{\text{field}}$ of the field in the matrix without the active, with laser gain (index g), and passive, with saturable absorption (index a), centers, the Hamiltonians of these centers $\hat{H}^{\text{g}}$ and $\hat{H}^{\text{a}}$, and the Hamiltonians of the field and center interaction $\hat{V}^{\text{g}}$ and $\hat{V}^{\text{a}}$ (dipole approximation). Additionally allowed for are nonresonant losses and dispersion in the matrix, the pump, and the relaxation processes, giving rise to Langevin stochastic sources in the master equations. For the field, the Hamiltonian is constructed from the classical one by replacing the envelope E with the annihilation operator $\hat{a}$ and E^* with the creation operator $\hat{a}^\dagger$:

$$\hat{H}_{\text{field}} = \frac{\hbar\omega_0}{2}\int\left[\hat{a}^\dagger(\mathbf{r}_\perp,t)\hat{a}(\mathbf{r}_\perp,t) + \hat{a}(\mathbf{r}_\perp,t)\hat{a}^\dagger(\mathbf{r}_\perp,t)\right]\mathrm{d}\mathbf{r}_\perp \quad (9.1)$$

($\hbar$ being the reduced Planck constant). The centers, as above, are modeled by two-level systems with the transition frequency ω_{c}, detuned from the carrier frequency ω_0 by $\delta\omega$. The energy levels are denoted by W_1 and W_2 ($W_2 - W_1 = \hbar\omega_{\text{c}}$). Then,

$$\begin{aligned}\hat{H}^{\text{g}} &= \int\left[W_1\hat{\sigma}_1(\mathbf{r}_\perp,t) + W_2\hat{\sigma}_2(\mathbf{r}_\perp,t)\right]\mathrm{d}\mathbf{r}_\perp\,,\\ \hat{H}^{\text{a}} &= \int\left[W_1\hat{\pi}_1(\mathbf{r}_\perp,t) + W_2\hat{\pi}_2(\mathbf{r}_\perp,t)\right]\mathrm{d}\mathbf{r}_\perp\,.\end{aligned} \quad (9.2)$$

The operators $\hat{\sigma}_{1,2}$ and $\hat{\pi}_{1,2}$ have the meaning of the number of atoms at the corresponding level within a unit area of the aperture. Finally, the Hamiltonians of interaction of the field with the centers are

$$\begin{aligned}\hat{V}^{\text{g}} &= \hbar g_{\text{g}}\int\left[\hat{\sigma}(\mathbf{r}_\perp,t)\hat{a}^\dagger(\mathbf{r}_\perp,t) + \hat{\sigma}^\dagger(\mathbf{r}_\perp,t)\hat{a}(\mathbf{r}_\perp,t)\right]\mathrm{d}\mathbf{r}_\perp\,,\\ \hat{V}^{\text{a}} &= \hbar g_{\text{a}}\int\left[\hat{\pi}(\mathbf{r}_\perp,t)\hat{a}^\dagger(\mathbf{r}_\perp,t) + \hat{\pi}^\dagger(\mathbf{r}_\perp,t)\hat{a}(\mathbf{r}_\perp,t)\right]\mathrm{d}\mathbf{r}_\perp\,.\end{aligned} \quad (9.3)$$

In (9.3), the constants of interaction between the field and the centers in the dipole approximation are expressed as $g_{\text{g,a}} = \mu_{\text{g,a}}[\omega_0/(2\varepsilon_0\hbar L)]^{1/2}$, $\mu_{\text{g,a}}$ are the matrix elements of the dipole transition between the working levels of the centers, ε_0 is the dielectric constant of the matrix at the carrier frequency, and L is the resonator length. The operators $\hat{\sigma}$ and $\hat{\pi}$ of collective coherence of active and passive centers are also introduced [108]. The operators obey the following commutation relations:

$$\left[\hat{a}(\mathbf{r}_\perp,t),\hat{a}^\dagger(\mathbf{r}'_\perp,t)\right] = \left(1 - \frac{1-\mathrm{i}d}{2k_0^2}\,\Delta_\perp\right)\delta(\mathbf{r}_\perp - \mathbf{r}'_\perp)\,, \quad (9.4)$$

$$\begin{aligned}\left[\hat{\sigma}(\mathbf{r}_\perp,t),\hat{\sigma}^\dagger(\mathbf{r}'_\perp,t)\right] &= \left[\hat{\sigma}_1(\mathbf{r}_\perp,t) - \hat{\sigma}_2(\mathbf{r}_\perp,t)\right]\delta(\mathbf{r}_\perp - \mathbf{r}'_\perp)\,,\\ \left[\hat{\sigma}_1(\mathbf{r}_\perp,t),\hat{\sigma}(\mathbf{r}'_\perp,t)\right] &= \hat{\sigma}(\mathbf{r}_\perp,t)\delta(\mathbf{r}_\perp - \mathbf{r}'_\perp)\,,\\ \left[\hat{\sigma}_2(\mathbf{r}_\perp,t),\hat{\sigma}(\mathbf{r}'_\perp,t)\right] &= -\hat{\sigma}(\mathbf{r}_\perp,t)\delta(\mathbf{r}_\perp - \mathbf{r}'_\perp)\,,\end{aligned} \quad (9.5)$$

$$\begin{aligned}\left[\hat{\pi}(\mathbf{r}_\perp,t),\hat{\pi}^\dagger(\mathbf{r}'_\perp,t)\right] &= \left[\hat{\pi}_1(\mathbf{r}_\perp,t) - \hat{\pi}_2(\mathbf{r}_\perp,t)\right]\delta(\mathbf{r}_\perp - \mathbf{r}'_\perp)\,,\\ \left[\hat{\pi}_1(\mathbf{r}_\perp,t),\hat{\pi}(\mathbf{r}'_\perp,t)\right] &= \hat{\pi}(\mathbf{r}_\perp,t)\delta(\mathbf{r}_\perp - \mathbf{r}'_\perp)\,,\\ \left[\hat{\pi}_2(\mathbf{r}_\perp,t),\hat{\pi}(\mathbf{r}'_\perp,t)\right] &= -\hat{\pi}(\mathbf{r}_\perp,t)\delta(\mathbf{r}_\perp - \mathbf{r}'_\perp)\,.\end{aligned} \quad (9.6)$$

The effective diffusion coefficient is again considered small, $0 < d \ll 1$.

The relaxation of the centers and incoherent broadband pump are taken into account by introducing the decay rates of the coherence (Γ and γ) and populations ($\Gamma_{1,2}$ and $\gamma_{1,2}$) of the working levels of the active and passive centers, as well as the mean rates of populating the upper level of active centers R_{g} and the lower level of passive centers R_{a}. We assume that both levels of the active and passive centers decay with the rates $\Gamma_{1,2}$ and $\gamma_{1,2}$ to certain levels, different from the working ones. For simplicity, we set $\Gamma = (\Gamma_1 + \Gamma_2)/2$, $\gamma = (\gamma_1 + \gamma_2)/2$, which is precisely valid in rarified atomic gases. We denote by κ the rate of the field decrease in the resonator upon axial propagation of the wave. Then, the Heisenberg–Langevin master equations are formulated as follows:

$$\frac{\partial\hat{a}}{\partial t} = (\mathrm{i}+d)\,\frac{v_{\text{g}}}{2k_0}\,\Delta_\perp\hat{a} - \frac{\kappa}{2}\,\hat{a} + g_{\text{g}}\hat{\sigma} + g_{\text{a}}\hat{\pi} + \hat{F}_{\text{a}}\,, \quad (9.7)$$

$$\begin{aligned}\frac{\partial\hat{\sigma}}{\partial t} &= -(\Gamma - \mathrm{i}\delta\omega)\hat{\sigma} + g_{\text{g}}(\hat{\sigma}_2 - \hat{\sigma}_1)\hat{a} + \hat{F}\,,\\ \frac{\partial\hat{\sigma}_1}{\partial t} &= -\Gamma_1\hat{\sigma}_1 + g_{\text{g}}(\hat{\sigma}^\dagger\hat{a} + \hat{\sigma}\hat{a}^\dagger) + \hat{F}_1\,,\\ \frac{\partial\hat{\sigma}_2}{\partial t} &= R_{\text{g}} - \Gamma_2\hat{\sigma}_2 - g_{\text{g}}(\hat{\sigma}^\dagger\hat{a} + \hat{a}^\dagger\hat{\sigma}) + \hat{F}_2\,,\end{aligned} \quad (9.8)$$

$$\begin{aligned}\frac{\partial\hat{\pi}}{\partial t} &= -(\gamma - \mathrm{i}\delta\omega)\hat{\pi} + g_{\text{a}}(\hat{\pi}_2 - \hat{\pi}_1)\hat{a} + \hat{G}\,,\\ \frac{\partial\hat{\pi}_1}{\partial t} &= R_{\text{a}} - \gamma_1\hat{\pi}_1 + g_{\text{a}}(\hat{\pi}^\dagger\hat{a} + \hat{a}^\dagger\hat{\pi}) + \hat{G}_1\,,\\ \frac{\partial\hat{\pi}_2}{\partial t} &= -\gamma_2\hat{\pi}_2 - g_{\text{a}}(\hat{\pi}^\dagger\hat{a} + \hat{\pi}\hat{a}^\dagger) + \hat{G}_2\,.\end{aligned} \quad (9.9)$$

The correlation relations for the Langevin sources $\hat{F}$ and $\hat{G}$ follow from the fluctuation-dissipation theorem using the results of Ref. [111]. Let us write the nonzero correlators in angle brackets:

$$\begin{aligned}\left\langle\hat{F}_i^\dagger(\mathbf{r}_\perp,t)\hat{F}_j(\mathbf{r}'_\perp,t')\right\rangle &= \left\langle\hat{F}_i^\dagger\hat{F}_j\right\rangle\delta(t-t')\delta(\mathbf{r}_\perp - \mathbf{r}'_\perp)\,,\\ \left\langle\hat{F}_i(\mathbf{r}_\perp,t)\hat{F}_j(\mathbf{r}'_\perp,t')\right\rangle &= \left\langle\hat{F}_i\hat{F}_j\right\rangle\delta(t-t')\delta(\mathbf{r}_\perp - \mathbf{r}'_\perp)\,,\quad i,j = 1,2\,,\end{aligned}$$

$$\langle \hat{F}_2\hat{F}_2\rangle = \Gamma_2\bar{\sigma}_2 + R_{\rm g}(1-s_{\rm g})\,,\quad \langle \hat{F}^\dagger\hat{F}\rangle = \Gamma_1\bar{\sigma}_2 + R_{\rm g}\,,$$
$$\langle \hat{F}_1\hat{F}_1\rangle = \Gamma_1\bar{\sigma}_1\,,\quad \langle \hat{F}_1\hat{F}\rangle = \Gamma_1\bar{\sigma}\,,$$
$$\langle \hat{F}\hat{F}_2\rangle = \Gamma_2\bar{\sigma}\,,\quad \langle \hat{F}\hat{F}^\dagger\rangle = \Gamma_2\bar{\sigma}_1\,. \tag{9.10}$$

In (9.10), in addition to the mean pump rate $R_{\rm g}$, the parameter of its regularity degree $s_{\rm g}$ is introduced, $0 < s_{\rm g} < 1$. At $s_{\rm g} = 0$ the centers are excited and transit to the upper working level independent of each other and randomly in time (Poisson pumping), and at $s_{\rm g} = 1$ the pump is strictly regular and free of noises (sub-Poisson pumping). When introducing a similar parameter $s_{\rm a}$ for the pumping of the lower level of passive centers, we get the following expressions for the correlators:

$$\langle \hat{G}_i^\dagger(\mathbf{r}_\perp,t)\hat{G}_j(\mathbf{r}'_\perp,t')\rangle = \langle \hat{G}_i^\dagger\hat{G}_j\rangle\delta(t-t')\delta(\mathbf{r}_\perp-\mathbf{r}'_\perp)\,,$$
$$\langle \hat{G}_i(\mathbf{r}_\perp,t)\hat{G}_j(\mathbf{r}'_\perp,t')\rangle = \langle \hat{G}_i\hat{G}_j\rangle\delta(t-t')\delta(\mathbf{r}_\perp-\mathbf{r}'_\perp)\,,\quad i,j=1,2,$$
$$\langle \hat{G}_1\hat{G}_1\rangle = \gamma_1\bar{\pi}_1 + R_{\rm a}(1-s_{\rm a})\,,\quad \langle \hat{G}\hat{G}^\dagger\rangle = \gamma_2\bar{\pi}_1 + R_{\rm a}\,, \tag{9.11}$$
$$\langle \hat{G}^\dagger\hat{G}\rangle = \gamma_1\bar{\pi}_2\,,\quad \langle \hat{G}_2\hat{G}_2\rangle = \gamma_2\bar{\pi}_2\,,$$
$$\langle \hat{G}\hat{G}_2\rangle = \gamma_2\bar{\pi}\,,\quad \langle \hat{G}_1\hat{G}\rangle = \gamma_1\bar{\pi}\,.$$

The presented operator equations completely describe the laser system considered, but they are not very convenient for analysis and calculations because of the noncommutativity of the operators. Therefore, in quantum electrodynamics [112] and quantum optics [41], the c-number representation is widely used, in which the operators are replaced with c-number functions. Such a procedure is justified for the calculation of quantum mean values of an operator that consists of a sum of normal products of creation and annihilation operators (creation operators are left of annihilation ones, the order of commuting operators is, naturally, unimportant). Operators can always be reduced to the normal form using the commutation relations. In application to Eqns (9.7)–(9.9), the normal product of operators has the form $\hat{a}^\dagger\hat{\sigma}^\dagger\hat{\pi}^\dagger\hat{\sigma}_2\hat{\pi}_2\hat{\sigma}_1\hat{\pi}_1\hat{\pi}\hat{\sigma}\hat{a}$ [41]. Finally, it is required that the expressions for the Langevin sources for the normally ordered pair averages be reformulated. Therefore, instead of Eqns (9.7)–(9.9), we get

$$\frac{\partial a}{\partial t} = (\mathrm{i}+d)\frac{v_{\rm g}}{2k_0}\Delta_\perp a - \frac{\kappa}{2}a + g_{\rm g}\sigma + g_{\rm a}\pi + F_{\rm a}\,, \tag{9.12}$$

$$\frac{\partial \sigma}{\partial t} = -(\Gamma - \mathrm{i}\delta\omega)\sigma + g_{\rm g}(\sigma_2-\sigma_1)a + F\,,$$
$$\frac{\partial \sigma_1}{\partial t} = -\Gamma_1\sigma_1 + g_{\rm g}(\sigma^* a + \sigma a^*) + F_1\,, \tag{9.13}$$
$$\frac{\partial \sigma_2}{\partial t} = R_{\rm g} - \Gamma_2\sigma_2 - g_{\rm g}(\sigma^* a + a^*\sigma) + F_2\,,$$
$$\frac{\partial \pi}{\partial t} = -(\gamma - \mathrm{i}\delta\omega)\pi + g_{\rm a}(\pi_2-\pi_1)a + G\,,$$
$$\frac{\partial \pi_1}{\partial t} = R_{\rm a} - \gamma_1\pi_1 + g_{\rm a}(\pi^* a + a^*\pi) + G_1\,, \tag{9.14}$$
$$\frac{\partial \pi_2}{\partial t} = -\gamma_2\pi_2 - g_{\rm a}(\pi^* a + \pi a^*) + G_2\,.$$

The correlation relations for the Langevin sources are presented below (see Eqn (9.20)).

The master equations (9.12)–(9.14) completely describe the laser system considered. They can be substantially simplified when the medium response is fast compared to the field envelope variation, i.e., under the conditions $\kappa \ll \Gamma$, $\Gamma_{1,2}$, γ, $\gamma_{1,2}$. Hence, it becomes possible to exclude adiabatically the variables of active and passive centers and to get a closed equation for the field envelope. Let us also assume for simplicity that the relaxation rates of the upper and lower working levels of the centers are considerably different ($\Gamma_2 \ll \Gamma_1$ and $\gamma_1 \ll \gamma_2$). Under these conditions, the centers, after a short transient period, can be considered to follow the field state variation instantaneously. Assuming that in Eqns (9.13) and (9.14) the time derivatives are zero and the working transition frequencies coincide with the carrier frequency ($\delta\omega = 0$), we get

$$\Gamma\sigma = g_{\rm g}(\sigma_2-\sigma_1)a + F\,,$$
$$\Gamma_1\sigma_1 = g_{\rm g}(\sigma^* a + \sigma a^*) + F_1\,, \tag{9.15}$$
$$\Gamma_2\sigma_2 = R_{\rm g} - g_{\rm g}(\sigma^* a + a^*\sigma) + F_2\,,$$
$$\gamma\pi = g_{\rm a}(\pi_2-\pi_1)a + G\,,$$
$$\gamma_1\pi_1 = R_{\rm a} + g_{\rm a}(\pi^* a + a^*\pi) + G_1\,, \tag{9.16}$$
$$\gamma_2\pi_2 = -g_{\rm a}(\pi^* a + \pi a^*) + G_2\,.$$

Expressing the atomic variables in terms the field amplitude a by means of the algebraic relations (9.15) and (9.16) and introducing the notations

$$I_{\rm g} = \frac{\Gamma_1\Gamma_2}{4g_{\rm g}^2}\,,\quad I_{\rm a} = \frac{\gamma_1\gamma_2}{4g_{\rm a}^2}\,,\quad g_0 = \frac{R_{\rm g}}{\kappa I_{\rm g}}\,,\quad a_0 = \frac{R_{\rm a}}{\kappa I_{\rm a}}\,, \tag{9.17}$$

we arrive at the closed master equation for the field in the c-number representation:

$$\frac{\partial a}{\partial t} = (\mathrm{i}+d)\frac{v_{\rm g}}{2k_0}\Delta_\perp a + \frac{\kappa}{2}f\big(|a|^2\big)a + \Phi_{\rm a} + \Phi_{\rm g}\,, \tag{9.18}$$

$$f\big(|a|^2\big) = -1 + \frac{g_0}{1+|a|^2/I_{\rm g}} - \frac{a_0}{1+|a|^2/I_{\rm a}}\,. \tag{9.19}$$

Here, $|a|^2 = I$ represents the intensity or photon number of the generated radiation, g_0 and a_0 are the linear gain and resonant absorption coefficients, and $I_{\rm g}$ and $I_{\rm a}$ are the gain and absorption saturation intensities in the absence of frequency detunings.

Finally, the correlation relations for the Langevin sources, $\Phi_{\rm a}$ and $\Phi_{\rm g}$, have the form

$$\langle \Phi_i^*(t,\mathbf{r}_\perp)\Phi_j(t',\mathbf{r}'_\perp)\rangle = \langle \Phi_i^*\Phi_j\rangle\delta_{i,j}\delta(t-t')\delta(\mathbf{r}_\perp-\mathbf{r}'_\perp)\,,$$
$$i,j = {\rm g},{\rm a}\,,$$
$$\langle \Phi_{\rm g}^2\rangle = -\frac{R_{\rm g}}{2I_{\rm g}}\frac{a^2/I_{\rm g}}{(1+I/I_{\rm g})^2}\left(1+\frac{s_{\rm g}}{2}\right),$$
$$\langle |\Phi_{\rm g}|^2\rangle = \frac{R_{\rm g}}{I_{\rm g}(1+I/I_{\rm g})} - \frac{R_{\rm g}}{2I_{\rm g}}\frac{I/I_{\rm g}}{(1+I/I_{\rm g})^2}\left(1+\frac{s_{\rm g}}{2}\right), \tag{9.20}$$
$$\langle \Phi_{\rm a}^2\rangle = \frac{R_{\rm a}}{I_{\rm a}}\frac{a^2/I_{\rm a}}{(1+I/I_{\rm a})^2}\left(1-\frac{s_{\rm a}}{2}\right),$$
$$\langle |\Phi_{\rm a}|^2\rangle = \frac{R_{\rm a}}{2I_{\rm a}}\frac{I/I_{\rm a}}{(1+I/I_{\rm a})^2}\left(1-\frac{s_{\rm a}}{2}\right).$$

Note that these correlators are proportional to the corresponding pump rates $R_{\rm g}$ and $R_{\rm a}$. In the presence of external coherent holding radiation, with the frequency shifted relative to the carrier frequency by $\delta\omega_{\rm in} = (\kappa/2)\theta$ and the amplitude proportional to $a_{\rm in}$, an additional term arises in Eqn (9.18) (now the frequency of the holding radiation is

chosen for a carrier frequency):

$$\frac{\partial a}{\partial t} = (\mathrm{i}+d)\,\frac{v_\mathrm{g}}{2k_0}\,\Delta_\perp a + \frac{\kappa}{2}(a_\mathrm{in} + \mathrm{i}\theta a) + \frac{\kappa}{2}\,f\bigl(|a|^2\bigr)a + (\Phi_\mathrm{a} + \Phi_\mathrm{g})\,. \tag{9.21}$$

If we introduce the dimensionless time $t' = (\kappa/2)t$, the dimensionless coordinates $(x', y') = (x, y)\sqrt{\kappa k_0/v_\mathrm{g}}$, and the dimensionless field amplitudes $E = a/\sqrt{I_\mathrm{a}}$, $E_\mathrm{in} = a_\mathrm{in}/\sqrt{I_\mathrm{a}}$, then Eqn (9.21) will take the form (dashes are omitted)

$$\frac{\partial E}{\partial t} = (\mathrm{i}+d)\Delta_\perp E + f\bigl(|E|^2\bigr)E + E_\mathrm{in} + \mathrm{i}\theta E + \chi_\mathrm{g} Q_E\,, \tag{9.22}$$

where

$$\chi_\mathrm{g} Q_E = \frac{1}{(\kappa/2)\sqrt{I_\mathrm{a}}}(\Phi_\mathrm{a} + \Phi_\mathrm{g})\,, \qquad \chi_\mathrm{g} = \sqrt{\frac{\kappa k_0}{I_\mathrm{a} v_\mathrm{g}}}\,. \tag{9.23}$$

When disregarding the stochastic source Q_E, Eqn (9.22) transforms into the classical one.

9.2 Linearized Heisenberg–Langevin equation

Following Ref. [109], we start with the equation for the amplitude of the electromagnetic field E in the c-number representation (9.22). Let us consider weak fluctuations of the field in the neighborhood of a classical soliton with amplitude e_s and corresponding intensity $I_\mathrm{s} = |e_\mathrm{s}|^2$:

$$E(t,x) = e_\mathrm{s}(x) + \delta e(t,x)\,. \tag{9.24}$$

Langevin equation (9.22) turns into a deterministic classical equation for soliton field $e_\mathrm{s}(x)$ when ignoring the stochastic source, $\chi_\mathrm{g} Q_E \to 0$, and replacing $E(t,x)$ with $e_\mathrm{s}(x)$:

$$(\mathrm{i}+d)\Delta_\perp e_\mathrm{s} + \mathrm{i}\theta_\mathrm{in} e_\mathrm{s} + f(I_\mathrm{s})e_\mathrm{s} + E_\mathrm{in} = 0\,. \tag{9.25}$$

In this case, for a 'free' laser without an external holding field, the quantity $\theta_\mathrm{in} = \nu$ plays the role of an eigenvalue, or nonlinear shift of the soliton frequency with respect to the frequency of the longitudinal mode. In the presence of holding radiation, a field on the periphery of a classical fundamental soliton approaches the constant value $e_\mathrm{h} = e_\mathrm{s}(x \to \pm\infty)$, which corresponds to the intensity $I_\mathrm{h} = |e_\mathrm{h}|^2 > 0$. To eliminate this background in the nonlinearity function, it is also convenient to use the function $\delta f_\mathrm{s}(I_\mathrm{s}) = f_\mathrm{s}(I_\mathrm{s}) - f_\mathrm{s}(I_\mathrm{h})$, where $f_\mathrm{s}(I_\mathrm{s}) = f(I_\mathrm{s}) - f(0)$. Recall that the function $f(I)$ (see Eqn (2.1)) becomes complex-valued in the presence of detunings between the frequencies of the working gain and absorption transitions and the frequency of the laser longitudinal mode. We will consider only steady state (in the classical limit) regimes, corresponding to the synchronization regime.

The linearization of Eqn (9.22) with respect to δe leads to the inhomogeneous linear stochastic equation, which in the matrix form reads

$$\mathrm{i}\left(\frac{\partial}{\partial t} + \gamma\right) U(t,x) + LU(t,x) = \mathrm{i}W(t,x)\,, \tag{9.26}$$

where

$$U(t,x) = \bigl\{\delta e(t,x), \delta e^*(t,x)\bigr\}^\mathrm{Tr}\,, \qquad W(t,x) = \chi_\mathrm{g}\bigl\{Q_E(t,x), Q_E^*(t,x)\bigr\}^\mathrm{Tr}\,, \tag{9.27}$$

$$\gamma = -\mathrm{Re}\,f(0) - \mathrm{Re}\,f_\mathrm{s}(I_\mathrm{h})\,, \qquad \theta = \theta_\mathrm{in} + \mathrm{Im}\,f(0) + \mathrm{Im}\,f_\mathrm{s}(I_\mathrm{h})\,, \tag{9.28}$$

$$L = \begin{bmatrix} (1-\mathrm{i}d)\dfrac{\partial^2}{\partial x^2} + \theta + \mathrm{Im}\,f_{\mathrm{s}1} - \mathrm{i}\,\mathrm{Re}\,f_{\mathrm{s}1}\,, & -\mathrm{i}f_{\mathrm{s}2} \\ -\mathrm{i}f_{\mathrm{s}2}^*\,, & -(1+\mathrm{i}d)\dfrac{\partial^2}{\partial x^2} - \theta - \mathrm{Im}\,f_{\mathrm{s}1} - \mathrm{i}\,\mathrm{Re}\,f_{\mathrm{s}1} \end{bmatrix}, \tag{9.29}$$

$$f_{\mathrm{s}1} = f_{\mathrm{s}1}(x) = \delta f_\mathrm{s}\bigl(I_\mathrm{s}(x)\bigr) + I_\mathrm{s} f_\mathrm{s}'\bigl(I_\mathrm{s}(x)\bigr)\,, \qquad f_{\mathrm{s}2} = f_{\mathrm{s}2}(x) = f_\mathrm{s}'\bigl(I_\mathrm{s}(x)\bigr)e_\mathrm{s}^2(x)\,, \qquad f_\mathrm{s}' = \frac{\mathrm{d}f_\mathrm{s}}{\mathrm{d}I}\,. \tag{9.30}$$

We seek the solution of Eqn (9.26) as an expansion in the basis of eigenfunctions of the homogeneous equation, corresponding to Eqn (9.26). The eigenfunction with the eigenvalue λ has the form

$$U(t,x) = U_\lambda(x)\exp(-\gamma t - \mathrm{i}\lambda t) + U_\lambda^\dagger(x)\exp(-\gamma t + \mathrm{i}\lambda^* t)\,,$$
$$U_\lambda^\dagger(x) = \sigma_1 U_\lambda^*(x)\,, \qquad \sigma_1 = \begin{pmatrix} 0 & 1 \\ 1 & 0 \end{pmatrix}, \tag{9.31}$$
$$U_\lambda(x) = \bigl\{\varphi_\lambda(x), \bar\varphi_\lambda(x)\bigr\}^\mathrm{Tr}\,.$$

Here, $\bar\varphi_\lambda^*(x) = \varphi_{-\lambda^*}(x)$. Then, for the operator L and the Hermitian conjugate operator $L^\dagger = \sigma_1 L^* \sigma_1 = L^{\mathrm{Tr}*}$,

$$(L+\lambda)U_\lambda = 0\,, \quad (L-\lambda^*)U_\lambda^\dagger = 0\,, \quad (L^\dagger + \lambda^*)U_\lambda^\dagger = 0\,. \tag{9.32}$$

Hence, it follows that, for each eigenvalue of L, there is a second eigenvector:

$$U_\lambda^\dagger(x) = \sigma_1 U_\lambda^*(x) = \bigl\{\bar\varphi_\lambda^*(x), \varphi_\lambda^*(x)\bigr\}^\mathrm{Tr} = \bigl\{\varphi_{-\lambda^*}(x), \bar\varphi_{-\lambda^*}(x)\bigr\}^\mathrm{Tr} = U_{-\lambda^*}(x)\,. \tag{9.33}$$

For $\mathrm{Re}\,\lambda = 0$, these two vectors coincide, $U_\lambda^\dagger = U_\lambda$. In contrast to the operator in the case of a medium with purely 'conservative' Kerr nonlinearity [105, 106], the operator $\sigma_3 L$ is non-Hermitian, so that its eigenvectors are not orthogonal. Here, the Pauli matrix is introduced:

$$\sigma_3 = \begin{pmatrix} 1 & 0 \\ 0 & -1 \end{pmatrix}.$$

An arbitrary (weak) perturbation is represented as an expansion in functions of discrete and continuous spectra. The perturbation dynamics is described in terms of the Green's function G:

$$U(t,x) = \int_{-\infty}^{\infty} \mathrm{d}x'\, G(t,x,x')U(0,x') + \int_0^t \mathrm{d}t' \int_{-\infty}^{\infty} \mathrm{d}x'\, G(t-t',x,x')W(t',x')\,. \tag{9.34}$$

In vector formulation, the Green's function is written as

$$G(t,x,x') = \sum_{\lambda} \exp\left(-\gamma t - \mathrm{i}\lambda t\right) \left|U_\lambda(x)\right\rangle \left\langle U_\lambda(x')\right|, \quad (9.35)$$

and the stochastic function W is expressed as

$$\begin{aligned} W(t,x) &= \chi_{\mathrm{g}} \sum_{\lambda} w_\lambda(t) \left|U_\lambda(x)\right\rangle, \\ w_\lambda(t) &= \int_{-\infty}^{\infty} \mathrm{d}x \left[\varphi_\lambda^*(x) Q_E(t,x) + \varphi_{-\lambda^*}(x) Q_E^*(t,x)\right]. \end{aligned} \quad (9.36)$$

The continuous spectrum does not contribute to the mean-square fluctuations of the coordinate and momentum, which are of interest here; therefore, we restrict ourselves to an analysis of the discrete spectrum (localized perturbations) only. To determine these quantities, we will also need only the even (with respect to the soliton center) eigenvectors of the discrete spectrum. Such states, first of all, include the neutral mode of the operator $L + \mathrm{i}\gamma$ that corresponds to the eigenvector of problem (9.32) with the eigenvalue $-\mathrm{i}\gamma$. This is the time-independent solution of the homogeneous equation corresponding to Eqn (9.26):

$$U_0(x) = \left\{\varphi_0(x), \varphi_0^*(x)\right\}^{\mathrm{Tr}}, \qquad \varphi_0(x) = -e_{\mathrm{s}}'(x). \quad (9.37)$$

The existence of such a solution is due to the translational invariance of the master equation (9.22) (in the absence of a Langevin source). Since the profile of a classical fundamental soliton is symmetric, solution (9.37) is odd.

Other eigenvalues and eigenfunctions of the discrete spectrum of L are determined numerically. In the calculations, the finite width of the laser along the x-axis was fixed as $w_x = 40$, which barely changes the characteristics of a classical soliton because of the exponential decrease in its field at the periphery. The calculation shows that the discrete spectrum of the operator L comprises, besides the eigenvalue of the neutral mode $-\mathrm{i}\gamma$, a pair of eigenvalues $-\mathrm{i}\lambda_{\pm 1} = \gamma_1 \mp \mathrm{i}\omega_1$. This distinguishes the laser scheme from the interferometer scheme with Kerr nonlinearity, where the second eigenvalue is also purely imaginary ($\mathrm{i}\gamma$). The splitting decreases as the amplitude of the holding radiation grows, which is explained in a natural way by the laser scheme becoming closer to the interferometer scheme. The eigenfunctions of the discrete spectrum are localized, and they exponentially decrease at the periphery of the soliton, whereas the phase in this region linearly increases upon moving off the center. The calculations performed for the parameters of the region of a stable one-dimensional fundamental soliton at $g_0 = 2.08$, $a_0 = 2$, $b = 10$, $d_0 = 0.06$, and $\theta_{\mathrm{in}} = 0.047$, yield the values $\gamma_1 = 0.69$, $\omega_1 = 0.51$ for a free laser ($E_{\mathrm{in}} = 0$) and $\gamma_1 = 0.73$, $\omega_1 = 0.15$ for a laser with the amplitude of holding radiation $E_{\mathrm{in}} = 0.02$.

The part of the solution of inhomogeneous equation (9.26) corresponding to the contributions of the functions of the discrete spectrum is written in the form

$$\begin{aligned} \left|U(t)\right\rangle &= u_0 |U_0\rangle + \exp\left[-(\gamma-\gamma_1)t\right] \sum_{\pm 1} u_{\pm 1} \exp\left(\mp \mathrm{i}\omega_1 t\right) |U_{\pm 1}\rangle \\ &+ \chi_{\mathrm{g}} \int_0^t \mathrm{d}t'\, w_0(t') |U_0\rangle + \chi_{\mathrm{g}} \exp\left[-(\gamma-\gamma_1)t\right] \sum_{\pm 1} \exp\left(\mp \mathrm{i}\omega_1 t\right) \\ &\times \int_0^t \mathrm{d}t' \exp\left[(\gamma-\gamma_1)t'\right] w_{\pm 1}(t') \exp\left(\pm \mathrm{i}\omega_1 t'\right) |U_{\pm 1}\rangle. \end{aligned} \quad (9.38)$$

This expression includes coefficients of the expansion of the initial perturbations and the stochastic force

$$u_{0,\pm 1} = \left\langle U_{0,\pm 1} \middle| U(0)\right\rangle, \quad w_{0,\pm 1}(t) = \chi_{\mathrm{g}}^{-1} \left\langle U_{0,\pm 1} \middle| W(t)\right\rangle, \quad (9.39)$$

which are statistical quantities. Now, the approach developed in [105, 106] allows finding the perturbation dynamics of the coordinate δx and momentum δp of the soliton center, which can be determined as follows:

$$\begin{aligned} \delta x(t) &= \mathrm{i}^{-1} \left\langle \frac{1}{2}\left(U_{+1}^\dagger + U_{-1}^\dagger\right)\sigma_3 \middle| U(t)\right\rangle, \\ \delta p(t) &= \mathrm{i}^{-1} \left\langle U_0^\dagger \sigma_3 \middle| U(t)\right\rangle. \end{aligned} \quad (9.40)$$

Finally, we get the statistically averaged squares of the fluctuations of these quantities:

$$\begin{aligned} &\left\langle\left\langle \delta\hat{x}^2(t)\right\rangle\right\rangle = 4\chi_{\mathrm{g}}^2 U_{\mathrm{im}}^2 \overline{w_0^2} t \\ &+ \chi_{\mathrm{g}}^2 U_{11}^2 \left\{1 + \frac{\overline{|w_1|^2}}{\gamma-\gamma_1}\left(1 - \exp\left[-2(\gamma-\gamma_1)t\right]\right)\right\} \\ &+ \chi_{\mathrm{g}}^2 U_{11}^2 \frac{|\overline{w_1^2}|}{|\kappa_1|}\left\{\cos\vartheta_{11} - \cos\left(\vartheta_{11} - 2\omega_1 t\right) \exp\left[-2(\gamma-\gamma_1)t\right]\right\} \\ &+ 8\chi_{\mathrm{g}}^2 U_{11} U_{\mathrm{im}} \frac{|\overline{w_0 w_1}|}{|\kappa_1|} \\ &\times \left\{\sin\vartheta_{01} - \sin\left(\vartheta_{01} - \omega_1 t\right) \exp\left[-(\gamma-\gamma_1)t\right]\right\}, \end{aligned} \quad (9.41)$$

$$\begin{aligned} &\left\langle\left\langle \delta\hat{p}^2(t)\right\rangle\right\rangle = \chi_{\mathrm{g}}^2 |U_{01}|^2 \left\{\exp\left[-2(\gamma-\gamma_1)t\right]\right. \\ &+ \frac{\overline{|w_1|^2}}{\gamma-\gamma_1}\left(1 - \exp\left[-2(\gamma-\gamma_1)t\right]\right) \\ &\left. + \frac{|\overline{w_1^2}|}{|\kappa_1|}\left(\cos\vartheta_\kappa - \cos\left(\vartheta_\kappa - 2\omega_1 t\right) \exp\left[-2(\gamma-\gamma_1)t\right]\right)\right\}. \end{aligned} \quad (9.42)$$

When deriving Eqns (9.41) and (9.42), the definitions for the scalar products of non-orthogonal eigenvectors

$$\begin{aligned} U_{11} &= \left\langle U_{-1}^\dagger \sigma_3 \middle| U_1\right\rangle = \int_{-\infty}^{\infty} \mathrm{d}x \left(|\varphi_1|^2 - |\varphi_{-1}|^2\right), \\ U_{01} &= \left\langle U_0^\dagger \sigma_3 \middle| U_1\right\rangle = \int_{-\infty}^{\infty} \mathrm{d}x \left(\varphi_0^* \varphi_1 - \varphi_0 \varphi_{-1}^*\right), \\ U_{\mathrm{im}} &= \mathrm{Im}\, U_{01} \end{aligned} \quad (9.43)$$

and the notations

$$\begin{aligned} &\vartheta_{11} = \arg\frac{\overline{w_1^2}}{\kappa_1}, \quad \vartheta_{01} = \arg\frac{\overline{w_0 w_1}}{\kappa_1}, \\ &\theta_{01} = \arg U_{01}, \quad \vartheta_\kappa = \vartheta_{11} + 2\theta_{01} \end{aligned}$$

were used.

According to Eqns (9.41) and (9.42), the fluctuation variance infinitely increases upon approaching the boundary of the soliton stability, when $\gamma_1 \to \gamma$. In the domain of the soliton stability $\gamma_1 < \gamma$, as in the case of an interferometer, the square of fluctuation of the soliton center coordinate predominantly linearly grows with time (the consideration is restricted to the times at which the perturbation remains weak). A new feature is that, alongside the linear growth, the exponentially decaying oscillations of the variance with a

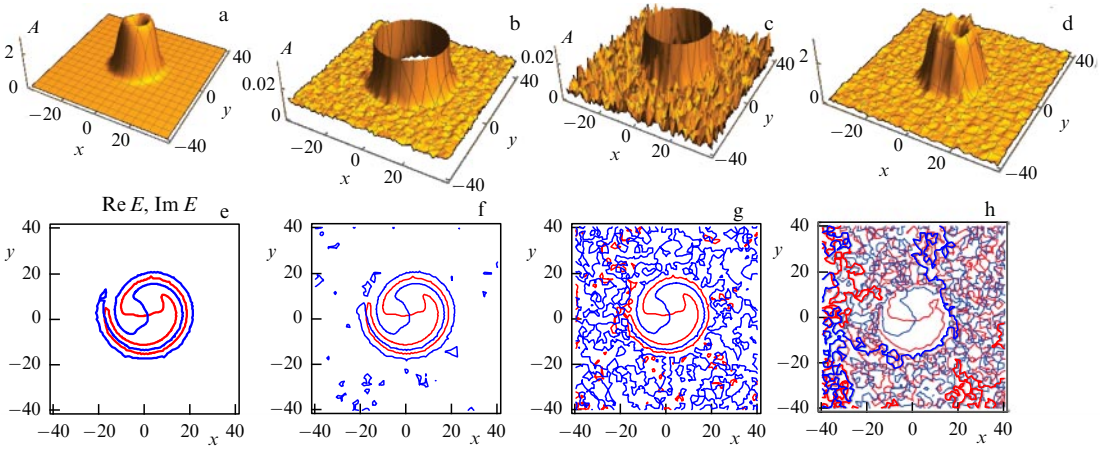

Figure 29. (Color online.) Profiles of real-valued amplitude $A = |E|$ (a–d) and contour lines of phase $\Phi = \arg E$ (e–h) (red curves correspond to $\operatorname{Im} E = 0$, blue ones, to $\operatorname{Re} E = 0$). $\chi_g = 0$ (a, f), 0.001 (b, f), 0.01 (c, g), 0.1 (d, h), $g_0 = 2.1$, $\theta = 0.08$. Profiles (b, c) are truncated in intensity to emphasize the periphery. On the maximum intensity scale, they practically coincide visually with the profiles in Fig. a.

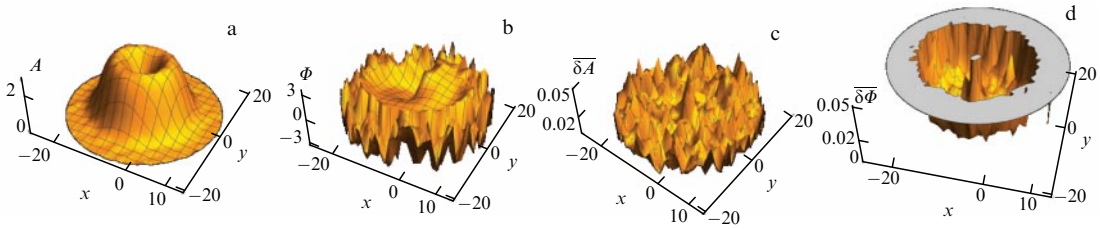

Figure 30. (Color online.) Profiles of stochastic amplitude $A(x, y)$ (a) and phase $\Phi(x, y)$ (b) and their mean-square deviations $\overline{\delta A}(x, y)$ (c) and $\overline{\delta\Phi}(x, y)$ (d). $\chi_g = 0.01$; the rest of the parameters are the same as in Fig. 29.

frequency of $2\omega_1$ appear. This is due to the above splitting of the eigenvalue of the discrete mode $-i\lambda_{\pm 1} = \gamma_1 \mp i\omega_1$ and manifests a dissipative character of the laser medium optical nonlinearity.

9.3 Numerical simulation

The direct numerical solution of the quantum mechanical Heisenberg–Langevin equation in the c-number representation is free from limitations on the weakness of the manifestation of fluctuations. The authors of [110] solved numerically the equations for the real-valued amplitude and phase, which follow from (9.22) upon the replacement $E(\mathbf{r}_\perp, t) \to A(\mathbf{r}_\perp, t) \exp(i\Phi(\mathbf{r}_\perp, t))$, $E_{in} \to A_{in} \exp(i\Phi_{in})$. It is convenient to characterize the intensity of the stochastic source by a dimensionless parameter χ_g; this intensity grows with an increase in cavity losses, which requires an appropriate increase in pumping. At fixed values of macroparameters g_0, a_0, and b, the value of χ_g varies within wide limits upon changing microparameters of the active and passive centers. Below, we present the results of simulating the quantum fluctuations of a two-dimensional soliton in a laser in the presence of coherent holding radiation with a small amplitude of $A_{in} = 0.01$. A symmetric soliton with the topological charge $m = 1$ served as the initial state (in the absence of fluctuations) (see Fig. 7).

The simulation results show that, on average, the soliton slightly changes in time upon increasing χ_g to $\chi_g = 0.1$. Figure 29 shows the amplitude profiles and isophase contour lines for three values of χ_g. It is seen that, upon increasing the stochastic force amplitude, the perturbations of the amplitude increase. In the peripheral phase distribution, initially homogeneous (equal to the phase of the holding radiation), at $\chi_g \geqslant 0.01$, pairs of dislocations appear (crossings of blue and red lines in the figure), which only 'shield' the influence of the peripheral dislocation (see [50]) upon changing χ_g to $\chi_g = 0.1$ (Fig. 29d).

Figure 30 presents the spatial profiles of the stochastic amplitude and phase in comparison with the time-averaged mean-square deviations, which for each point of the cross section are defined by the following expressions:

$$\overline{\delta Z^2}(x, y) = \left\langle (Z - \overline{Z})^2 \right\rangle_t = \left\langle Z^2 \right\rangle_t - \overline{Z}^2, \quad Z = A, \Phi. \quad (9.44)$$

From Fig. 30d, it is seen that, at the soliton periphery, where the field is small because of the smallness of the external field, and in the center, where the field tends to zero in the vicinity of the dislocation, the phase fluctuation becomes large (the plot is truncated at the level $\overline{\delta\Phi} = 0.05$).

The energy center vector of a soliton is defined by averaging the field coordinate over its intensity:

$$\tilde{x}(t) = \frac{\left\langle xA(x, y, t)^2 \right\rangle_{x,y}}{\left\langle A(x, y, t)^2 \right\rangle_{x,y}}, \qquad \tilde{y}(t) = \frac{\left\langle yA(x, y, t)^2 \right\rangle_{x,y}}{\left\langle A(x, y, t)^2 \right\rangle_{x,y}}. \quad (9.45)$$

Figure 31 presents the calculated dynamical changes (stochastic trajectories) of the center of inertia and the position of the basic dislocation of the soliton. In the classical case (Fig. 31a, b), the vector of their position difference, small in magnitude (about 1% of the soliton width), rotates in accordance with lunar-type motion and additionally oscil-

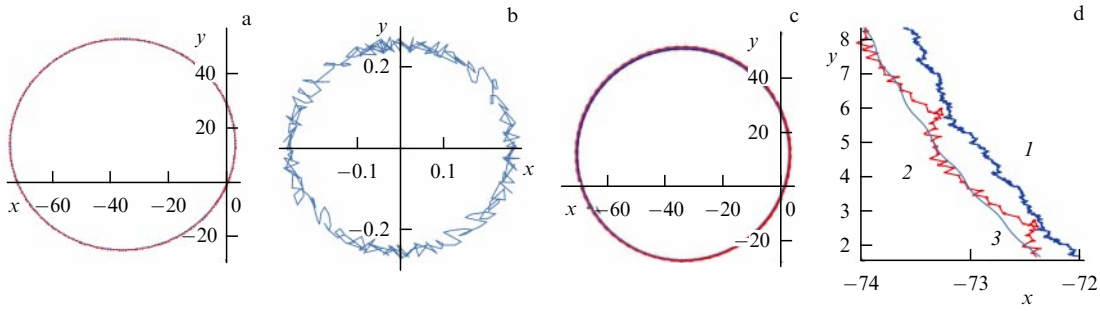

Figure 31. (Color online.) Trajectories of the soliton energy center (blue curves) and position of dislocation (red curves) at $\chi_g = 0$ (a) and $\chi_g = 0.1$ (c). (b) Small vector of the difference between the positions of the soliton center and the dislocation shown in Fig. a. (d) Fragments of trajectories, shown in Fig. c, for the energy center of the soliton (curve *1*), the center of dislocation (curve *2*), and their classical motion (curve *3*). Remaining parameters are the same as in Fig. 29.

lates with an amplitude of the order of 0.1%. This is due to the incomplete synchronization of the soliton and the external radiation, which leads to a small trembling of the dislocation position relative to the energy center. The introduction of quantum perturbations with the amplitude of the stochastic force, maximal among those considered (Fig. 29d), leads to a 'thickening of trajectories' (Fig. 31c) and increasing the amplitude of the position difference oscillation. Although the peripheral dislocation caused by the introduction of the holding beam becomes completely lost in the 'sea' of dislocations generated by quantum perturbations (Fig. 29d), the asymmetry of the intensity profile is preserved, as is, on average, lunar-type soliton motion. The amplitude of quantum perturbations of the dislocation position is somewhat greater than the perturbation amplitude of the center of inertia (Fig. 31d). The same can be said about the perturbations of the intensity maximum position, which, like the position of the energy center, is specified by a small value of the holding beam intensity, necessary for synchronizing the mean phase of the soliton to keep its stability. The fact that the fluctuations manifest themselves more strongly at the periphery of the soliton and in the neighborhood of topological singularities correlates with the natural increase in the importance of quantum effects with a decrease in radiation intensity.

10. Additional factors

Recall that the master equation (2.1) is only a basic one and requires specification and generalization to allow for various factors, some of them being listed in this section.

Anisotropy of '*diffusion*.' Above, we mainly started not even with the very equation (2.1), but with its simplified version (2.2) that follows from (2.1) with the equality of the 'effective diffusion coefficients,' $d_\perp$ and $d_\parallel$. When these coefficients differ ($d_\perp \neq d_\parallel$), the space $\mathbf{r}_3 = (x, y, \tau)$ becomes anisotropic. This leads to orientational effects in three-dimensional laser solitons, studied in [90].

Frequency detunings. We also mainly assumed the function $f(I)$ to be real-valued (see Eqn (3.2)), which, within the two-level model of active and passive centers, is valid if the working transition frequencies of these centers are close to the range of acting radiation frequencies (the frequency detunings are much smaller than the widths of spectral contours of the centers). The detunings are allowed for in one-dimensional and two-dimensional schemes in a number of papers (see [5] for references). The main effect of detunings is the development of self-focusing instabilities, including those leading to soliton fission into parts and even to their 'amoeba-like' dynamics [5].

It can also be noted that, in most papers devoted to the field, spectral broadening was considered homogeneous. Inhomogeneous broadening requires more complicated modeling, which, however, is significantly simplified for unidirectional propagation of radiation and the use of the ergodicity principles [113, 114].

Inhomogeneity of the scheme parameters. This important issue has been studied in a large number of papers (see [5] for reference). If the parameters are inhomogeneous, the invariance with respect to spatial translations vanishes. While random inhomogeneities can cause a capture (localization) of dissipative optical solitons, the introduction of regular inhomogeneities allows controlling their position and even proposing a kind of analog-to-digital information processing [5].

Inhomogeneities inevitably arise because of the restricted dimensions of real schemes. In Section 8, we already analyzed some consequences of the longitudinal limitations of the scheme. As for transverse limitations, their role in three-dimensional solitons can be revealed, for example, in a gradient optical fiber with a quadratic transverse profile of the refractive index. In this case, the master equation (2.2) includes an additional term:

$$\frac{\partial E}{\partial z} = (\mathrm{i} + d)\nabla_3^2 E + f_m E + \mathrm{i}\beta r_\perp^2 E\,. \tag{10.1}$$

Inhomogeneity that causes focusing at $\beta < 0$ *and defocusing at* $\beta > 0$. Consider the action of such an inhomogeneity on the bright apple soliton with the symmetry axis z or τ, presented in Section 7.2. For the defocusing inhomogeneity ($\beta > 0$), a soliton initially moving strictly along the z-axis begins to shift aside under the action of perturbations, deforms, increases in size, and disappears. If the inhomogeneity is focusing ($\beta < 0$), the result depends on its magnitude. With strong focusing ($|\beta| > 10^{-7}$), the apple compresses in transverse directions and elongates in the longitudinal one, moving along the z-axis. Its closed vortex line goes to the periphery of the soliton in the region of small intensities, after which the apple splits into two precessons, which are then destroyed (collapse) as they find themselves outside their stability domain.

At smaller values of $|\beta|$, the apple soliton preserves stability. Thus, the apple soliton is stable in a focusing potential with the coefficient $-10^{-7} < \beta < 0$. For the stability of more complex topological solitons, the limit value of $|\beta|$ must be an order of magnitude smaller. These conclusions allow evaluating the possibilities of formation and the

properties of topological laser solitons in real spatially limited schemes.

Relaxation effect. The inertialess response of a medium, expressed by relation (3.2), is violated in many types of laser media, whose response to radiation depends on the field state not only at the same moment of time but also in the preceding time interval. Considering new degrees of freedom related to the medium leads to the restriction of stability domains of laser solitons and the appearance of new types of them [5].

The ultimate manifestation of 'equality' of field and matter degrees of freedom is the dissipative (laser) solitons of self-induced transparency, which generalize the well-known McCall and Hahn solitons [115, 116] to the case of systems with gain and saturable absorption. In such media with two-level active and passive centers, the pulse transfers the active (gain) centers from the upper energy level to the lower one, providing a pickup of the stored energy (π-pulses). Simultaneously, in the passive centers, the leading edge of the pulse causes a transition from the lower energy level to the upper one, and the trailing edge returns the centers to the lower level, minimizing the absorption of radiation (2π-pulses). Initially, this mechanism was proposed as a regime of coherent mode locking with the generation of relatively long pulses in a laser [117]; such pulses can be considered dissipative solitons if their size is much smaller than the laser resonator length. The mechanism was confirmed experimentally in a titanium-sapphire laser with an absorber [118, 119]. For a nonresonator scheme, the dissipative solitons of self-induced transparency were found by numerical simulation in Refs [113, 120, 121] in the regime of extremely short pulses, including quasi-unipolar ones (the issue of quasi-unipolar pulses of radiation is considered in reviews [23, 122, 123]). They are one-dimensional temporal solitons; topological solitons of self-induced transparency have not been found yet, despite being of undoubted interest.

11. Conclusion

The properties of the topological structures considered in the review follow from the analysis of the unique and relatively simple master generalized Ginzburg–Landau equation (2.1), which adequately describes many basic mechanisms of oscillation in lasers with saturable absorption — the presence of laser gain saturated with the growth of radiation intensity and nonresonant and resonant nonlinear absorption. Although in real laser systems there is a considerable number of additional factors, the analysis shows that they do not hamper the formation of surprisingly diverse laser solitons. However, to our knowledge, to date, only two-dimensional topological laser solitons with axially symmetric intensity distribution and unit charge have been obtained experimentally [124, 125]; it can be hoped that this review will promote the carrying out of further experiments.

It seems important that topological laser solitons having a nontrivial internal structure demonstrate a wealth of physics of a wide class of open (dissipative) nonlinear systems, especially vividly expressed in three-dimensional solitons. In particular, we noted above the likeness of the topological charge nonconservation in the one-dimensional scheme considered in Section 4.2 and the phenomenon of phase slip in superconductivity, hydrodynamics, etc. A number of topological features of laser solitons have analogs in conservative systems [126], which may be related to the mutual compensation of the energy inflow and outflow under quasistationary conditions. However, the very presence of such flows, lacking in conservative systems, introduces additional peculiarities into the structure and dynamics of solitons. The interaction of topological and dissipative (energy) factors manifests itself also in the character of hysteresis when varying the system parameters. Namely, the loss of laser soliton stability with conservation of its topology can be associated with a smooth and reversible second-order phase transition, whereas the destabilization violating the soliton topology makes the hysteresis process jump-like and even irreversible.

Hopefully, the demonstration of both a wide collection of topological laser solitons and their interesting properties and interconversion will be helpful in searching for similar phenomena in other dissipative nonlinear systems, first and foremost, nonequilibrium Bose–Einstein condensates. Within purely optical and laser schemes, further development of the issue is naturally expected when an essential role is played by the degrees of freedom related to the inertia of the medium response (self-induced transparency effect) and quantum optical phenomena, substantial for minimizing the size and energy of solitons, which is important for applications.

In our opinion, the richness of physics and the applied potential of laser solitons justify the development of experimental studies in the field. Note also that, although the analysis of the quantum fluctuations in topological dissipative solitons is in the initial stage, the completion of the master equation linearization method by direct simulation based on the stochastic master equation allows significant softening of the limitations inherent in the analytical approach. This makes real the discovery of novel manifestations of the interaction of topological and quantum effects.

Acknowledgments

This review was written with the financial support of the Russian Foundation for Basic Research (RFBR) within project 19-12-50174 and is based on the studies carried out with the support of the Russian Scientific Foundation (RSF), grant 18-12-00075. The modeling of quantum fluctuations was supported by RFBR, grant 18-02-00402. A premature death prevented our colleague L A Nesterov from becoming a co-author of this review. The authors are grateful to A N Shatsev, Yu M Golubev, and T Yu Golubeva for their collaboration. Some of the results presented in the review were obtained using the computational resources of the Supercomputer Center at Peter the Great Saint Petersburg Polytechnic University (www.scc.spbstu.ru).

References

1. Kivshar Yu S, Agrawal G P *Optical Solitons*: *From Fibers to Photonic Crystals* (San Diego, CA: Academic Press, 2003); Translated into Russian: *Opticheskie Solitony*. *Ot Svetovodov k Fotonnym Kristallam* (Moscow: Fizmatlit, 2005)
2. Akhmediev N, Ankiewicz A *Solitons*: *Non-Linear Pulses and Beams* (London: Chapman and Hall, 1997); Translated into Russian: *Solitony*: *Nelineinye Impul'sy i Puchki* (Moscow: Fizmatlit, 2003)
3. Novikov S, Manakov S V, Pitaevskii L P, Zakharov V E *Theory of Solitons*: *The Inverse Scattering Method* (New York: Springer, 1984); Translated from Russian: Zakharov V E, Manakov S V, Novikov S P, Pitaevskii L P *Teoriya Solitonov*: *Metod Obratnoi Zadachi Rasseyaniya* (Moscow: Fizmatlit, 1980)
4. Rosanov N N *Dissipativnye Opticheskie Solitony*. *Ot Mikro- k Nano- i Atto-* (Dissipative Optical Solitons: From Micro- to Nano- and Atto-) (Moscow: Fizmatlit, 2011)

5. Rosanov N N *Dissipativnye Opticheskie i Rodstvennye Solitony* (Dissipative Optical and Related Solitons) (Moscow: Fizmatlit, 2021)
6. Jackiw R *Comments Nucl. Part. Phys.* **13** 141 (1984); Translated into Russian: *Usp. Fiz. Nauk* **149** 139 (1986)
7. Rosanov N N "I Transverse patterns in wide-aperture nonlinear optical systems", in *Progress in Optics* Vol. 35 (Ed. E Wolf) (Amsterdam: Elsevier, 1996) p. 1
8. Rosanov N N *Opticheskaya Bistabil'nost' i Gisterezis v Raspredelennykh Nelineinykh Sistemakh* (Optical Bistability and Hysteresis in Distributed Nonlinear Systems) (Moscow: Nauka. Fizmatlit, 1997)
9. Mandel P *Theoretical Problems in Cavity Nonlinear Optics* (Cambridge: Cambridge Univ. Press 1997)
10. Rozanov N N *Phys. Usp.* **43** 421 (2000); *Usp. Fiz. Nauk* **170** 462 (2000)
11. Weiss C O et al., in *Spatial Solitons* (Springer Series in Optical Sciences, Vol. 82, Eds S Trillo, W Torruellas) (Berlin: Springer, 2001) p. 393
12. Rosanov N N *Spatial Hysteresis and Optical Patterns* (Berlin: Springer, 2002)
13. Staliūnas K, Sánchez-Morcillo V J *Transverse Patterns in Nonlinear Optical Resonators* (Springer Tracts in Modern Physics, Vol. 183) (Berlin: Springer, 2003)
14. Akhmediev N, Ankiewicz A (Eds) *Dissipative Solitons* (Lecture Notes in Physics, Vol. 661) (Berlin: Springer, 2005); Translated into Russian: *Dissipativnye Solitony* (Moscow: Fizmatlit, 2008)
15. Akhmediev N, Ankiewicz A (Eds) *Dissipative Solitons*: *From Optics to Biology and Medicine* (Lecture Notes in Physics, Vol. 751) (Berlin: Springer, 2008)
16. Kuszelewicz R et al. (Eds) "Dissipative optical solitons" *Eur. Phys. J. D* **59** (1) (2010) Topical issue
17. Tlidi M et al. (Eds) "Localized structures in dissipative media: from optics to plant ecology" *Philos. Trans. R. Soc. Lond.* **372** (2027) (2014) Theme issue
18. Lugiato L, Prati F, Brambilla M *Nonlinear Optical Systems* (Cambridge: Cambridge Univ. Press, 2015)
19. Grelu P (Ed.) *Nonlinear Optical Cavity Dynamics*: *From Microresonators to Fiber Lasers* (Weinheim: Wiley-VCH Verlag, 2016)
20. Tlidi M, Clerc M G, Panajotov K (Eds) "Dissipative structures in matter out of equilibrium: from chemistry, photonics and biology, the legacy of Ilya Prigogine" *Philos. Trans. R. Soc. Lond. A* **376** (2135) (2018) Theme issue
21. Rosanov N N, Fedorov S V, Veretenov N A *Eur. Phys. J. D* **73** 141 (2019)
22. Rosanov N N et al. *Opt. Spectrosc.* **127** 77 (2019); *Opt. Spektrosk.* **127** 82 (2019)
23. Rosanov N N et al. *Quantum Electron.* **51** 959 (2021); *Kvantovaya Elektron.* **51** 959 (2021)
24. Mihalache D *Rom. Rep. Phys.* **73** 403 (2021)
25. Chembo Y K, Nan Y *Phys. Rev. A* **82** 033801 (2010)
26. Gorodetskii M L *Opticheskie Mikrorezonatory s Gigantskoi Dobrotnost'yu* (Optical Microresonators with a Giant Quality Factor) (Moscow: Fizmatlit, 2016)
27. Turitsyn S K et al. *Phys. Usp.* **59** 642 (2016); *Usp. Fiz. Nauk* **186** 713 (2016)
28. Shtyrina O V et al. *J. Opt. Soc. Am. B* **38** 2488 (2021)
29. Rozanov N N, Fedorov S V *Opt. Spectrosc.* **72** 782 (1992); *Opt. Spektrosk.* **72** 1394 (1992)
30. Fedorov S V, Khodova G V, Rosanov N N *Proc. SPIE* **1840** 208 (1992)
31. Rosanov N N, Khodova G V *J. Opt. Soc. Am. B* **7** 1057 (1990)
32. Karpov D V et al. *Phys. Rev. B* **92** 075305 (2015)
33. Lu L, Joannopoulos J D, Soljačić M *Nat. Photon.* **8** 821 (2014)
34. Ozawa T et al. *Rev. Mod. Phys.* **91** 015006 (2019)
35. Aranson I S *Phys. Usp.* **62** 892 (2019); *Usp. Fiz. Nauk* **189** 955 (2019)
36. Kvon Z D et al. *Phys. Usp.* **63** 629 (2020); *Usp. Fiz. Nauk* **190** 673 (2020)
37. Smirnova D et al. *Light Sci. Appl.* **9** 127 (2020)
38. Soskin M et al. *J. Opt.* **19** 010401 (2017)
39. Gbur G J *Singular Optics* (Boca Raton, FL: CRC Press. Taylor and Francis Group, 2017)
40. Yin X, Peng C *Photon. Res.* **8** (11) B25 (2020)
41. Scully M O, Zubairy M S *Quantum Optics* (Cambridge: Cambridge Univ. Press, 1997); Translated into Russian: *Kvantovaya Optika* (Moscow: Fizmatlit, 2003)
42. Grigor'yan V S, Maimistov A I, Sklyarov Yu M *Sov. Phys. JETP* **67** 530 (1988); *Zh. Eksp. Teor. Fiz.* **94** 174 (1988)
43. Okulov A Yu, Oraevsky A N *Tr. Fiz. Inst. Acad. Nauk SSSR* **187** 202 (1988)
44. Vanin E V et al. *Phys. Rev. A* **49** 2806 (1994)
45. Sazonov S V *Phys. Rev. A* **103** 053512 (2021)
46. Leontovich M A *Izv. Akad. Nauk SSSR Ser. Fiz.* (8) 16 (1944)
47. Leontovich M A, Fock V A *J. Phys. USSR* **10** 13 (1946); *Zh. Eksp. Teor. Fiz.* **16** 557 (1946)
48. Rosanov N N *Opt. Spectrosc.* **127** 285 (2019); *Opt. Spektrosk.* **127** 283 (2019)
49. Rosanov N N *Opt. Spectrosc.* **128** 1151 (2020); *Opt. Spektrosk.* **128** 1129 (2020)
50. Suchkov A F *Sov. Phys. JETP* **22** 1026 (1965); *Zh. Eksp. Teor. Fiz.* **49** 1495 (1965)
51. Rozanov N N *Sov. Tech. Phys. Lett.* **6** 335 (1980); *Pis'ma Zh. Tekh. Fiz.* **6** 778 (1980)
52. Rozanov N N *Sov. Phys. JETP* **53** 47 (1981); *Zh. Eksp. Teor. Fiz.* **80** 96 (1981)
53. Rosanov N N, Khodova G V *J. Opt. Soc. Am. B* **7** 1057 (1990)
54. Veretenov N A, Fedorov S V, Rosanov N N *Phys. Rev. Lett.* **125** 193901 (2020)
55. Shafie M M et al. *Chaos* **31** 093104 (2021)
56. Fedorov S V, Veretenov N A, Rosanov N N *Phys. Rev. Lett.* **122** 023903 (2019)
57. Belousova I M et al. *Sov. Phys. JETP* **25** 761 (1967); *Zh. Eksp. Teor. Fiz.* **52** 1146 (1967)
58. Arnold V I *Catastrophe Theory* (Berlin: Springer-Verlag, 1992); Translated from Russian: *Teoriya Katastrof* (Moscow: Nauka, 1990)
59. Imamoğlu A et al. *Phys. Rev. A* **53** 4250 (1996)
60. Langer J S, Ambegaokar V *Phys. Rev.* **164** 498 (1967)
61. Dee G *Physica D* **15** 295 (1985)
62. Chernych A I, Gabitov I R, Kuznetsov E A, in *Singular Limits of Dispersive Waves* (NATO ASI Series. Ser. B, Vol. 320, Eds N M Ercolani et al.) (New York: Plenum Press, 1994) p. 315
63. Gor'kov L, in *Charge Density Waves in Solids* (Modern Problems in Condensed Matter Sciences, Vol. 25, Eds L P Gor'kov, G Grüner) (Amsterdam: Elsevier Sci. Publ., 1989)
64. Andronov A A et al. *Theory of Bifurcations of Dynamical Systems on a Plane* (Jerusalem: Israel Program for Scientific Translations, 1971); Translated from Russian: *Teoriya Bifurkatsii Dinamicheskikh Sistem na Ploskosti* (Moscow: Nauka, 1967)
65. Pitaevskii L P *Phys. Usp.* **41** 569 (1998); *Usp. Fiz. Nauk* **168** 641 (1998)
66. Fedorov S V, Veretenov N A, Rosanov N N *Opt. Lett.* **45** 3284 (2020)
67. Simon D S *Topology in Optics*: *Tying Light in Knots* (Bristol: IOP Publ., 2021)
68. Berry M V, Dennis M R *Proc. R. Soc. Lond. A* **457** 141 (2001)
69. Soskin M S, Vasnetsov M V *Prog. Opt.* **42** 219 (2001)
70. Freund I *Opt. Commun.* **201** 251 (2002)
71. Ruchi, Senthilkumaran P, Pal S K *Int. J. Opt.* **2020** 2812803 (2020)
72. Rosanov N N et al. *Quantum Electron.* **51** 959 (2021); *Kvantovaya Elektron.* **51** 959 (2021)
73. Fedorov S V, Veretenov N A, Rosanov N N, submitted
74. San Miguel M, Feng Q, Moloney J V *Phys. Rev. A* **52** 1728 (1995)
75. Panajotov K, Tlidi M *Opt. Lett.* **43** 5663 (2018)
76. Rozanov N N *Quantum Electron.* **30** 1005 (2000); *Kvantovaya Elektron.* **30** 1005 (2000)
77. Veretenov N, Fedorov S, Rosanov N *Opt. Lett.* **46** 4076 (2021)
78. Barland S et al. *Nature* **419** 699 (2002)
79. Genevet P et al. *Phys. Rev. Lett.* **104** 223902 (2010)
80. Genevet P et al. *J. Nonlin. Opt. Phys. Mater.* **21** 1250029 (2012)
81. Hachair X et al. *IEEE J. Select. Topics Quantum Electron.* **12** 339 (2006)
82. Eslami M, Kheradmand R, Aghdami K M *Phys. Scripta* **2013** (T157) 014038 (2013)
83. Prati F et al. *Eur. Phys. J. D* **59** 139 (2010)
84. Anbardan S R et al. *Phys. Rev. E* **97** 032208 (2018)

85. Eslami M, Kheradmand R, Hashemvand H *Opt. Quantum Electron.* **46** 319 (2014)
86. Anbardan S R et al. *Phys. Rev. E* **101** 042210 (2020)
87. Vysotina N V et al. *Sov. Phys. J.* **28** 887 (1985); *Izv. Vyssh. Uchebn. Zaved. Fiz.* (11) 42 (1985)
88. Dennis M R et al. *Nat. Phys.* **6** 118 (2010)
89. Landau L D, Lifshitz E M *The Classical Theory of Fields* (Oxford: Pergamon Press, 1971); Translated from Russian: *Teoriya Polya* (Moscow: Nauka, 1988)
90. Veretenov N A, Rosanov N N, Fedorov S V *Phys. Rev. Lett.* **117** 183901 (2016)
91. Veretenov N A, Fedorov S V, Rosanov N N *Phys. Rev. Lett.* **119** 263901 (2017)
92. Veretenov N A, Fedorov S V, Rosanov N N *Philos. Trans. R. Soc. A* **376** 20170367 (2018)
93. Fedorov S V, Rosanov N N, Veretenov N A *JETP Lett.* **107** 327 (2018); *Pis'ma Zh. Eksp. Teor. Fiz.* **107** 342 (2018)
94. Rosanov N N, Fedorov S V, Veretenov N A *Theor. Math. Phys.* **203** 547 (2020); *Teor. Mat. Fiz.* **203** 134 (2020)
95. Adams C C *The Knot Book*: *An Elementary Introduction to the Mathematical Theory of Knots* (New York: W.H. Freeman, 1994)
96. Vakhitov N G, Kolokolov A A *Radiophys. Quantum Electron.* **16** 783 (1973); *Izv. Vyssh. Uchebn. Zaved. Radiofiz.* **16** 1020 (1973)
97. Veretenov N A, Fedorov S V, Rosanov N N, submitted
98. Carter S J et al. *Phys. Rev. Lett.* **58** 1841 (1987)
99. Rosenbluh M, Shelby R M *Phys. Rev. Lett.* **66** 153 (1991)
100. Spälter S et al. *Opt. Express* **2** 77 (1998)
101. Mecozzi A, Kumar P *Opt. Lett.* **22** 1232 (1997)
102. Nagasako E M, Boyd R W, Agarwal G S *Opt. Express* **3** 171 (1998)
103. Lantz E et al. *J. Opt. B* **6** S295 (2004)
104. Oppo G-L, Jeffers J "Quantum fluctuations in cavity solitons", in *Quantum Imaging* (Ed. M I Kolobov) (New York: Springer, 2007); Translated into Russian: in *Kvantovoe Izobrazhenie* (Ed. M I Kolobov) (Moscow: Fizmatlit, 2009)
105. Nesterov L A et al. *Opt. Spectrosc.* **106** 570 (2009); *Opt. Spektrosk.* **106** 639 (2009)
106. Nesterov L A, Veretenov N A, Rosanov N N *Opt. Spectrosc.* **118** 781 (2015); *Opt. Spektrosk.* **118** 815 (2015)
107. Nesterov L A, Veretenov N A, Rosanov N N *Opt. Spectrosc.* **118** 794 (2015); *Opt. Spektrosk.* **118** 828 (2015)
108. Golubeva T Yu et al. *Opt. Spectrosc.* **128** 505 (2020); *Opt. Spektrosk.* **128** 517 (2020)
109. Fedorov S V et al. *Laser Phys. Lett.* **18** 015204 (2021)
110. Fedorov S V, Rosanov N N, Veretenov N A *J. Phys. Conf. Ser.* **2103** 012150 (2021)
111. Davidovich L *Rev. Mod. Phys.* **68** 127 (1996)
112. Berestetskii V B, Lifshitz E M, Pitaevskii L P *Quantum Electrodynamics* (Burlington: Butterworth-Heinemann, 1982); Translated from Russian: *Kvantovaya Elektrodinamika* (Moscow: Nauka, 1989)
113. Vysotina N V, Rosanov N N, Semenov V E *Opt. Spectrosc.* **106** 713 (2009); *Opt. Spektrosk.* **106** 793 (2009)
114. Kozlov V V, Rosanov N N *Phys. Rev. A* **87** 043836 (2013)
115. McCall S L, Hahn E L *Phys. Rev.* **183** 457 (1969)
116. Poluektov I A, Popov Yu M, Roitberg V S *Sov. Phys. Usp.* **18** 673 (1975); *Usp. Fiz. Nauk* **114** 97 (1974)
117. Kozlov V V *Phys. Rev. A* **56** 1607 (1997)
118. Arkhipov M V et al. *JETP Lett.* **109** 634 (2019); *Pis'ma Zh. Eksp. Teor. Fiz* **109** 657 (2019)
119. Arkhipov M V et al. *Phys. Rev. A* **101** 013803 (2020)
120. Vysotina N V, Rozanov N N, Semenov V E *JETP Lett.* **83** 279 (2006); *Pis'ma Zh. Eksp. Teor. Fiz.* **83** 337 (2006)
121. Rosanov N N, Semenov V E, Vysotina N V *Quantum Electron.* **38** 137 (2008); *Kvantovaya Elektron.* **38** 137 (2008)
122. Rosanov N N, Arkhipov R M, Arkhipov M V *Phys. Usp.* **61** 1227 (2018); *Usp. Fiz. Nauk* **188** 1347 (2018)
123. Arkhipov R M, Arkhipov M V, Rosanov N N *Quantum Electron.* **50** 801 (2020); *Kvantovaya Elektron.* **50** 801 (2020)
124. Genevet P et al. *Phys. Rev. Lett.* **104** 223902 (2010)
125. Yaparov V V et al. *Opt. Spectrosc.* **112** 601 (2012); *Opt. Spektrosk.* **112** 655 (2012)
126. Villois A, Proment D, Krstulovic G *Phys. Rev. Fluids* **2** 044701 (2017)